CALIBRATED EXPOSURE, FOCUS AND DEFECT TEST PATTERNS FOR OPTICAL LITHOGRAPHY

by

Bachvan Huynh

Memorandum No. UCB/ERL M88/36

27 May 1988

CALIBRATED EXPOSURE, FOCUS AND DEFECT TEST PATTERNS FOR OPTICAL LITHOGRAPHY

by

Bachvan Huynh

Memorandum No. UCB/ERL M88/36

27 May 1988

ELECTRONICS RESEARCH LABORATORY

College of Engineering
University of California, Berkeley
94720

CALIBRATED EXPOSURE, FOCUS AND DEFECT TEST PATTERNS FOR OPTICAL LITHOGRAPHY

by

Bachvan Huynh

ELECTRONICS RESEARCH LABORATORY

College of Engineering
University of California, Berkeley
94720

Author   **Bachvan Huynh**

Title   **Calibrated Exposure, Focus and Defect Test Patterns**

                for Optical Lithography

RESEARCH PROJECT

Submitted to the Department of Electrical Engineering and
Computer Sciences, University of California, Berkeley,
in partial satisfaction of the requirements for the degree
of Master of Science, Plan II.

Approval for the Report and Comprehensive Examination:

Committee: _____ , Research Adviser

            _____   Date
               May 19, 1988

            _____

                                         Date
               May 19, 1988

Calibration of Exposure, Focus and Defect Test Patterns for Optical Lithography

Bachvan Huynh

Department of Electrical Engineering and Computer Sciences

University of California, Berkeley

ABSTRACT

A set of optical test patterns have been designed, laid out, projection printed, and evaluated. The patterns include structures for the inspection of critical defect locations between features, near elbows and corners, and structures for monitoring exposure and focus. Simulations of two-dimensional aerial image (with 2D and SPLAT) and of resist profile dissolution (with SAMPLE) were used both in pattern selection and sizing and in the interpretation of results. These patterns were printed on a GCA 6200 stepper at a numerical aperture (NA) of 0.28 μm, wavelength (λ) of 0.4358 μm, and partial coherence factor (σ) of 0.7. A focus-exposure matrix was used to reveal focus and dose effects. Standard resist, thin resist, and substrates of different reflectivity were used to explore the role of the resist and substrate. SEM photographs of the printed defect patterns agree with modeling predictions that opaque defects centered between features bridge at a size of 0.35 λ/NA, while the transparent defects bridge later, and that the most critical location is an opaque defect near the corner of a resist line. Sub-imageable patterns for monitoring exposure dose show good sensitivity and excellent agreement with the simple algebraic model but must be corrected for bias effect in mask making. Arrays of small squares and lines for monitoring focus also show adequate sensitivity to determine best focus position.

May 20, 1988

Table of Contents

Chapter 1

Introduction

As the minimum feature size of integrated circuits becomes smaller, the techniques used to characterize the performance of optical projection systems must become more sophisticated. For example, test patterns that can greatly speed up the characterization of stepper performance using a low power optical microscope are sought for monitoring the proper tuning of optical process parameters such as dose and focus. Other classes of targets are needed for diagnosing optical system parameters and characterizing the printability of defects through SEM studies.

A number of test patterns have been designed to meet these needs. The Kodak test pattern has traditionally been used to examine printing quality. Electrical measurement techniques are also frequently used. [1] Recently, more parameter isolating targets have been developed by Siemens for monitoring exposure dose.[2] These have been extended to monitor focus position.[3]

Systematic studies of these approach have been undertaken at U.C. Berkeley. A set of parameter isolating test structures have been design, calibrated, and tested for stepper characterization. These structures have been designed for rapid reading with a low power optical microscope. The structures provide quantitative measures for monitoring the balance of the complex interrelationships between parameters of the exposure tool, lithographic material, and wafer condition. The quantitative evaluation of the visual portion of these revised lithography test targets with image [4,5] and resist profile simulations [6] is the subject of this study.

In a Fall 87 class, traditional imagery characterization test patterns and the above mentioned parameter isolating patterns were designed and implemented, together with some new exploratory test structures for both visual and electrical characterization of stepper performance.[7] The visual targets of interest here were laid out by William Haller and Davor Sutija, converted into a mask tape by Kenny Toh and the mask was made in the microlab by Marylin Kushner. These patterns were then printed on wafers in a focus dose matrix using various resist thickness and substrate combinations. Visual inspection on an optical microscope was made for the targets desired for rapid reading at low power. A set of chrome

on glass and resist on glass wafers were also produced for optical inspection. SEM's for the detailed studies were made with the help of Tom Booth on the CWIKSCAN II.

Chapter 2

Processes

1. Layout

The layout of the test patterns were done on a Microvax using the latest generation of CAD tool OCT/VEM at U.C. Berkeley. The layout in an OCT file was converted to a CIF file which was then converted to a MANN file for mask making.

2. Mask Making

The patterns in the MANN file were converted onto the mask using the GCA 3600F pattern generator in the U.C. Berkeley Microelectronics Facility. Due to a much smaller bias comparing to an emulsion mask, a chrome mask of the test patterns was chosen to be fabricated. The bias on the 10X chrome mask was measured with a Vickers Image Shearing Microscope and was found to be

$$\Delta x = +0.3 \text{ and } \Delta y = +0.6 \text{ for openings in chrome}$$
$$\Delta x = -0.6 \text{ and } \Delta y = -1.2 \text{ for chrome width}$$

3. Wafer Preparation

Three different wafers were prepared for the experiment in order to explore the role of the resist and substrate :

a.   Si : Silicon wafer coated with 1.2 μm of Kodak 820 Micropositive photoresist, 120 °C prebake.

b.   Si : Silicon wafer coated with 1810 A of thin resist (Shipley 1400-21 diluted 50:50), 90 °C prebake and 110 °C postbake.

c.   Al : Aluminum deposited on Si and coated with 1.2 μm of Kodak 820 Micropositive photoresist, 120 °C prebake.

4. Exposure

The wafers were printed on a GCA 6200 10X stepper at a numerical aperture (NA) of 0.28 μm, wavelength (λ) of 0.4358 μm, and partial coherence factor (σ) of 0.7. The wafers were exposed in a standard focus-exposure matrix, with exposures ranging from 0.07 sec to 0.19 sec in 0.02 sec steps, and

with focus settings ranging from 258 to 282 in steps of 4. Although this could not be confirmed, 4 GCA focus units are estimated to be equivalent to a vertical movement of 1 μm, which in turn corresponds to approximately 0.36 Rayleigh units of defocus.

5. Development

The wafers were developed on a MTI Omnichuck Photoresist Development Station. Kodak 934 (50% concentration [i,e, 1:1 concentrate:H_2O of 1:1 premixed]) was used to develop the photoresist. Spin-Spray and a 60 sec development time were used. No post exposure bake was done except for thin resist at 110 °C.

6. SEM

Prior to taking SEM photographs, the wafer was coated with about 300A of gold in a Hummer sputtering system to realize better resist contrast. Most of the photographs of the test patterns were taken from the top-view and at a voltage of 21KV on a Nanometric CWIKSCAN II SEM.

Chapter 3

Exposure Monitor

The use of non-printable features to reduce mask transmission as introduced by Wolfgang Arden and Dietrich Widmann [2] appears to be a very promising way to monitor exposure independent of focus and other confounding factors. These structures consist of subimageable features which scatter light into angles outside the acceptance angle of the lens. This is used to reduce the effective transmission area by area. By observing with a low power microscope which area first fails to clear, changes in the effectiveness of the exposure can be monitored. These structures were designed, analyzed with image simulation, laid out and tested.

1. Structures Description

The exposure monitor consists of a set of 17 10μm x 10μm areas filled with arrays of sub-imageable patterns to reduce the transmitted intensity. The pattern sizes are increased area by area to allow a gradual decrease in transmission. Any variation in the exposure or process will result in a change in the particular target area which just clears. A layout of the structures is shown in Figure 3.1. Each pattern is labelled with the fraction of the area that is clear. The sizes used and the corresponding transmitted intensity values are given in Table 3.1.

2. Algebraic Model

A simple algebraic model can be used to determine the pattern transmitted intensity from the pattern dimensions. According to scalar diffraction theory, for the 1D case shown below, the E field transmitted through the pattern is proportional to the fraction of the clear area. The transmitted intensity which is given by the square of the electric field is thus proportional to the square of the open area.
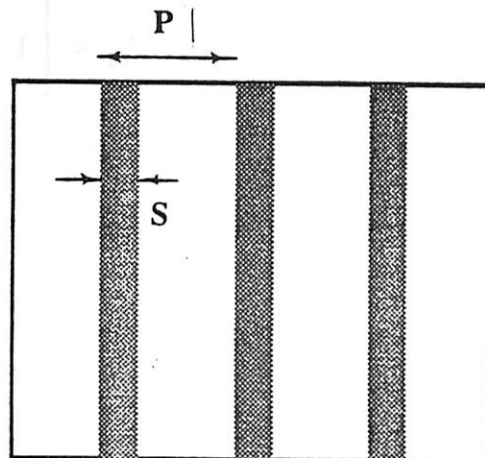
$$E_{dc} = \frac{S}{P}$$

$$I_{dc} = \left[E_{dc}\right]^2 = \left[\frac{S}{P}\right]^2$$

Similarly for the 2D cases shown below
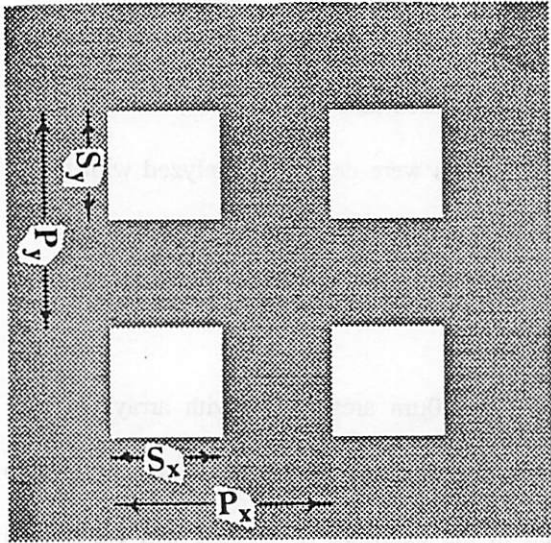
Normal Polarity
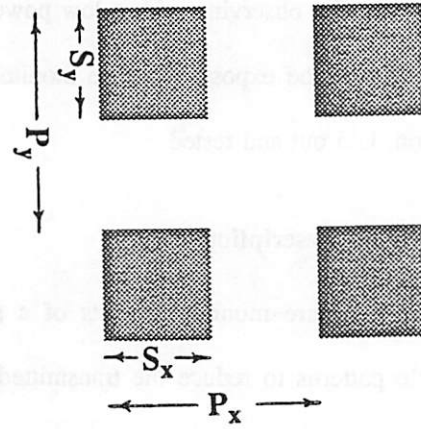
Reverse Polarity

$$E_{dc} = \frac{S_x}{P_x} \frac{S_y}{P_y}$$

$$E_{cc} = 1 - \frac{S_x}{P_x} \frac{S_y}{P_y}$$

$$I_{dc} = \left[\frac{S_x}{P_x} \frac{S_y}{P_y} \right]^2$$

$$I_{cc} = \left[1 - \frac{S_x}{P_x} \frac{S_y}{P_y} \right]^2$$

In our design for the exposure monitor, normal polarity patterns (dark field) are used for transmissions of up to but not including 25%. For transmissions above 25%, reverse polarity patterns (bright field) are used. An equal area checkerboard pattern is used for the 25% transmission (actual 0.3 μm x 0.3 μm but is shown in Table 3.1 as 0.6 μm x 0.3 μm so the same formula can be used).

The maximum pitch of these periodic patterns can be determined by making the first diffracted order lie just outside the lens. That is $\frac{2\pi}{P} = 2\pi\sigma\frac{NA}{\lambda}+2\pi\frac{NA}{\lambda}$ or $P = \frac{1}{(1+\sigma)}\frac{\lambda}{NA}$. Since σ is in the range of 0.3 to 0.7, the maximum period is about 0.6 λ/NA. This is 0.9 μm as viewed at the wafer on the GCA 6200 or 9 μm on the mask.

Aerial image simulation with 2D[4] is used to verify the algebraic model. The results are shown in Table 3.2 for the various sizes used. Excellent agreements to 0.1% are found between these two models. It should be noted that the formulas used in the algebraic model are independent of the optical system parameters, thus a simple optical bench set up could be used to calibrate the mask transmission.

3. Experimental Results

In Figure 3.1, the labels on the exposure monitor patterns range from 0.1 to 0.9 which correspond to transmission from 1% to 81% of the incident intensity. Figure 3.2 shows a photograph of these targets on a wafer at low magnification. It is interesting to note that the area labelled 0.5 clears before that labelled 0.55. This effect is caused by the bias in mask making. Figure 3.3 is a photograph of the mask in reflected light which shows the severe bias effect on the ideally equal area checkerboard pattern used in the 0.5 case. As a result, the 0.5 pattern allows more light to go through than the 0.55 pattern which is based on larger features. The transmission of the test targets as corrected for 0.03 μm bias in x and 0.06 μm bias in y for bright field, and 0.06 μm bias in x and 0.12 μm bias in y for dark field is given in Table 3.3.

Figures 3.4 and 3.5 show photographs of the exposure patterns printed at different exposure time on Si and Al substrate (with Kodak 820 resist). Good sensitivity is observed on both substrates. The targets are easier to read on Si than on Al. Figure 3.6 plots the number of targets that are clear as a function

of exposure time for the regular resist thickness. Figures 3.7 and 3.8 replot this data in terms of the intensities transmitted to clear. The exposure time to clear is inversely proportional to target transmission. At the best exposure time as determined by the operator, the resist is found to clear the targets at a transmission of 70%, 73%, and 56% for silicon, aluminum and thin resist on silicon.

4. Evaluation

4.1. Observations

1   The simple algebraic model has been verified with two-dimensional aerial image simulations. Thus the pattern size and pitch of an exposure target having desired transmission values can easily be obtained. The actual transmission depends on bias which can vary from mask to mask. As a result, it is necessary to calibrate each area. This need not be done on the steppers as the formulas can be used on a bench top microscope system which accepts only the DC component of the transmitted light.

2   The exposure patterns show good sensitivity to exposure time when they are printed on both the Si and Al substrates coated with Kodak 820 resist. The patterns printed on thin resist are found to be cleared mostly at a transmission of 56% at all doses. It appears that the thin resist process happens to fall in the region where not many targets were designed (i,e, between 30.2% and 56.4%)

4.2. Recommendations

1.   Since the transmitted intensity is proportional to the square of the fraction of open area, the exposure targets should be labelled in terms of transmission rather than area.

2.   Transmissions in the range of 50% to 80% in steps of 2% are recommended in future targets design.

3.   Pattern sizes as large as possible should be used in order to reduce the effect of bias. The maximum pitch of up to $\dfrac{1}{(1+\sigma)}\dfrac{\lambda}{NA}$ or 0.9 μm (0.58 λ/NA) could be used.

4. Rerun with smaller dose steps on the order of 2% of nominal is recommended.

Chapter 4

Focus Monitor

An extension of the exposure monitor patterns for focus has been suggested by A.R. Neureuther.[3] The concept is that only in focus will the minimum intensity of the opaque region dip below resist threshold (see Figure 4.1). Both 1D and 2D patterns of this type have been designed, laid out, tested and evaluated with simulation. The test patterns are designed for rapid visual inspection with a low power optical microscope to determine the best focus position.

1. Structures Description

The focus targets consist of a sequence of 10 x 10 μm areas with small 1D and 2D features with a 4 μm period. The feature size is increased area by area. Figure 4.2 shows the layout of the structures.

1.1. 1D Focus Targets

The 1D focus monitor consists of 6 sets of opaque lines in a clear field ranging from 0.5 μm to 1.0 μm in steps of 0.1 μm which correspond to 0.3 λ / NA to 0.7 λ / NA. They are marginally resolvable and hence are sensitive to defocus.

1.2. 2D Focus Targets

The 2D focus monitor consists of 6 sets of opaque squares in a clear field ranging from 0.8 μm to 1.3 μm in steps of 0.1 μm which correspond to 0.5 λ / NA to 0.8 λ / NA. They are marginally resolvable and hence are sensitive to defocus.

2. Intensity Design Curves

The sizes of the 1D/2D opaque features in the 10 μm x 10 μm areas are selected through two-dimensional aerial image simulation with 2D[4] by area. The minimum intensity in the image rapidly increases with defocus. As a result, the number of target areas which leave resist features to scatter light decreases with the amount of defocus. The 1D and 2D intensity design curves are shown in Figures 4.3 and 4.4 which plot the minimum intensity in the image versus defocus in Raleigh unit. The

curves in Figure 4.4 have a steeper slope than those in Figure 4.3 indicating that the 2D targets are more sensitive to defocus than the 1Ds'. Photographs of the printed focus test patterns shown in Figures 4.5 and 4.6 also verify this observation.

3. Experimental Results

Figures 4.5 and 4.6 show the photographs of the focus targets printed at different focus positions on Si and Al substrates (with Kodak 820 resist) respectively. The best focus position is determined by the position which has the smallest features resolved. Plotted in Figure 4.7 and 4.8 are the target counts on Si versus focus positions for the 1D and 2D targets respectively. Each target is given a count of either 1 or 2 depending on how clear it is printed. A count of 2 is given to an area which is clearly printed and a count of 1 to an area barely printed. As can be seen from the photographs, the 2D targets give a sharper response to focus than the 1D targets.

4. Evaluation

4.1. Observations

1. The 1D and 2D focus targets appear to be usable in determining the best focus position with 2D targets being significantly more sensitive.

2. The 1D and 2D target counts do not follow a threshold intensity model. The discrepancies appear to be due to non-vertical resist dissolution phenomena.

3. Both the 1D and 2D targets printed on thin resist have the smallest features resolved at all focus position.

4.2. Recommendation

1. The optimum range of focus targets should be adjusted to be from 0.3 to 0.8 μm (0.2 to 0.5 λ/NA) for the 1D case, and 0.7 to 1.2 μm (0.45 to 0.75 λ/NA) for the 2D case.

2. Smaller gradation in sizes on the order of 0.05 μm or 0.03 λ/NA should be used.

3. 1D targets in both the horizontal and vertical directions should be placed adjacent to each other to

test for astigmatism.

Chapter 5

Defect Structures

Five basic feature types with programmed defects of various sizes and separations from and protrusions into features have been designed to characterize the printability of defects in optical projection printing. The features are used to screen for structures that are sensitive to defects and to investigate parameter effects such as focus, exposure, and substrate reflectivity on defect printability. Two-dimensional aerial image simulation with 2D [4] and SPLAT [5] and resist profile dissolution simulation with SAMPLE [6] were used to select the pattern shapes and sizes.

1. Structures Description

Each of the five categories of features with programmed defects is descripted in this section. All the lines are 1.3 μm wide, corresponding to 0.8 λ /NA. All designs are realized in both polarities.

Category[1]: Isolated lines with square defects of the same polarity sized 0.3, 0.5, and 0.6 μm separated from the lines by distances of 0.2, 0.3 and 0.5 μm (Figure 5.1(a)).

Category[2]: Equal lines and spaces with defects sized 0.3, 0.5, 0.6, and 0.8 μm located on the edge of a line and also in the center between lines (Figure 5.1(b)).

Category[3]: 10 μm x 10 μm square area with 0.5 μm x 0.5 μm defects (a) of the same polarity located on the exterior diagonals at distances of 0.2, 0.3, 0.4 and 0.5 μm from the corners (b) of the same polarity collinear with each of the four edges at distances of 0.2, 0.3, 0.4 and 0.5 μm from the edges of the square (c) of opposite polarity located on the interior diagonals at distances of 0.2, 0.3, 0.4 and 0.5 μm from the corners (Figure 5.1(c)).

Category[4]: Isolated elbows with 0.5 x 0.5 μm defect of opposite polarity (a) located on the upper corner of the elbow (b) collinear with both the outer horizontal edge and the inner vertical edges of the elbow (c) collinear with the outer horizontal edge and at 2.6 μm from the outer vertical edge of the elbow (d) collinear iwth both the inner horizontal and vertical edges of the elbow (Figure 5.1(d)).

Category[5]:   Nested elbows with two 0.5 x 0.5 μm defects of the same polarity (a) one located on

the exterior diagonal of the outermost elbow at distances of 0.2, 0.3, 0.4 and 0.5 μm

from the elbow corner, the other located along the diagonal between the inner two

elbows at distances of 0.2, 0.3, 0.4 and 0.5 μm from the innermost elbow corner (b)

one collinear with the inner vertical edge of the outermost elbow at distances of 0.2,

0.3, 0.4 and 0.5 μm from the outermost elbow, the other located between elbows and

with its upper edge collinear with the upper edge of the innermost elbow at distances

of 0.2, 0.3, 0.4 and 0.5 μm from the innermost elbow (Figure 5.1(e)).

2. Experimental Results

Shown in Figure 5.2 are two photographs of the mask taken in reflected light showing different

bias effect on opaque and transparent defects. For two defects of the same size, bias in mask making

will result in a smaller opaque defect than a transparent defect. Figure 5.3 shows the SEM cross sec-

tion of a periodic pattern of line=space=1.3μm when it is at best focus dose, best focus underexposed,

and best dose 3μm defocus. The actual line and space widths from measurement in each case are also

included to show the effect of process bias. As can be seen from the photographs, the resist wall angle

gets steeper in going from underexposure to best exposure.

Category[1]:   Figures 5.4 and 5.5 show the SEM pictures of the two polarities of the isolated lines

with defects of different sizes at different spacings from the lines. Spacing increases

from 0.2 to 0.3 and 0.5 μm and ΔL decreases moving from left to right. Defect size

increases from 0.3 to 0.5 and 0.6 μm and ΔL increases moving vertically. At best

focus and exposure, ΔL is similar although bottom of resist has larger ΔL for opaque

defect. In the opaque case, underexposure increases the printability of defects. A 3 μm

defocus slightly reduces the effect of defects. In the transparent case, no observable

difference is found in the three situations in Figure 5.4. Defocus does not have a

beneficial effect as might be anticipated. The ΔL may not be quite as large but is

noticeably larger in a direction parallel to the line. This is due to larger spot size with

defocus and poorer line edge intensity slope. Figures 5.6 and 5.7 show the enlarged

portion of the 0.3μm transparent and opaque defects at a spacing of 0.2μm from the line. Figures 5.8 and 5.9 show the 0.6μm transparent and opaque defects at a spacing of 0.2μm from the line. The ΔLs were measured for the opaque defects and are shown in Table 3.4. In Figure 5.10, the data for a touching transparent defect for the 30% intensity contour is reproduced from[8] [Ref. 8] with additional data points for the transparent and opaque defects at 0.2μm from the line. Note that the ΔLs caused by the opaque defects are larger than those predicted by the intensity threshold model and that the ΔLs caused by the transparent defects are smaller. Additional exposure or development time will remove this but at the expense of additional bias. Simulations with SPLAT were done for the 0.6μm opaque defect corrected for bias at different spacings (0.2, 0.3 and 0.5μm) from a line and are shown in Figures 5.11, 5.12 and 5.13. From the simulated intensity contour plots, the ΔL determined from the 30% intensity contour is found to be inversely proportional to spacing. On the other hand the 20% intensity contour is moving further away from the line edge. The measured results in Table 3.4(a) first increase and then decrease. This behavior is apparently caused by non-vertical resist dissolution effects. Figure 5.14 shows the effects of the 3μm defocus. The ΔL of the 30% contour is slightly reduced in Figure 5.14 which agrees with the experimental result. Figure 5.15(a) and (b) are the transparent counterparts of Figures 5.11 and 5.14 respectively. A defocus of 3μm has even less effect on the printability of the transparent defect.

Category[2]: Figures 5.16(a) and (b) show the SEM photographs of the two polarities of the line arrays with centered and edged defects. As can be seen from the pictures, centered defect bridging effect is worst for the opaque case than the transparent case even with bias effect. The opaque centered defect bridges at a size of 0.6 μm (or 0.54 μm after corrected for bias which corresponds to 0.35 λ / NA) whereas no bridging effect is observed for the transparent defect even at a size of 0.8 μm. For defect sizes less than 0.5 μm, edge defect is worse than centered defect. Figures 5.17 and 5.18 show the

enlarged portion of the 0.5 μm opaque centered defect for Si and Al respectively when it is at best focus dose, at best focus underexposed, and at best dose 3 μm defocus respectively. Underexposure causes the two lines to bridge and a 3 μm defocus doesn't have much effect to the printability of defect.

These defect patterns have also been simulated with SPLAT and are shown in Figures 5.19(a) and (b). The simulated contour plot was scaled to enable a direct overlay of the contour over the SEM picture for better comparison. The lines follow approximately the 30% threshold at best focus dose. The fact that the protrusion from the line deviates from the 30% threshold gives an evidence of non-vertical resist dissolution phenomena. Shown in Figures 5.20(a), (b), and (c) are the reverse polarity of Figures 5.17(a), (b), and (c). In the transparent case (Figure 5.20), the effect of the defect is significantly smaller than that of the opaque case.

Category[3]: Figures 5.21 and 5.22 show the transparent and opaque square areas respectively with defects located diagonally from the corners. Three cases are shown in each figure: best focus dose, best focus underexposed, and best dose 3 μm defocus. The corner defects do not print except for underexposed opaque corner defects as shown in Figure 5.22(b). Figure 5.23 shows the SPLAT simulations for an opaque defect at 0.2 μm from the corner. The squares follow approximately the 30% threshold at best focus dose. The fact that the defects print when they are underexposed by a small amount shows a deviation from the intensity threshold model. This deviation again appears to be due to non-vertical resist dissolution phenomena. Figures 5.24 and 5.25 show the transparent and opaque square areas with defects collinear with the edges of the squares. Again three cases are shown for each polarity. The transparent defects do not print (Figure 5.24). The opaque defects are more severe when they are underexposed than when they are printed at best dose. A 3 μm defocus does slightly reduce the printability of these defects.

Category[4]:   Figures 5.26(a)/5.27(a) and 5.28(a)/5.29(a) show the SEM photographs of a transparent/opaque elbow with a 0.5 x 0.5 μm opaque/transparent defect placed at a critical location on the elbow. Figures 5.26(b), 5.27(b), 5.28(b), and 5.29(b) are the underexposed versions of the (a)s'. Underexposure appears to have reduced the susceptibility of opaque elbows to transparent defects but at the expense of increasing the effects of opaque defects on transparent elbows.

Category[5]:   Shown in Figures 5.30 and 5.31 are the two polarities of the worst case of defects near nested elbows. Three different situations are shown: best focus and dose, best focus underexposed, and best dose 3 μm defocus. In the transparent case, No significant difference is observed in the three situations. The defect near the outermost elbow does print in all three situations whereas the defect between elbows does not. In the opaque case (Figure 5.31), at best focus dose, a defect near the outermost elbow has the same effect as when it is between elbows, and as before, underexposure increases the printability of defects. At best dose, 3 μm defocus reduces the susceptibility of the outermost elbow to defect while at the same time increases the effect of the defect between elbows. This effct is also observed in the patterns printed on Al substrate (Figure 5.32).

3. Evaluation

3.1. Observations

1.   Small (< 0.4 λ/NA) opaque and transparent defects have similar effects.

2.   Opaque defects > 0.4 λ/NA have a more significant effect on linewidth variation than transparent defects.

3.   On the same mask, underexposure dramatically increases the printability of opaque defects and somewhat reduces that of transparent defects.

4.   Corner defects up to 0.3 λ/NA do not print unless they are underexposed.

5. Opaque defects centered between features at minimum spacing (0.8 λ / NA) bridge at a size of 0.35 λ / NA.

6. The worst possible case from the targets printed is an opaque defect located in the extension of a corner in a line. This case is worse than between lines due to the intensity minima near the corner.

7. The printability of defects near features is approximately the same for Si and Al substrates.

3.2. Recommendations

1. Patterns with opaque defects in contacts should be included as they will likely be the overall worst defect locations.

2. A smaller exposure step should be used.

3. The effect of post exposure bake should be explored.

4. Defects of various shapes but equal area should be included to verify that for dimensions smaller than 0.3 λ/NA, the defect interaction depends only on defect area.

5. A larger variety of spacing should be considered.

6. Automatic sizing from printed defect images should be investigated.

Chapter 6

Conclusion

An exploratory study of exposure, focus, and defects test patterns has been completed. These patterns were printed on three different types of substrates to explore the parameter effects of resist thickness and substrate reflectivity. Visual inspection with a low power optical microscope has shown that the exposure and focus patterns are sensitive enough to be used to determine the best exposure time and focus position respectively on both Si and Al substrates. Corrections for mask masking bias are necessary in calibration of these targets. The patterns printed on Si with thin resist are totally insensitive to dose and focus variations. Good agreement with simulation and experiment was obtained for the exposure targets and the focus targets showed deviations from a threshold intensity model due to non-vertical resist dissolution. The focus targets are still usable for detecting best focus position. SEM photographs of the printed defect patterns agree with modeling predictions that opaque defects centered between features are significantly worse than the transparent defects and contribute bridging at a size of 0.35 λ/NA for a spacing of 0.8 λ/NA. Defects near a corner in a line are slightly worse due to low intensity there. Since clear contacts suffer from low intensity, it is anticipated that defects in contacts may be the overall most critical location for defects. The printability of defects on Al and Si appears to be similar.

Acknowledgement

References

1. Christopher P. Ausschnitt, "Electrical Measurements for Characterizing Lithography," in *VLSI Electronics : Microstructure Science*, ed. N.G. Einspruch and R.K. Watts, vol. 16, Academic Press, Inc., Orlando, Florida, 1987.

2. Wolfgang Arden and Dietrich Widmann, *Method of Rapid Indirect Determination of Photoresist Linewidths in Optical Projection Printing*, April 6, 1987. Patent # DE 3305977 C2

3. A.R. Neureuther private communication.

4. P.D. Flanner III, *Two-Dimensional Optical Imaging for Photolithography Simulation*, University of California, Berkeley, May 12, 1986. M.S. Thesis

5. Kenny K.H. Toh, *Simulation of Projection Lens Aberrations via TCCs*, University of California, Berkeley, September 24, 1987.

6. W.G. Oldham, S.N. Nandgaonkar, A.R. Neureuther, and M.M. O'toole, "A General Simulator for VLSI Lithography and Etching Processes: Part I - Application to Projection Lithography," *IEEE Trans. on Electron Devices*, vol. ED-26, pp. 717-722, April 1979.

7. W.G. Oldham, A.R. Neureuther, Rolfe Anderson, Uathavikul Bordin, Dean Drako, William Haller, Bachvan Huynh, Don Lyons, George Misium, Davor Sutija, and Kenny Toh, *Berkeley CMOS Process Test Patterns*, University of California, Berkeley. Forthcoming ERL Memorandum

8. Vincent Mastromarco, A.R. Neureuther, and Kenny Toh, "Printability of Defects in Optical Lithography: Polarity and Critical Location Effects," *Vacuum Science Technology B*, February 1988.

Size (µm)		Pitch (µm)		Transmission	
x	y	x	y	Dark Field	Bright Field
0.2	0.2	0.8	0.5	1.0%	...
0.3	0.2	0.8	0.5	2.3%	...
0.4	0.2	0.8	0.5	4.0%	...
0.3	0.3	0.6	0.6	6.3%	...
0.3·	0.3	0.6	0.5	9.0%	...
0.4	0.3	0.7	0.5	11.8%	...
0.4	0.3	0.6	0.5	16.0%	...
0.4	0.4	0.6	0.6	19.8%	...
0.6*	0.3	0.6	0.6	...	25.0%
0.4	0.4	0.6	0.6	...	30.9%
0.4	0.3	0.6	0.5	...	36.0%
0.4	0.3	0.7	0.5	...	43.2%
0.3	0.3	0.6	0.5	...	49.0%
0.3	0.3	0.6	0.6	...	56.3%
0.4	0.2	0.8	0.5	...	64.0%
0.3	0.2	0.8	0.5	...	72.3%
0.2	0.2	0.8	0.5	...	81.0%

Table 3.1. Exposure pattern sizes and transmission values

*checkerboard pattern is used in this area. In order to use the same formula to calculate the transmitted intensity, the size in x is doubled.

Algebraic vs Rigorous Model							
Size (μm)		Pitch (μm)		Transmission			
				Algebraic Calculation		SPLAT Simulation	
x	y	x	y	Dark Field	Bright Field	Dark Field	Bright Field
0.2	0.2	0.8	0.5	1.0%	...	1.0%	...
0.3	0.2	0.8	0.5	2.3%	...	2.2%	...
0.4	0.2	0.8	0.5	4.0%	...	4.0%	...
0.3	0.3	0.6	0.6	6.3%	...	6.2%	...
0.3	0.3	0.6	0.5	9.0%	...	9.0%	...
0.4	0.3	0.7	0.5	11.8%	...	11.8%	...
0.4	0.3	0.6	0.5	16.0%	...	16.0%	...
0.4	0.4	0.6	0.6	19.8%	...	19.8%	...
0.6	0.3	0.6	0.6	...	25.0%	...	25.0%
0.4	0.4	0.6	0.6	...	30.9%	...	30.9%
0.4	0.3	0.6	0.5	...	36.0%	...	36.0%
0.4	0.3	0.7	0.5	...	43.2%	...	43.2%
0.3	0.3	0.6	0.5	...	49.0%	...	49.0%
0.3	0.3	0.6	0.6	...	56.3%	...	56.2%
0.4	0.2	0.8	0.5	...	64.0%	...	64.0%
0.3	0.2	0.8	0.5	...	72.3%	...	72.2%
0.2	0.2	0.8	0.5	...	81.0%	...	81.0%

Table 3.2. Comparison of the algebraic and the simulation models

Algebraic vs Rigorous Model (corrected for bias)							
Size (μm)		Pitch (μm)		Transmission			
				Algebraic Calculation		SPLAT Simulation	
x	y	x	y	Dark Field	Bright Field	Dark Field	Bright Field
0.23	0.26	0.8	0.5	2.2%	...	2.2%	...
0.33	0.26	0.8	0.5	4.6%	...	4.6%	...
0.43	0.26	0.8	0.5	7.8%	...	7.8%	...
0.33	0.36	0.6	0.6	10.9%	...	10.9%	...
0.33	0.36	0.6	0.5	15.7%	...	15.7%	...
0.43	0.36	0.7	0.5	19.6%	...	19.6%	...
0.43	0.36	0.6	0.5	26.6%	...	26.6%	...
0.43	0.46	0.6	0.6	30.2%	...	30.2%	...
0.48	0.18	0.6	0.6	...	57.8%	...	57.8%
0.32	0.28	0.6	0.6	...	56.4%	...	56.4%
0.32	0.18	0.6	0.5	...	65.3%	...	65.3%
0.32	0.18	0.7	0.5	...	69.8%	...	69.8%
0.24	0.18	0.6	0.5	...	73.3%	...	73.3%
0.24	0.18	0.6	0.6	...	77.4%	...	77.4%
0.32	0.07	0.8	0.5	...	89.1%	...	89.1%
0.24	0.07	0.8	0.5	...	91.8%	...	91.8%
0.13	0.07	0.8	0.5	...	95.5%	...	95.5%

Table 3.3. Exposure pattern sizes corrected for bias and transmission values

(a) At best focus and dose

Defect Size (μm)	Spacing (μm)	ΔL (μm)
0.3	0.2	0.03
0.5	0.2	0.25
0.6	0.2	0.43
0.6	0.3	0.48
0.6	0.5	0.36

(b) At best focus underexposed

Defect Size (μm)	Spacing (μm)	ΔL (μm)
0.6	0.2	0.60
0.6	0.5	0.90

(c) At best dose 3 μm defocus

Defect Size (μm)	Spacing (μm)	ΔL (μm)
0.6	0.2	0.39

Table 3.4. Measured linewidth variation
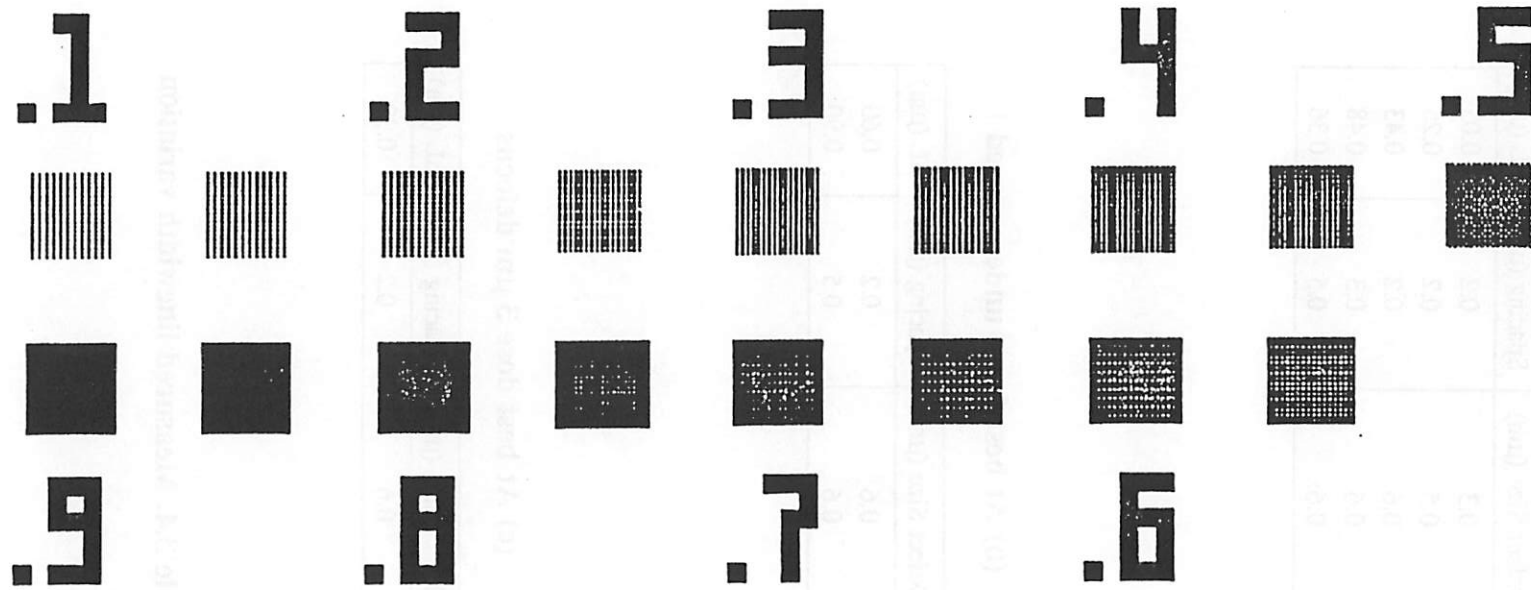
Fig. 3.1. Layout of the exposure monitor
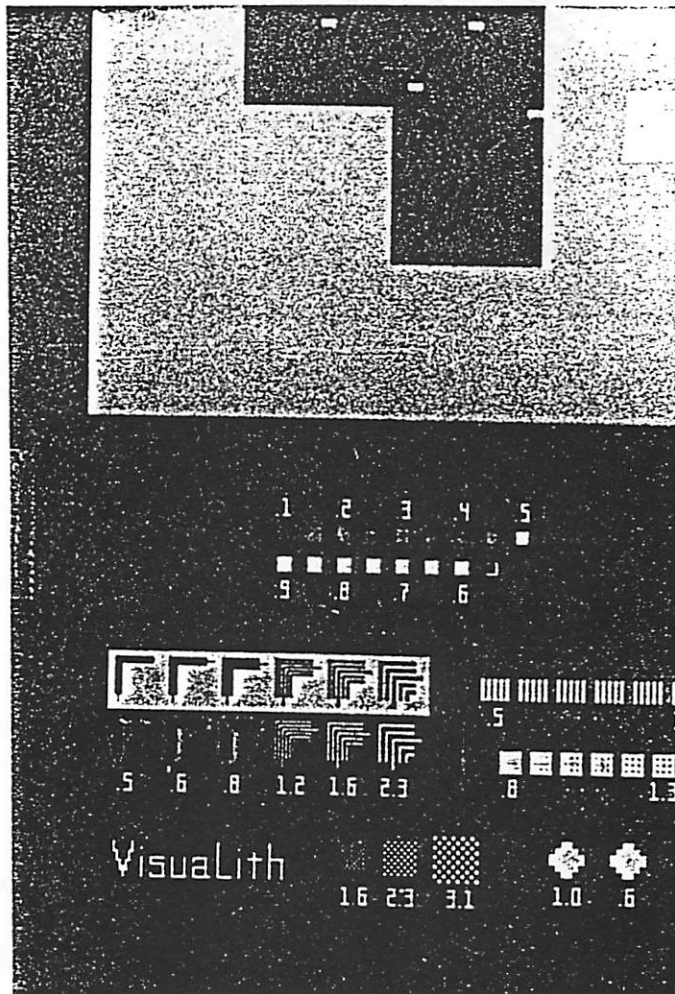
Fig. 3.2. Photograph showing the reversal in the order of clearing of targets

Exposure time = 0.11 sec
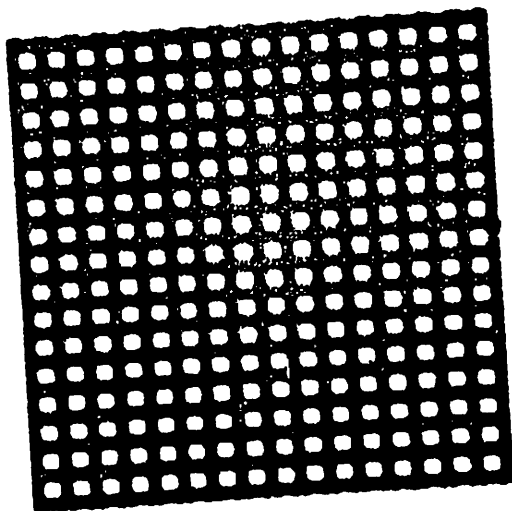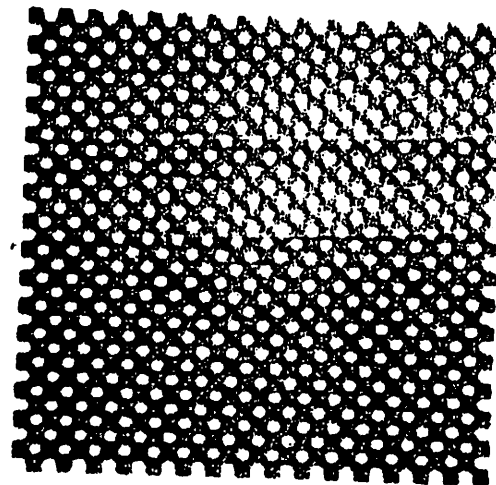
Fig. 3.3. Photographs taken in reflected light showing the severe bias effect on the checkerboard pattern compared to the array pattern
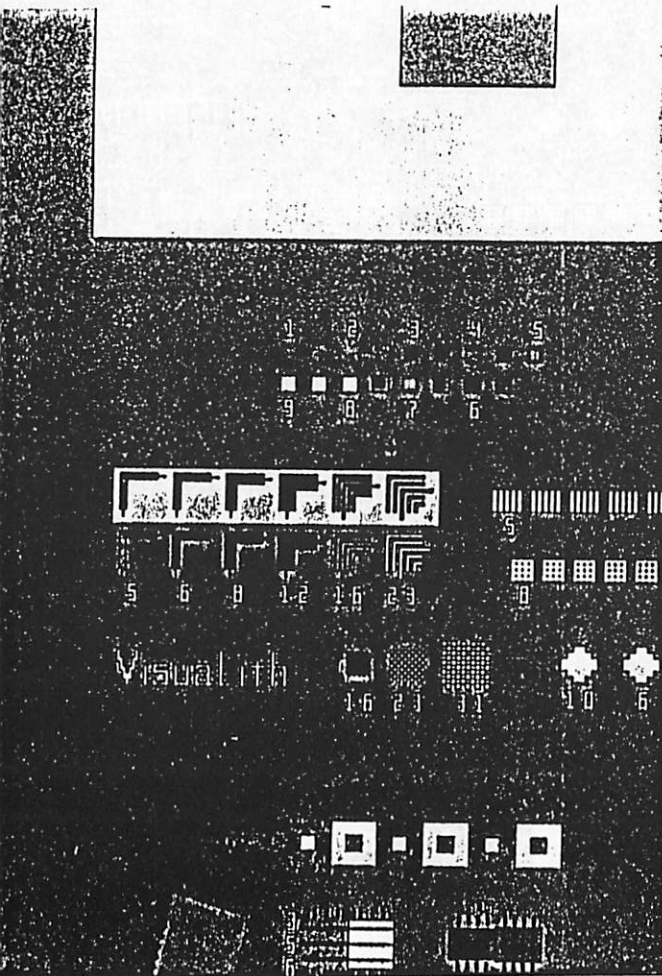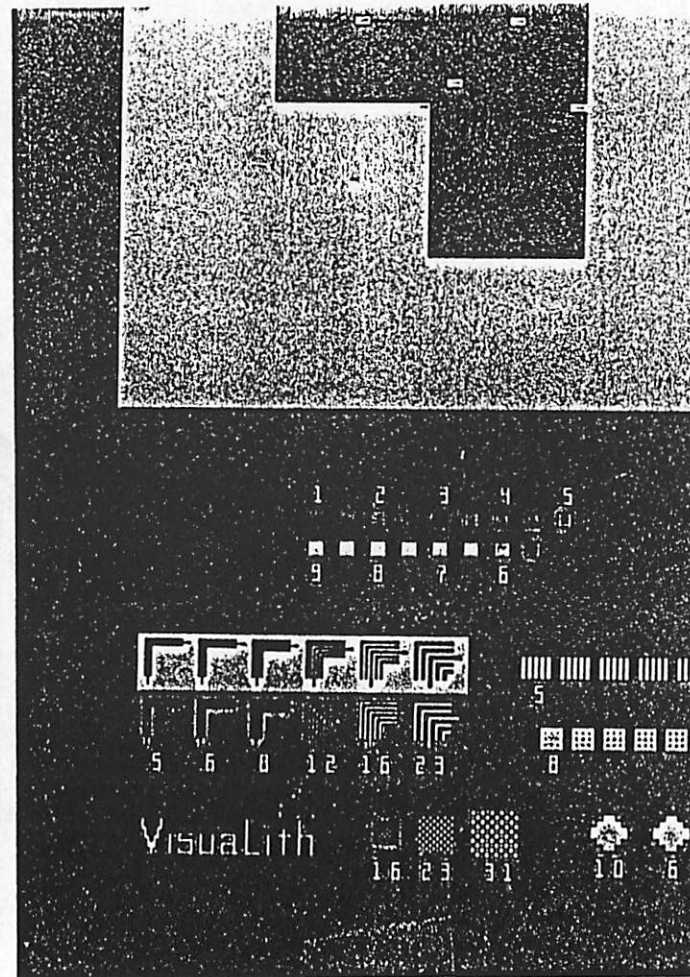
Exposure time = 0.07 sec   **Exposure time = 0.09 sec**   **Exposure time = 0.13 sec**
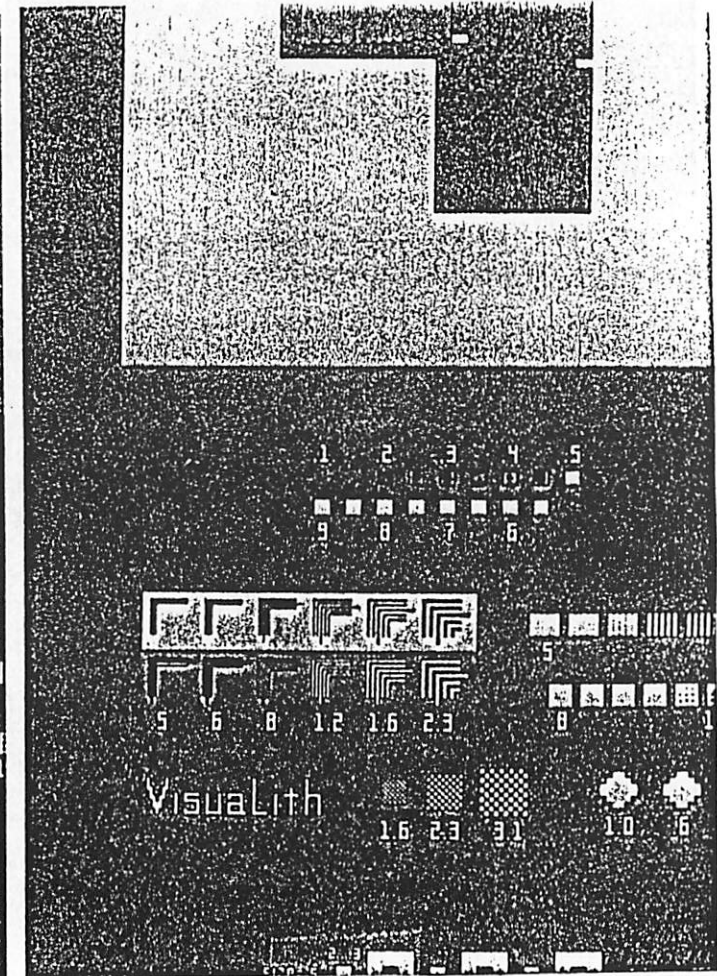
Fig. 3.4. Three photographs of the exposure patterns printed at different
exposure time on Si with 1.2 μm of Kodak 820 resist

Exposure time = 0.07 sec   Exposure time = 0.09 sec   Exposure time = 0.13 sec
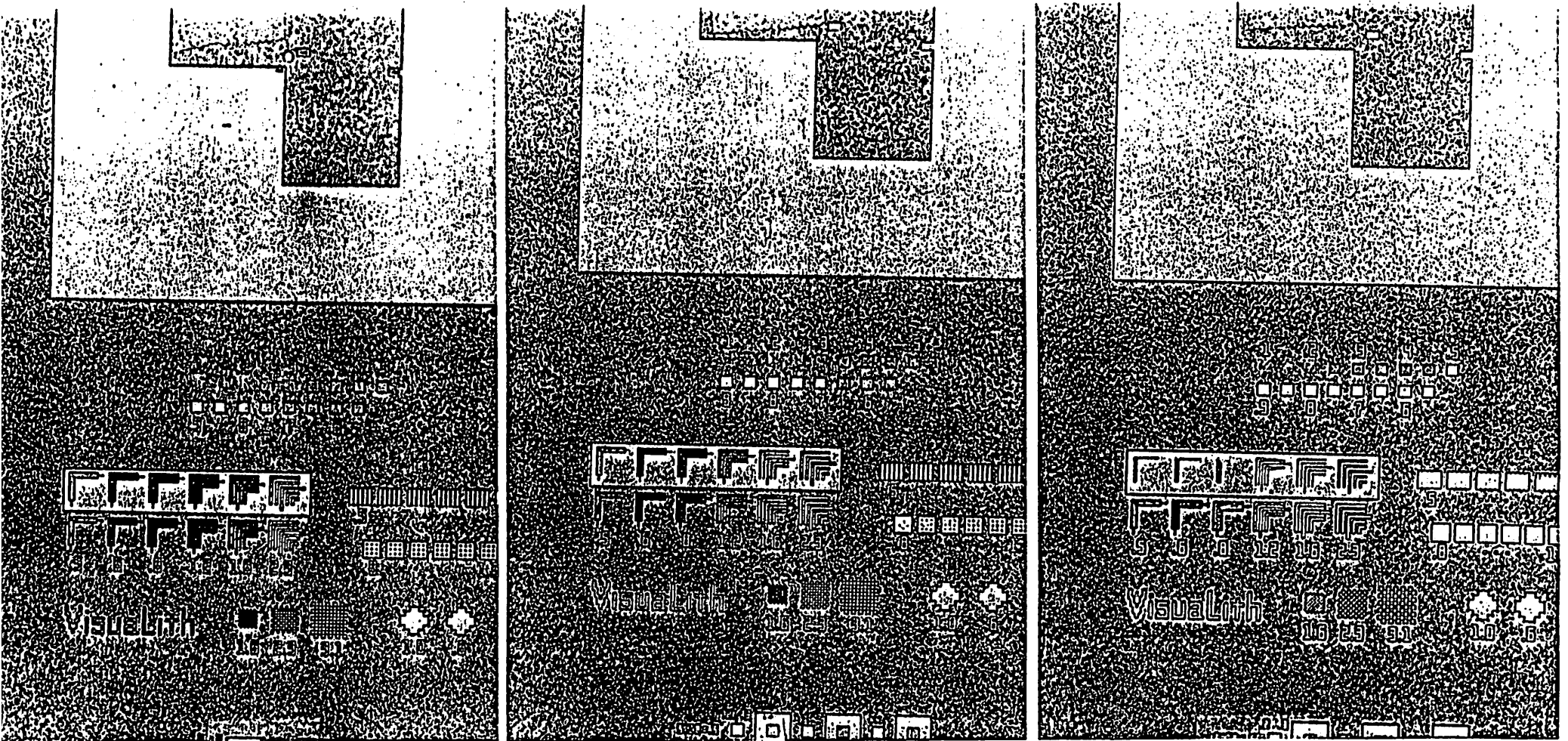
Fig. 3.5. Three photographs of the exposure patterns printed at different exposure time on Al with 1.2 μm of Kodak 820 resist

Fig. 3.6. Number of clear exposure targets for varying exposure time
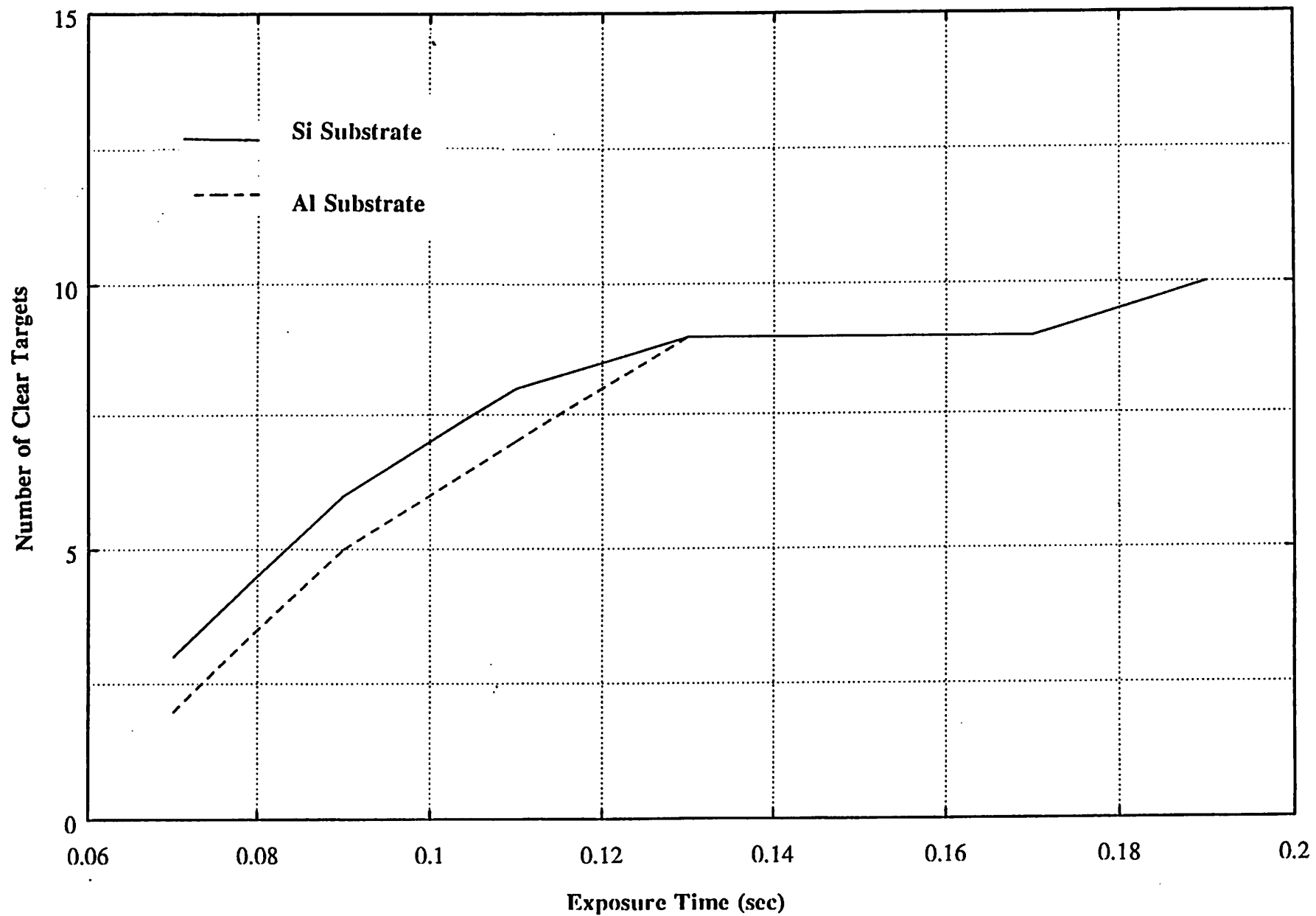
Fig. 3.7. Intensity transmitted to clear at different exposure time for Si substrate
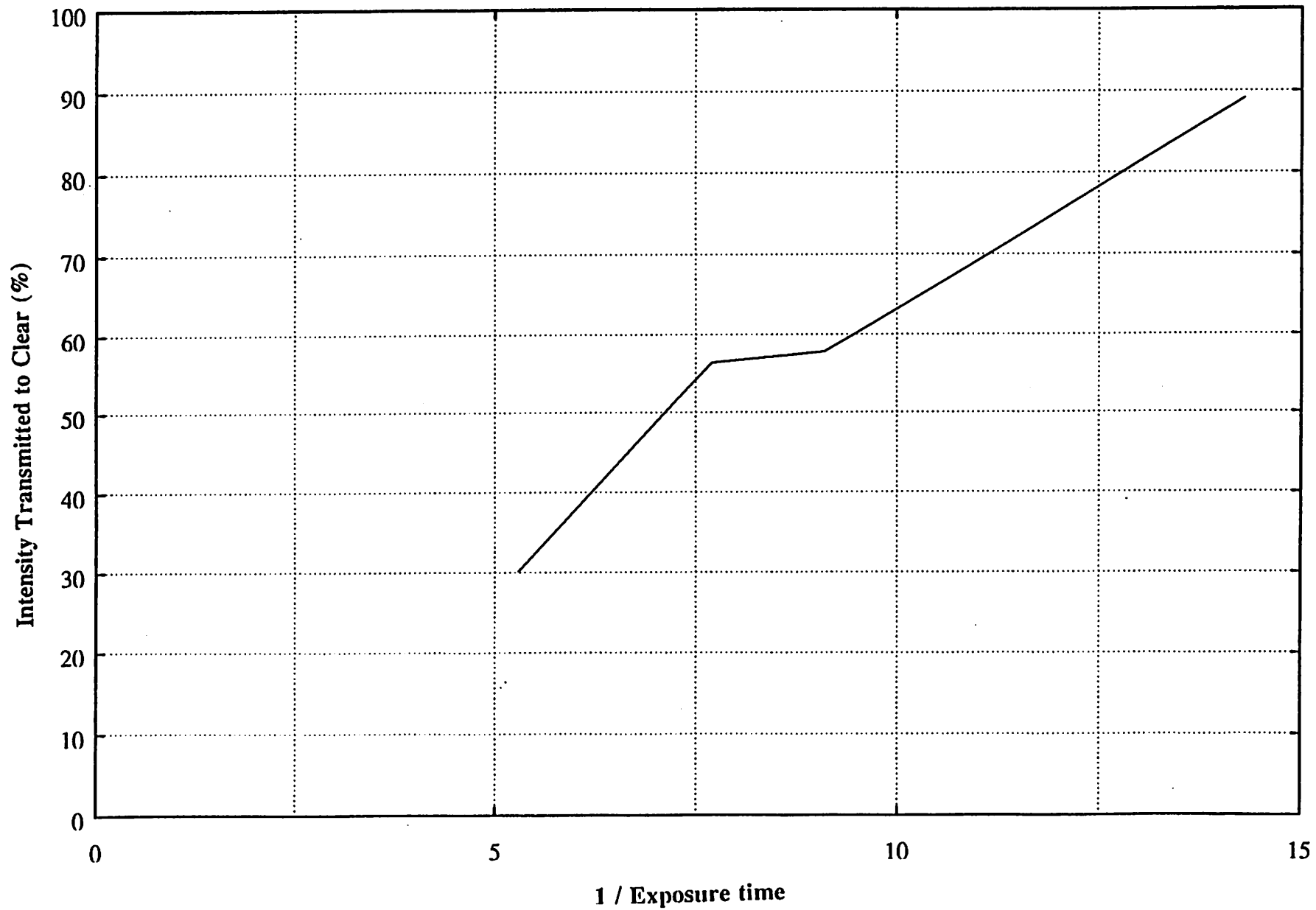
Fig. 3.8. Intensity transmitted to clear at different exposure time for Al substrate
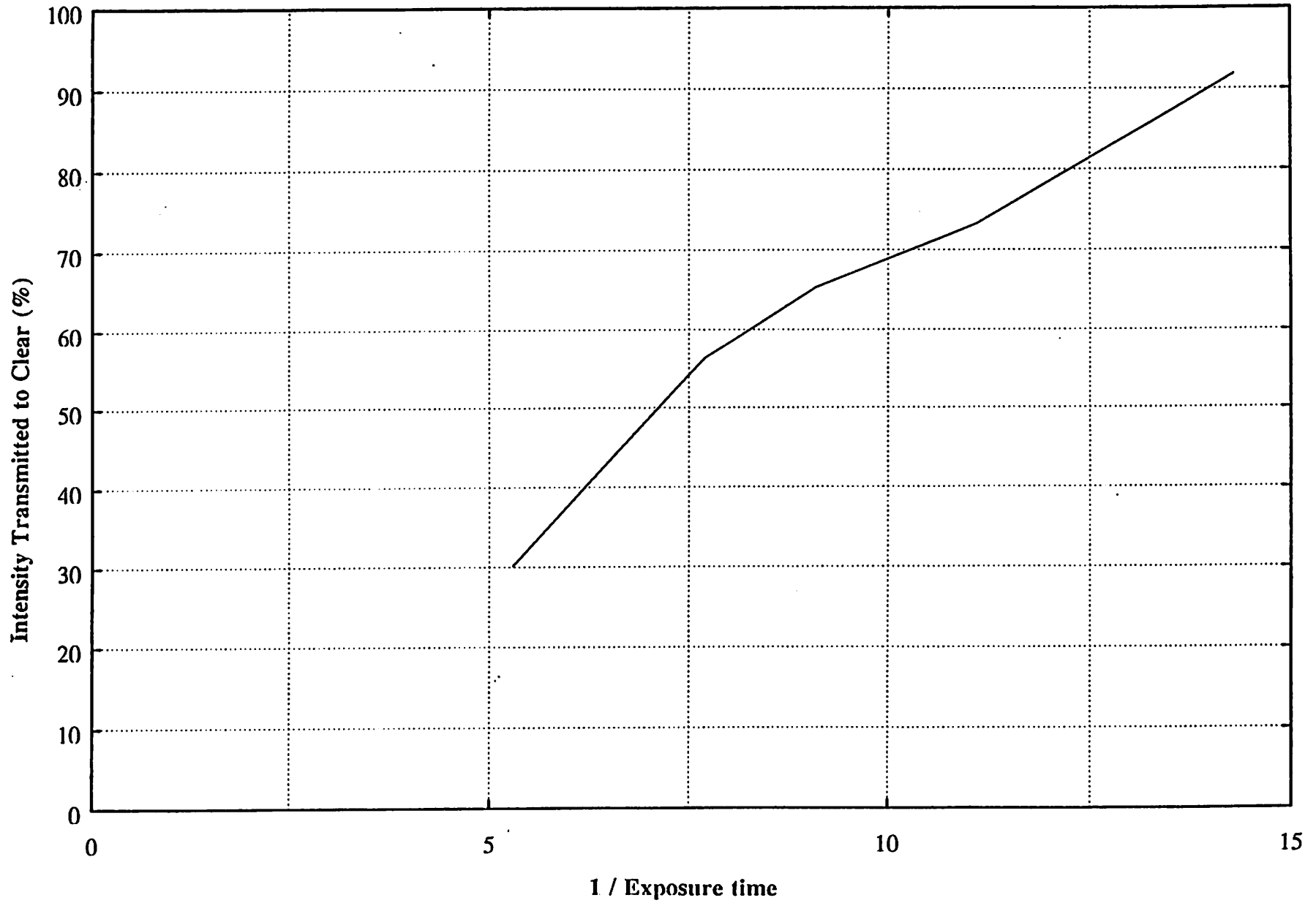
Fig. 4.1. $S_x = 0.5\mu m$
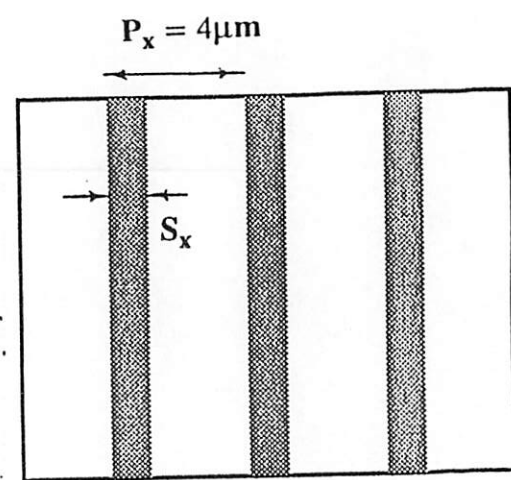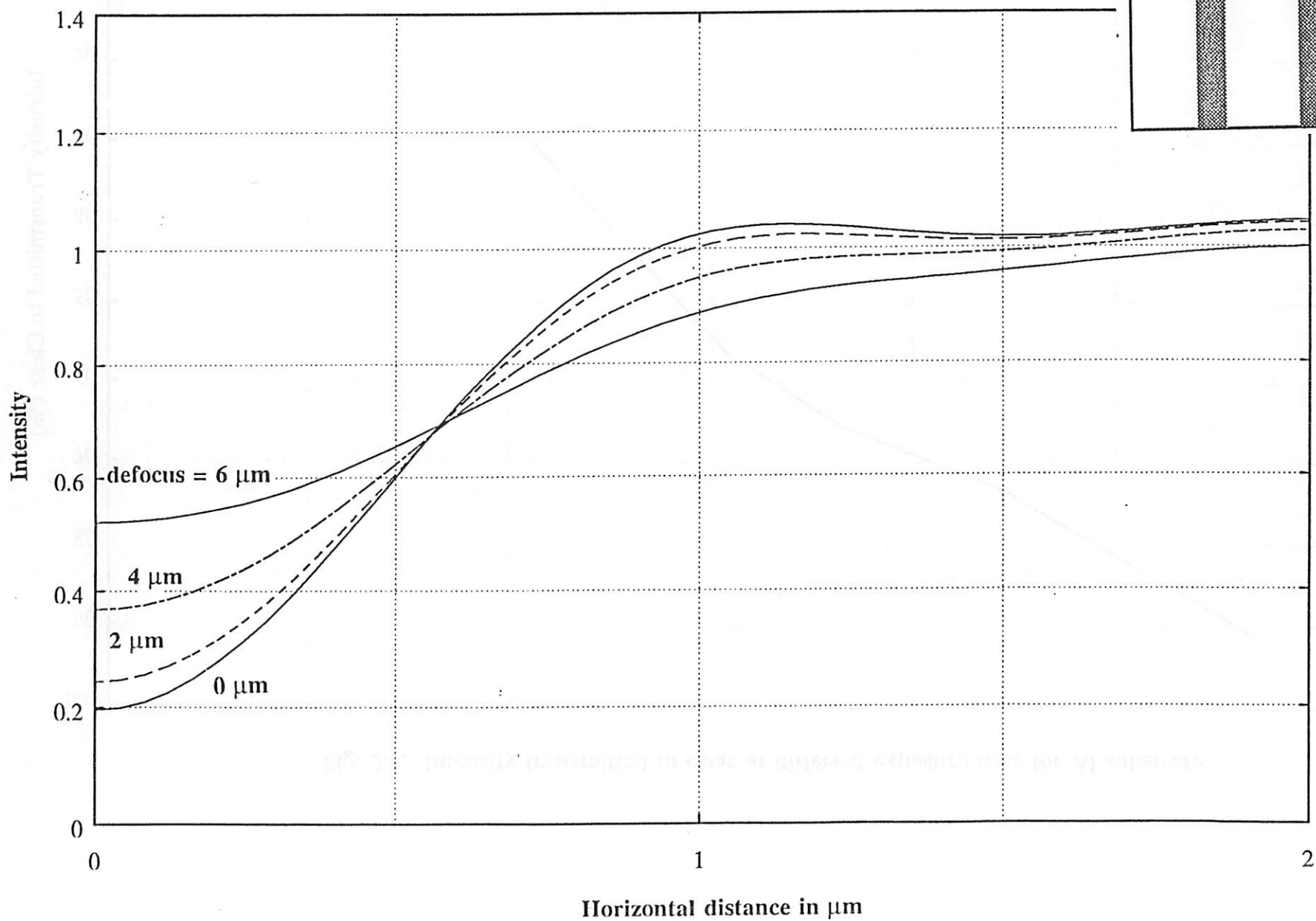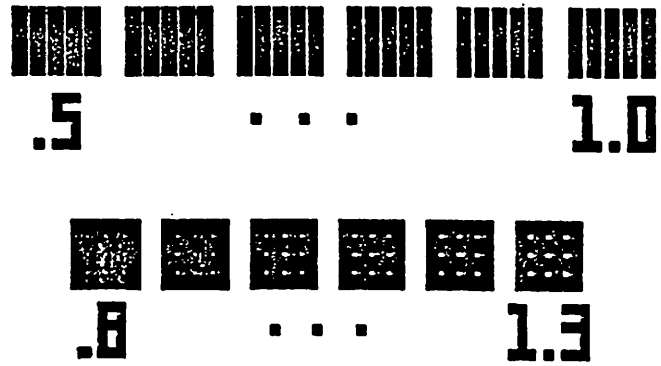
Fig. 4.2. Layout of the focus monitor

Fig. 4.3. 1D intensity design curves
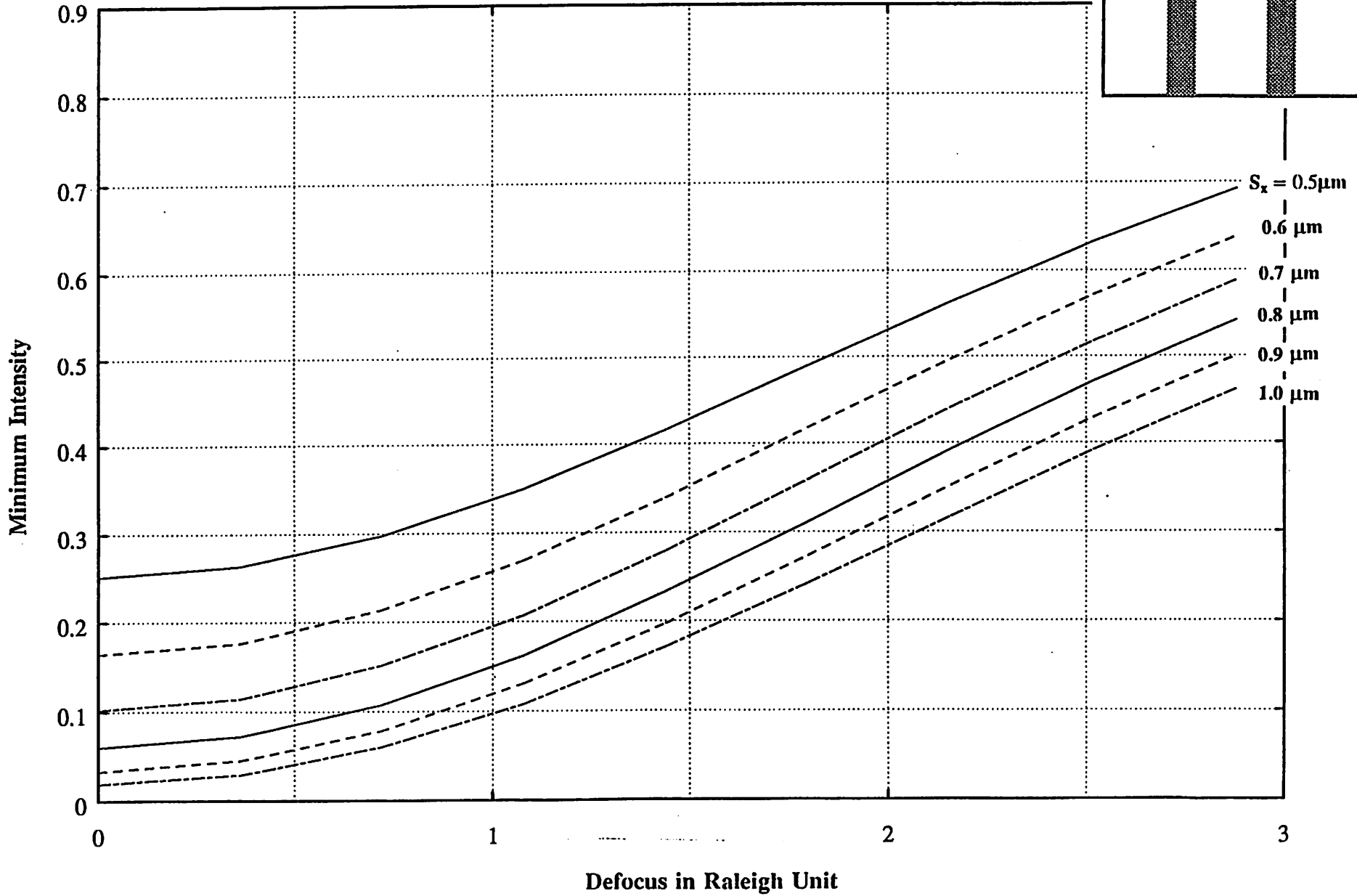
Fig. 4.4. 2D intensity design curves
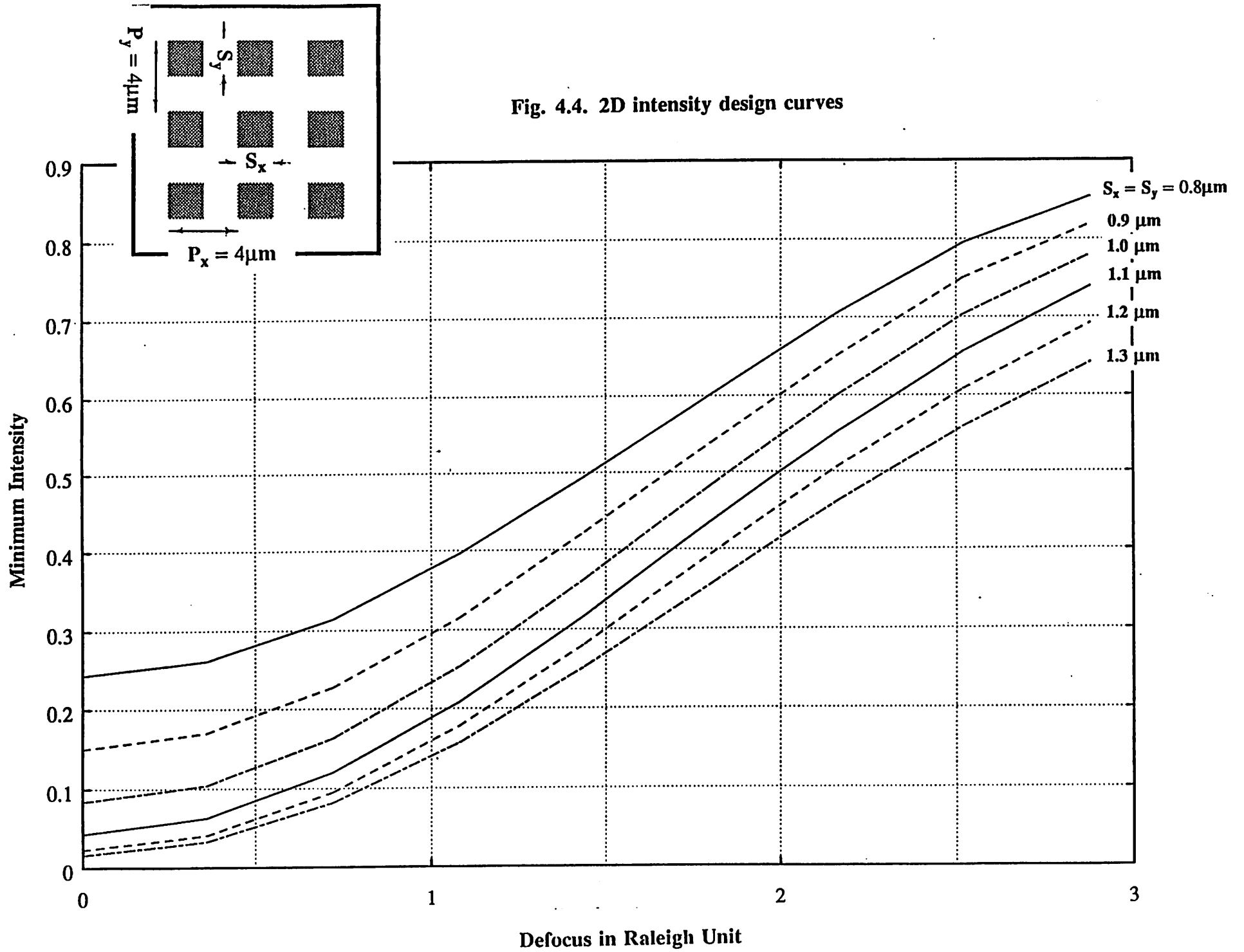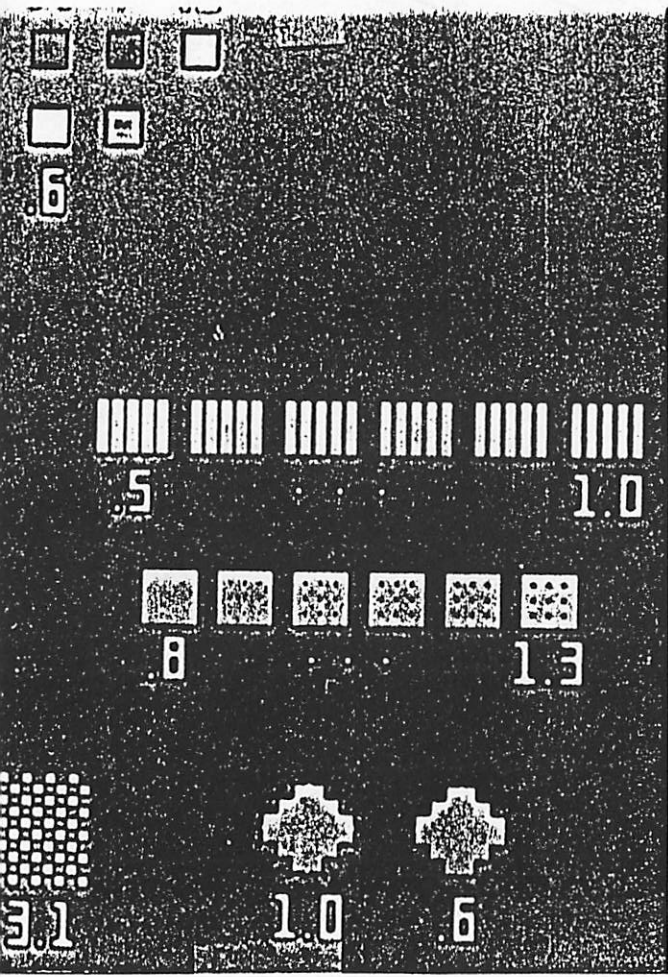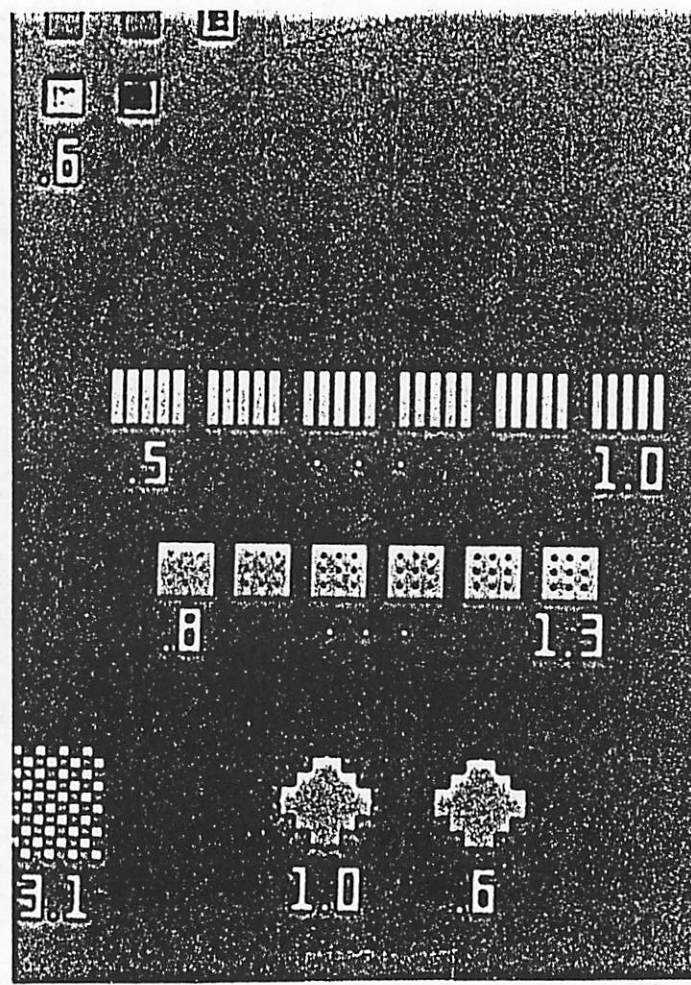
(a) focus position = 282   (b) focus position = 270   (c) focus position = 258
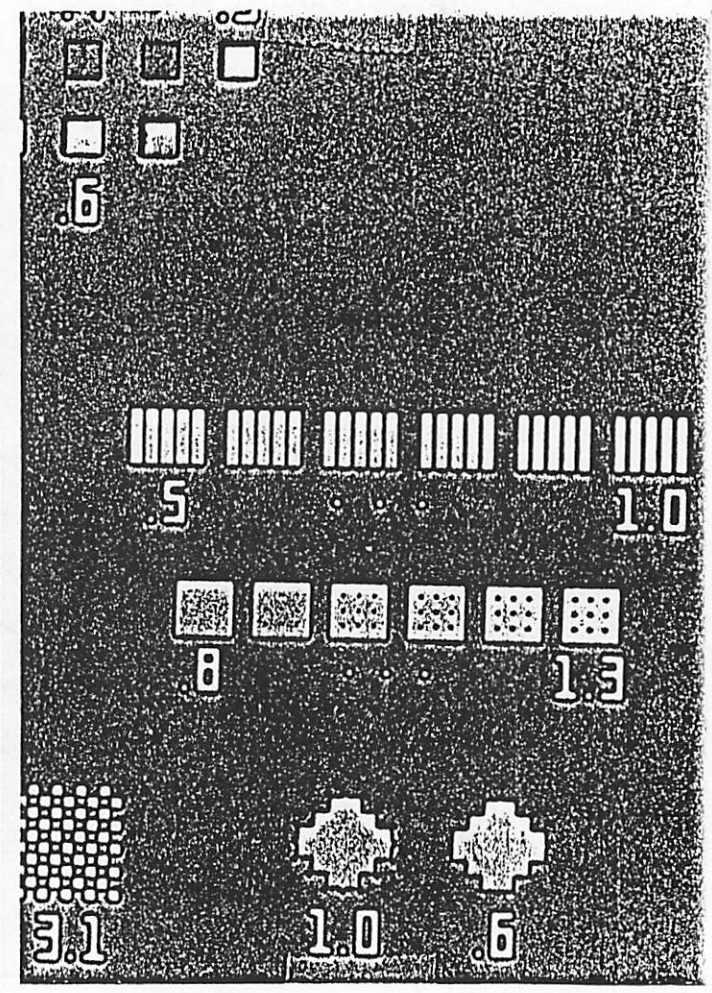
Fig. 4.5. Three photographs of the focus test patterns printed at different focus positions on Si with 1.2 μm of Kodak 820 resist
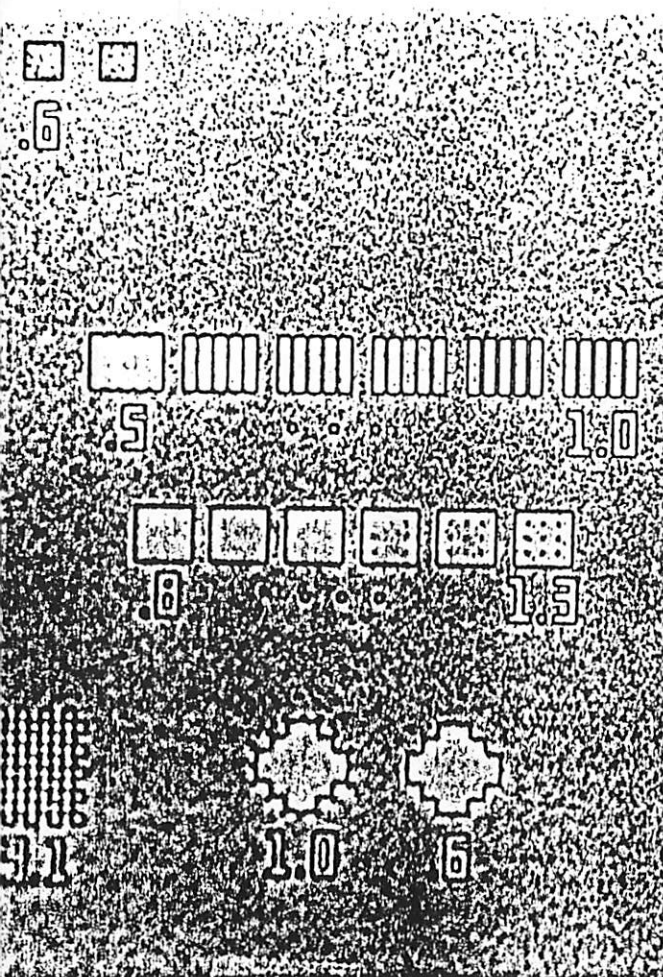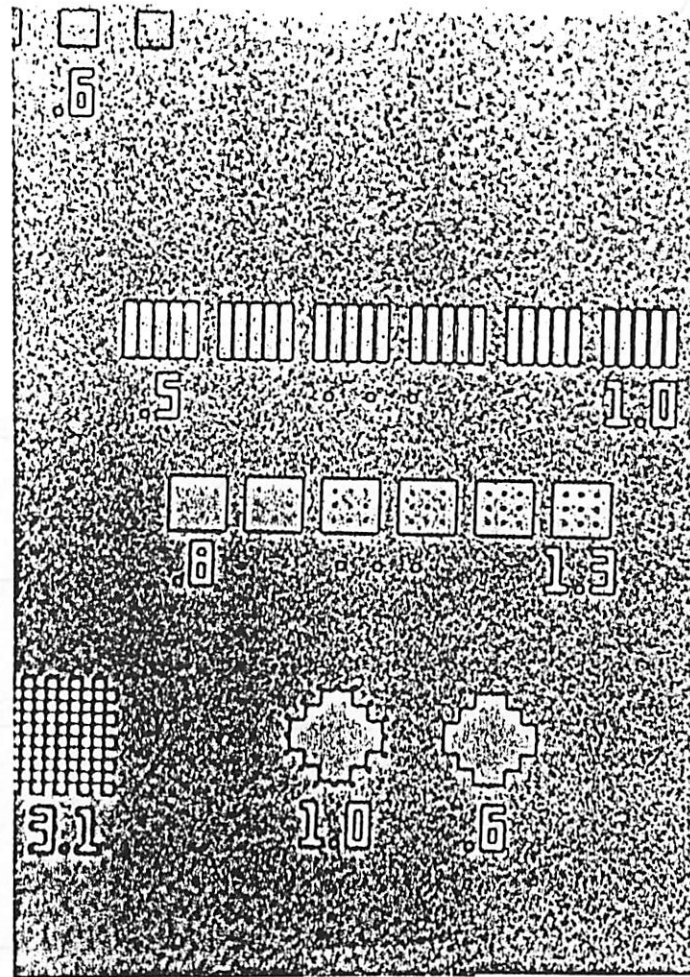
(a) focus position = 282   (b) focus position = 270   (c) focus position = 258
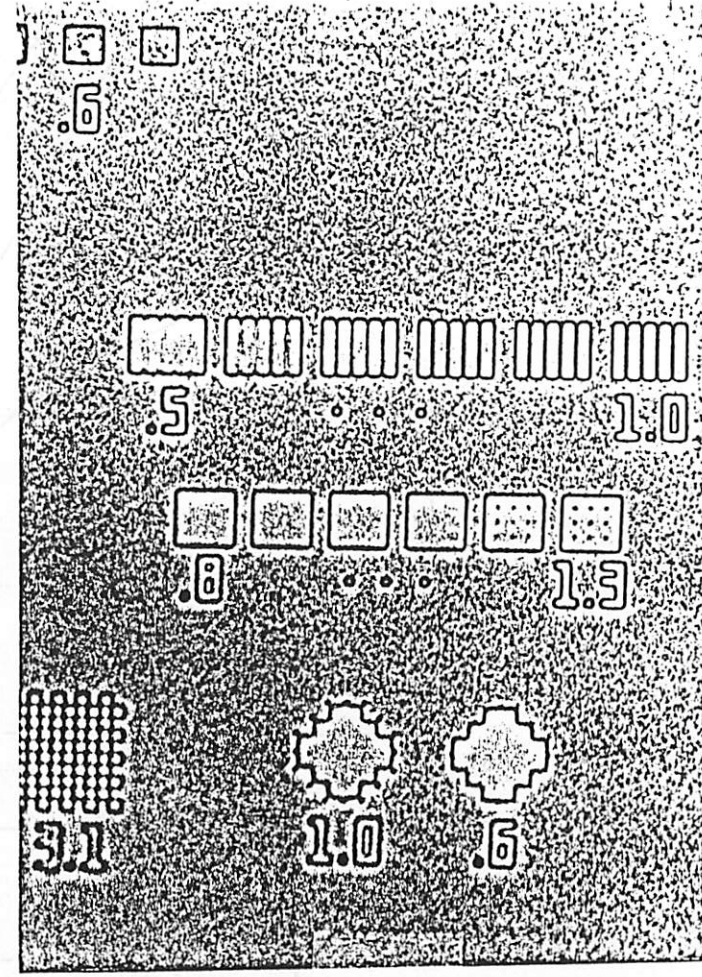
Fig. 4.6. Three photographs of the focus test patterns printed at different focus positions on Al with 1.2 μm of Kodak 820 resist

Fig. 4.7. 1D focus target counts on Si for varying focus positions

- - - - Underexposed

•—•—• 30% Intensity threshold prediction   ——— Best Dose

——* 20% Intensity threshold prediction   — - — Overexposed

1D Target Counts

Operator Best Focus
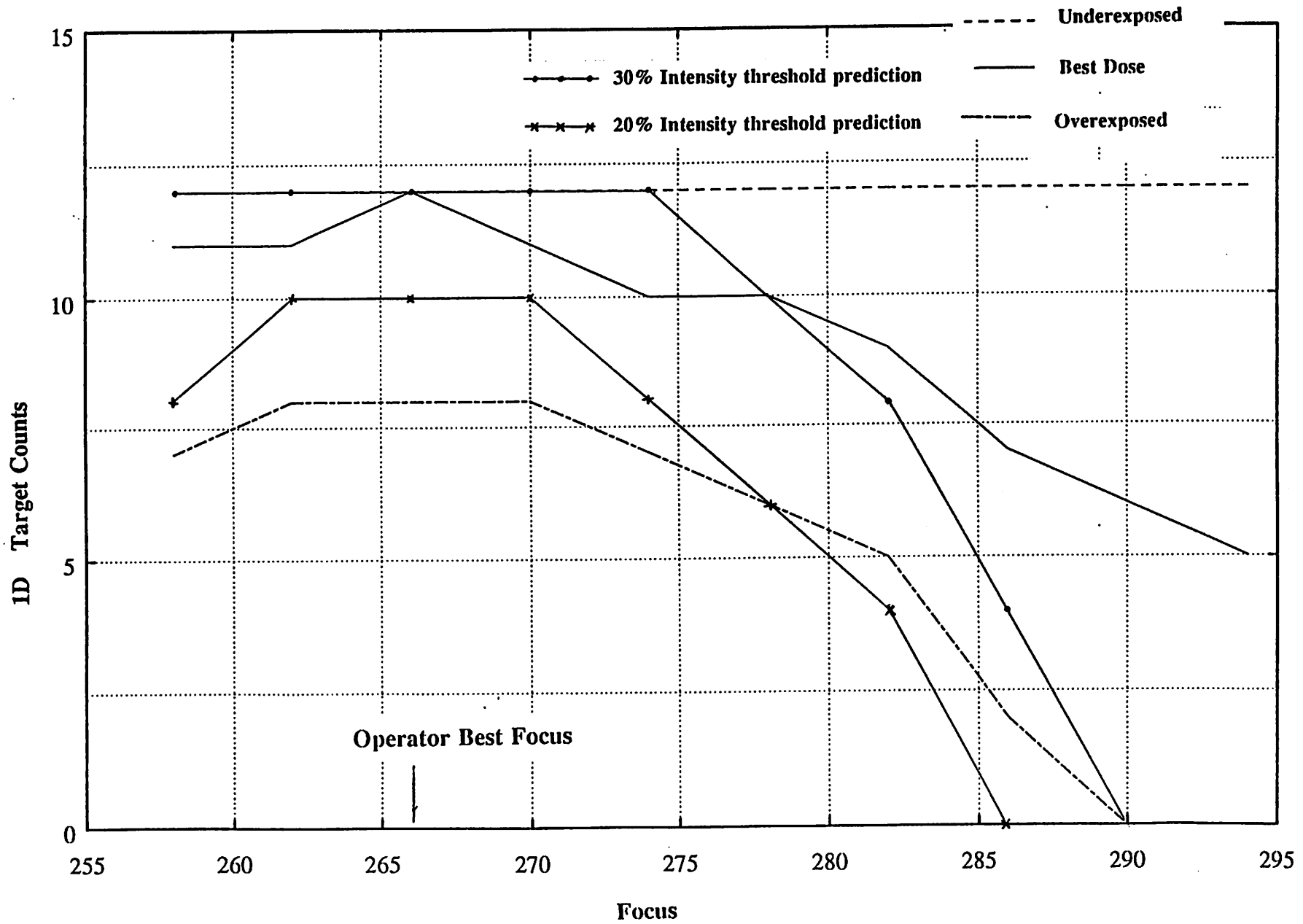
Focus

Fig. 4.8. 2D focus target counts on Si for varying focus positions

Legend:
- •—•—• 30% Intensity threshold prediction
- ✕—✕—✕ 20% Intensity threshold prediction
- —·—·— Underexposed
- — — — Best Dose
- ——— Overexposed

Y-axis: 2D Target Counts (0, 5, 10, 15)

X-axis: Focus (255, 260, 265, 270, 275, 280, 285, 290, 295)

Operator Best Focus

(c)

(a)

(b)
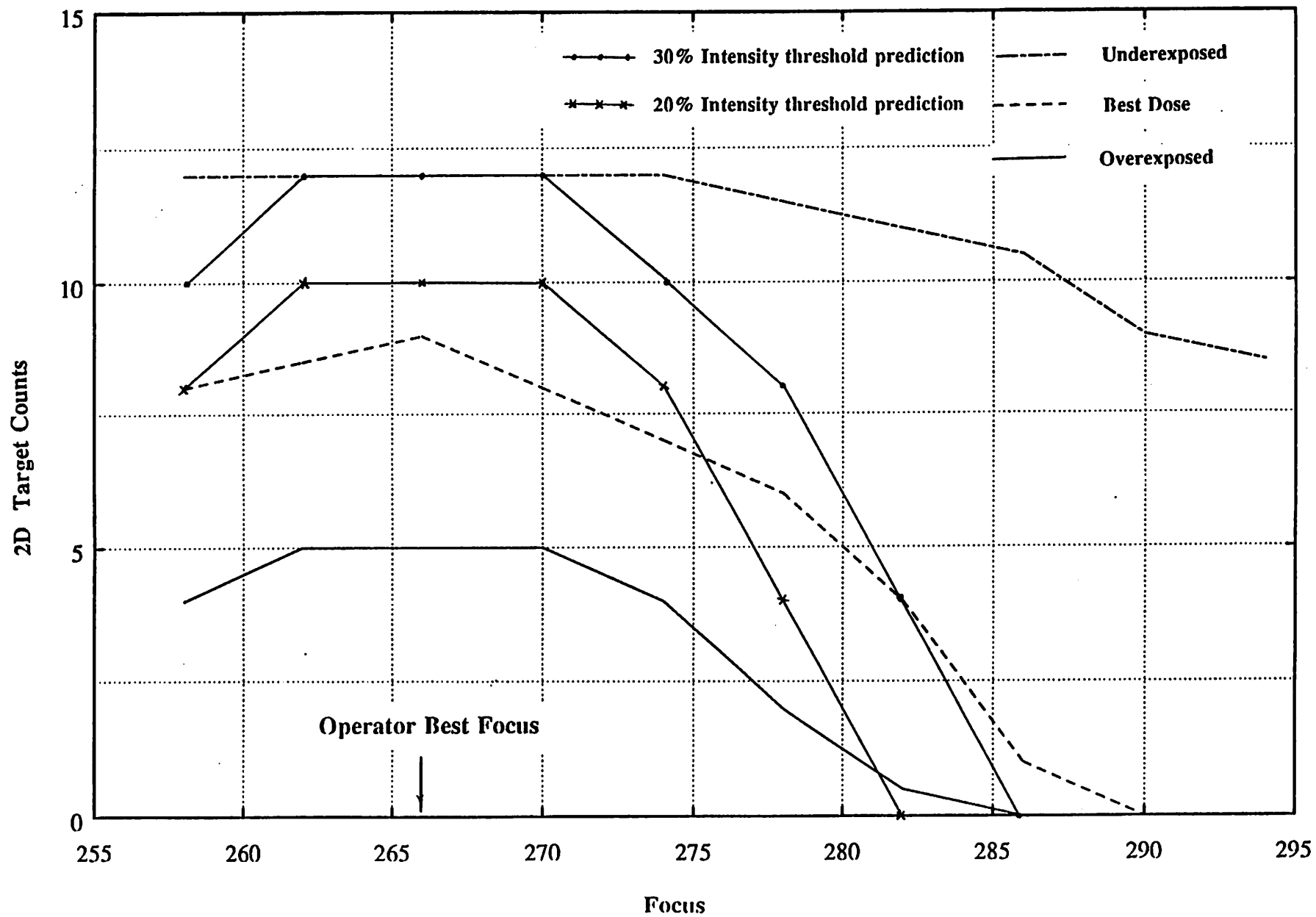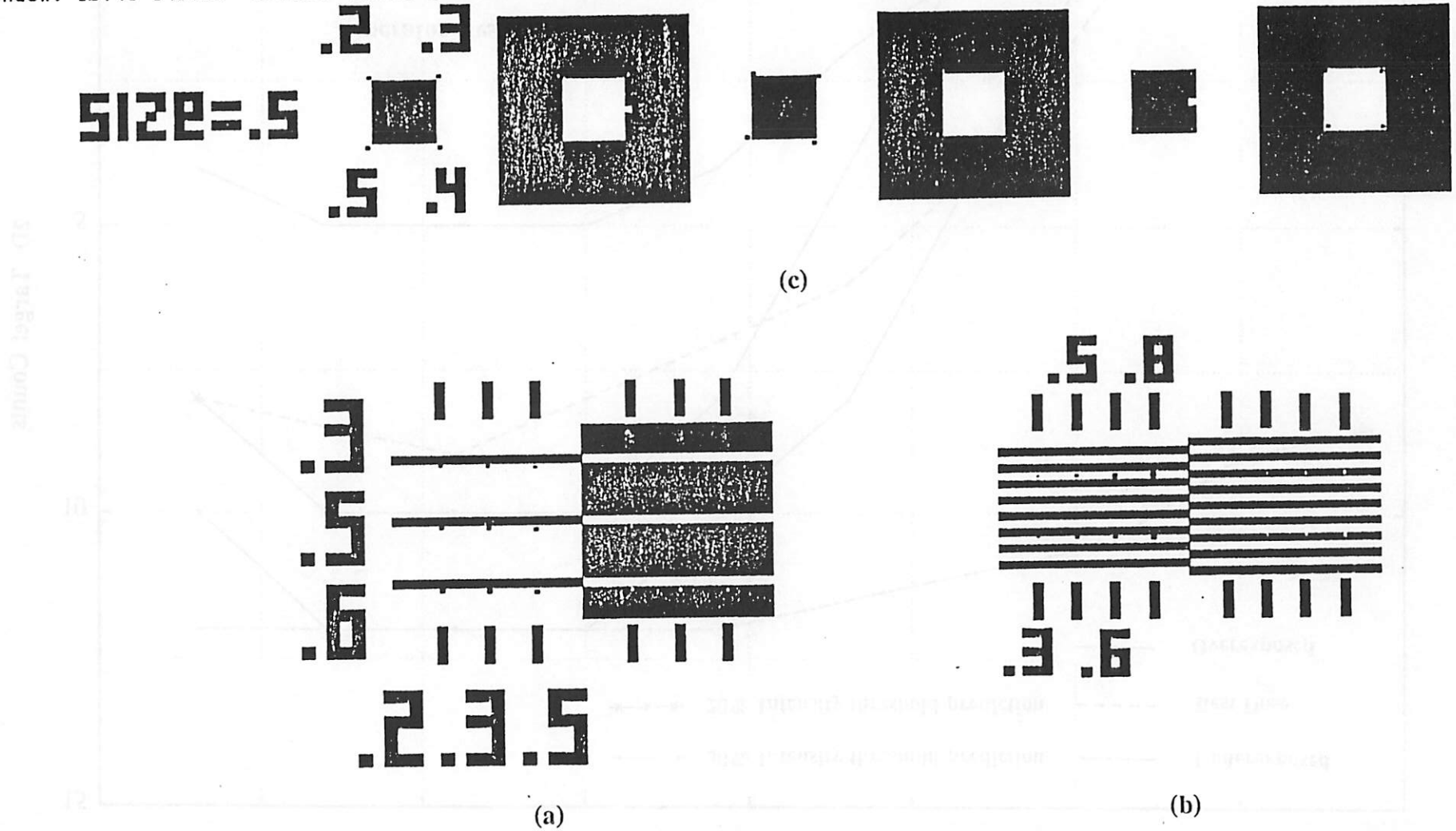
Fig. 5.1. Layout of the defect patterns
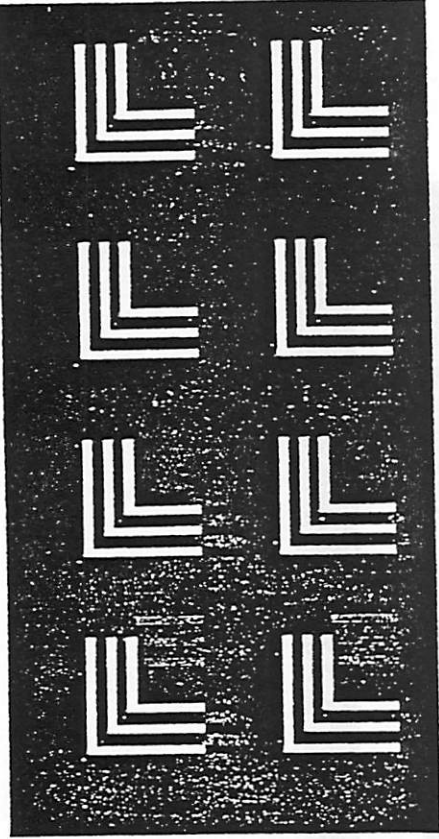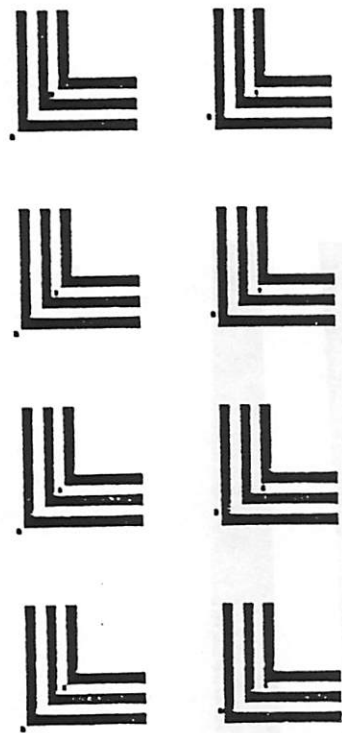
(e)
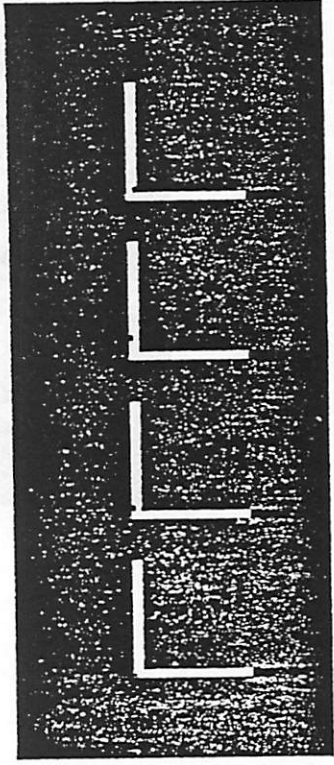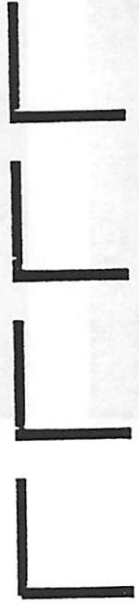
(d)

Fig. 5.1.
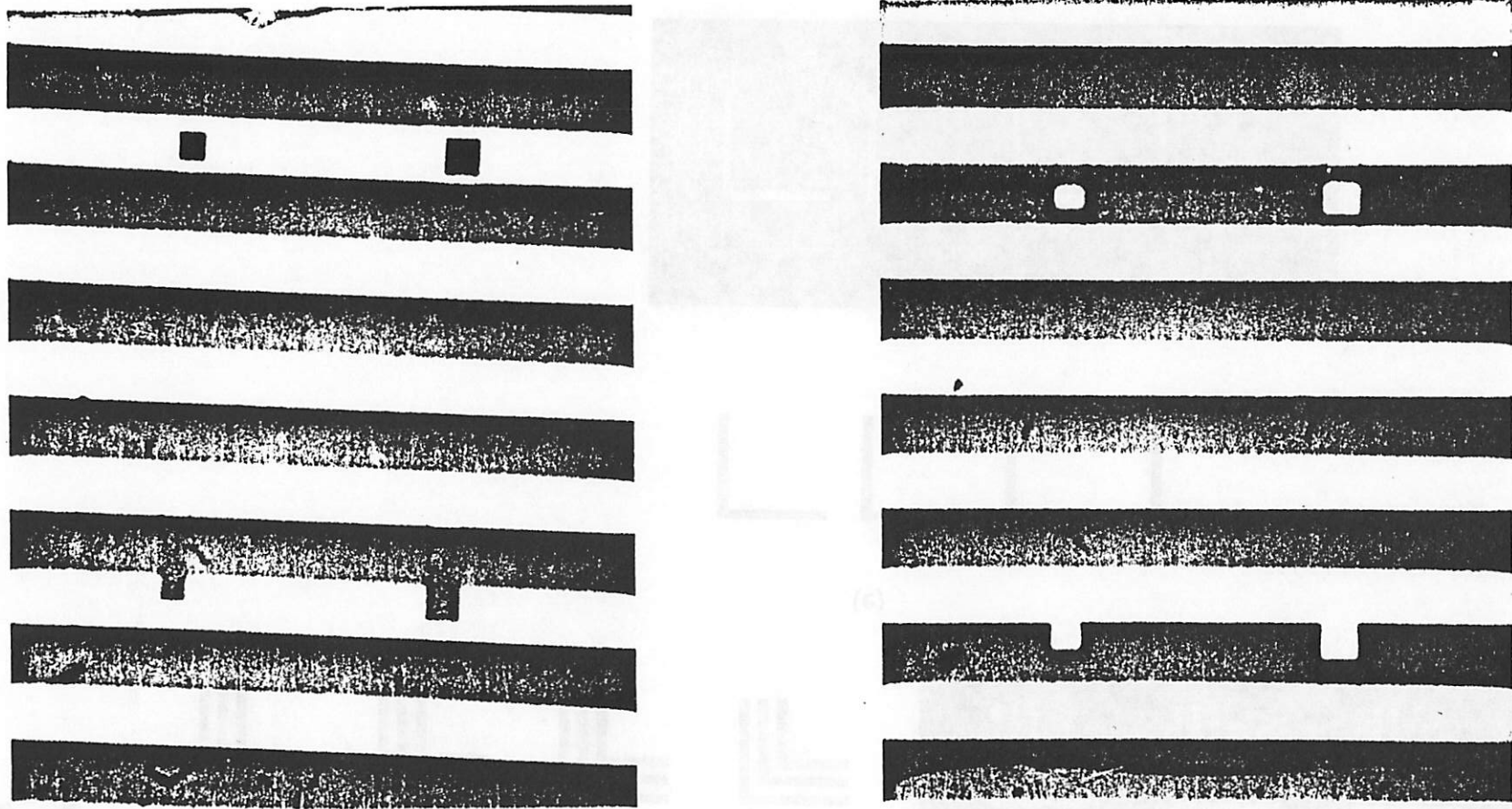
Fig. 5.2. Photographs of the mask taken in reflected light showing different bias effect on opaque and transparent defects

(a) At best focus and dose , L=1.7μm S=0.9μm
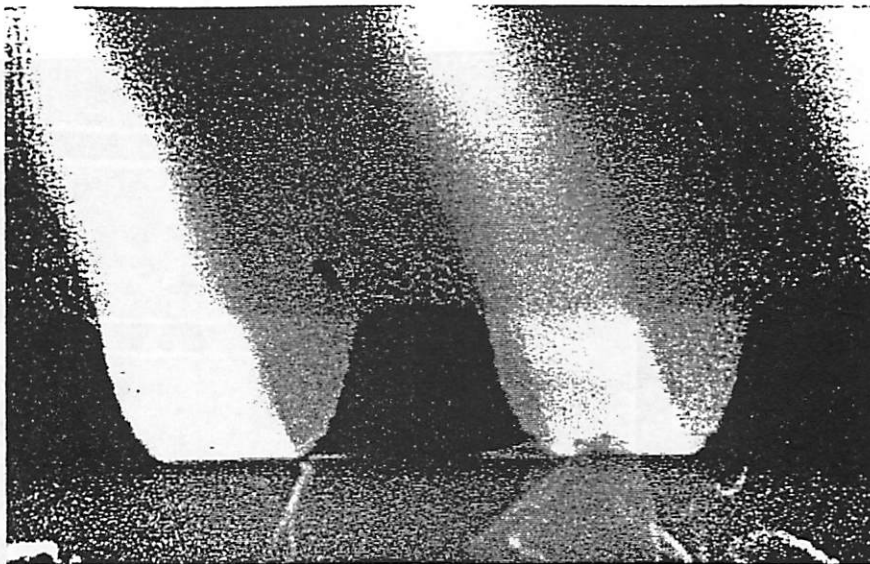
(b) At best focus underexposed , L=1.82μm S=0.67μm

(c) At best dose 3 μm defocus , L=1.76μm S=0.87μm


```
1 Micron ━━━━
Accel: 19.96Kv   Mag:   17.07Kx
Width:  0.874 Microns   Test ID: LINES   Sample ID: RESIST ON SI
```
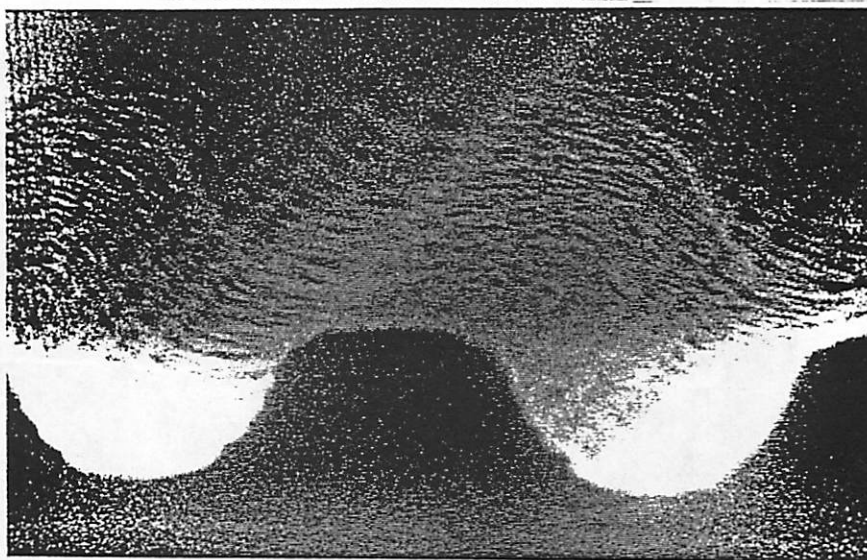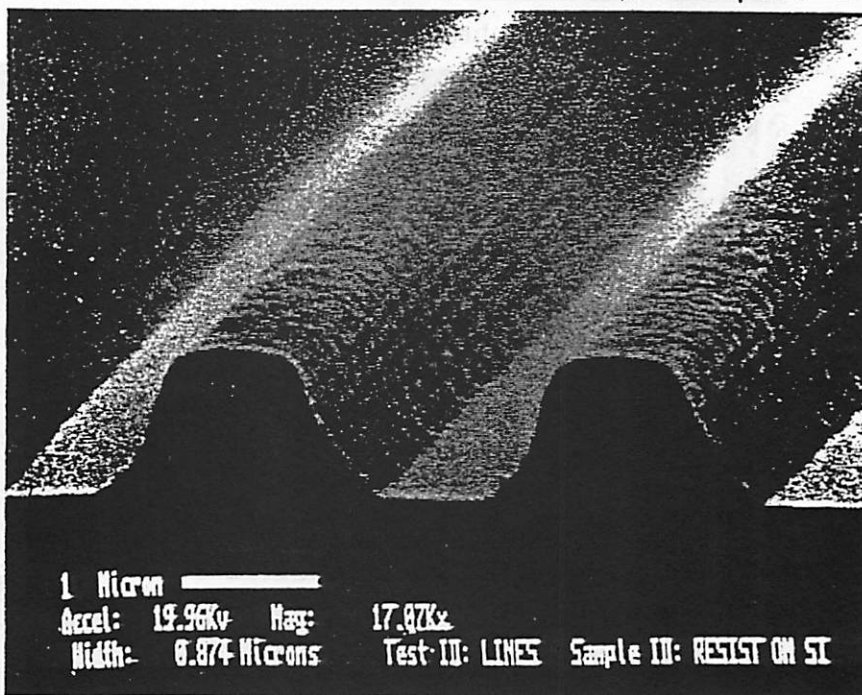
Fig. 5.3. Resist profile for line = space = 1.3 μm
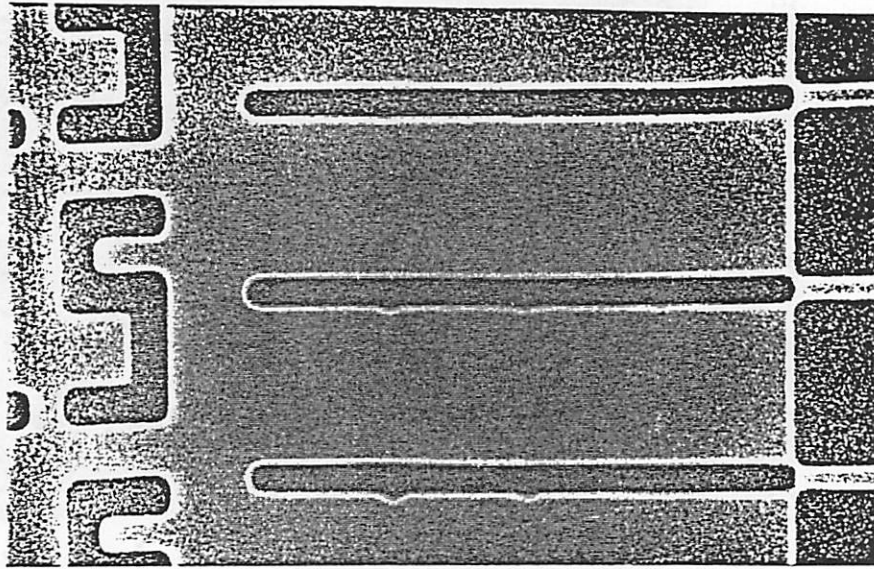
(a) At best focus and dose
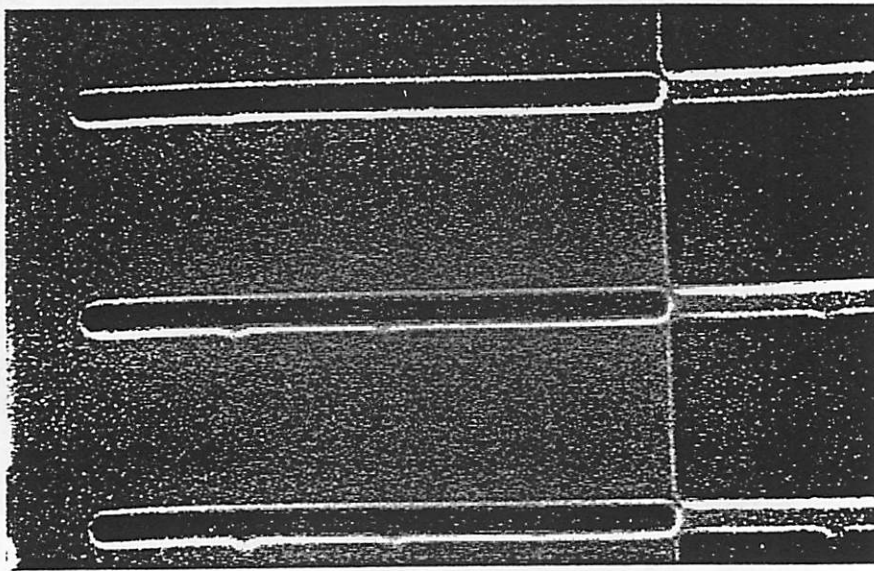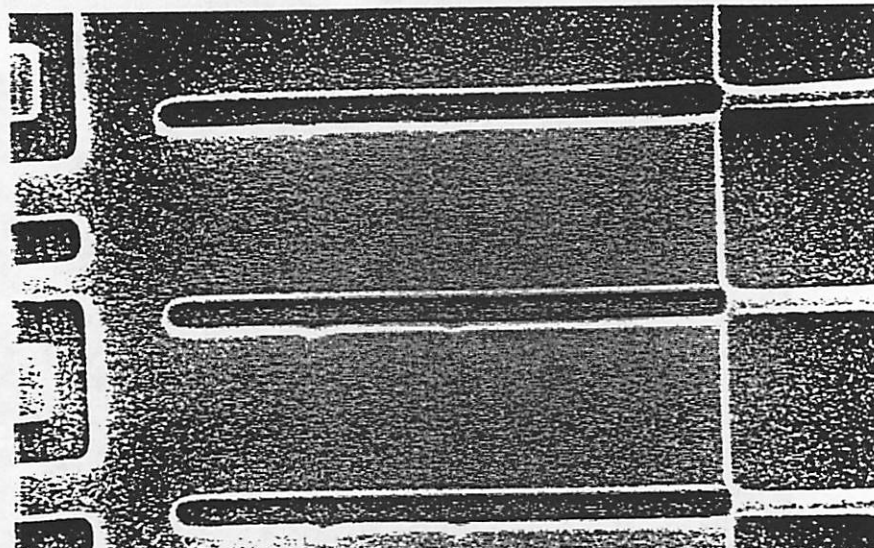
(b) At best focus underexposed

```
10 Microns ▬▬▬▬▬
Accel: 20.96Kv    Mag:    2.41Kx
Width: 27.738 Microns    Test ID: DEFECT  Sample ID: KODAK 820
```

(c) At best dose 3 µm defocus

Fig. 5.4. SEM photographs of the transparent isolated lines with defects of different sizes at different spacings from the lines
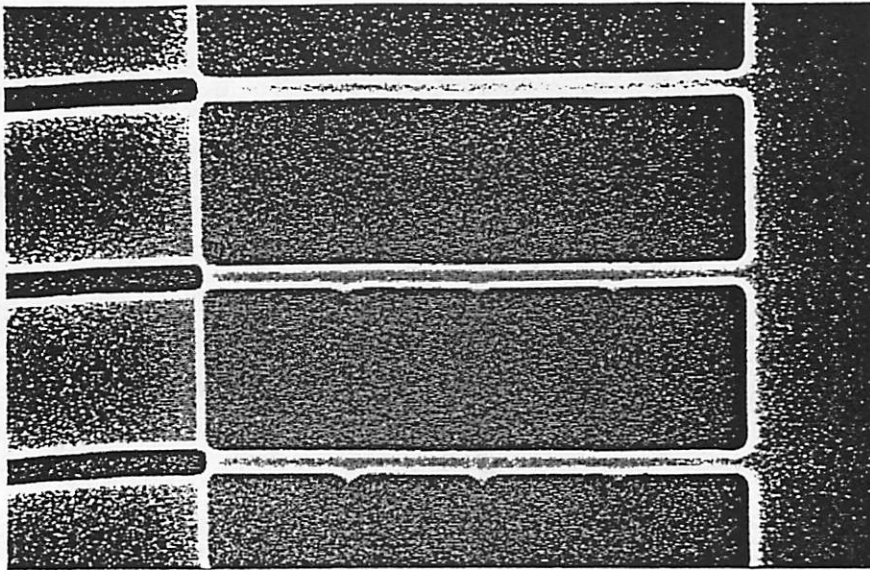
(a) At best focus and dose
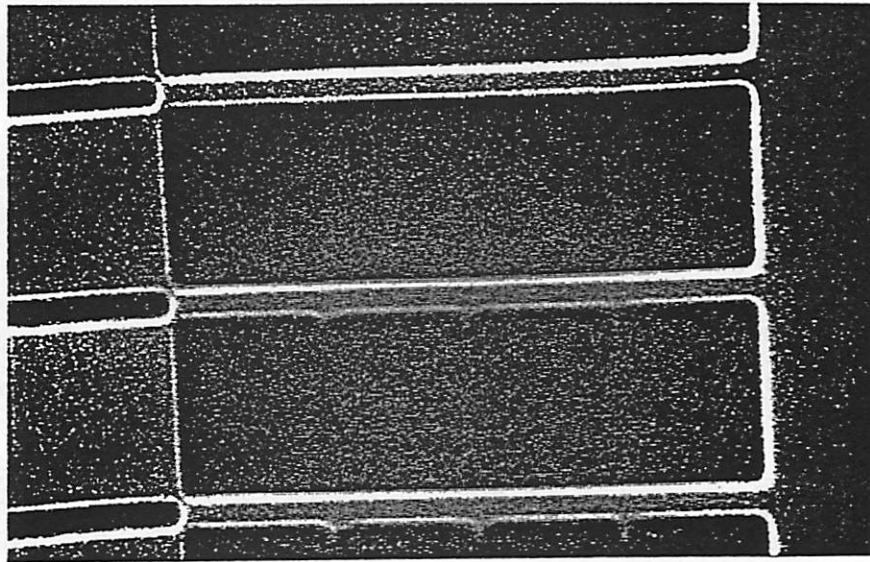
(b) At best focus underexposed
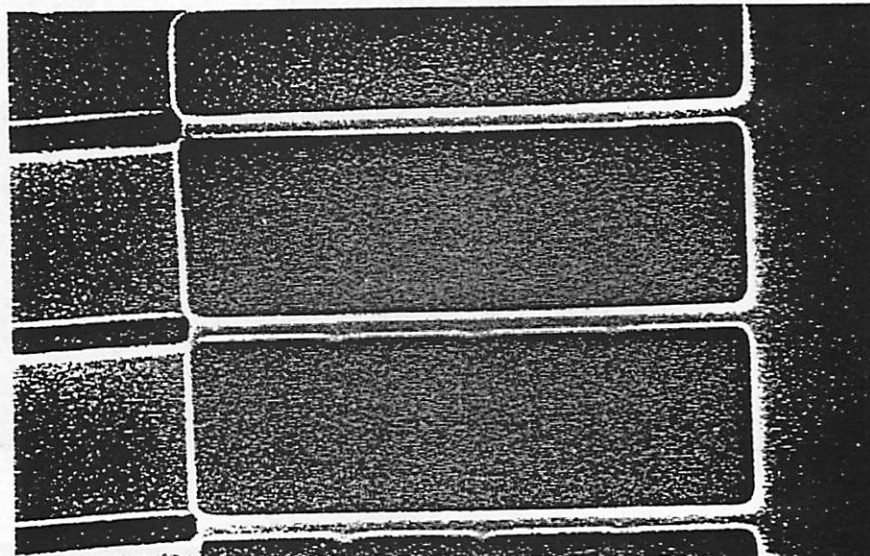
10 Microns
Accel: 20.96Kv   Mag: 2.41Kx
Width: 27.758 Microns   Test ID: DEFECT   Sample ID: KODAK 820

(c) At best dose 3 µm defocus

Fig. 5.5.   SEM photographs of the opaque isolated lines with defects of different sizes at different spacings from the lines

(a) At best focus and dose
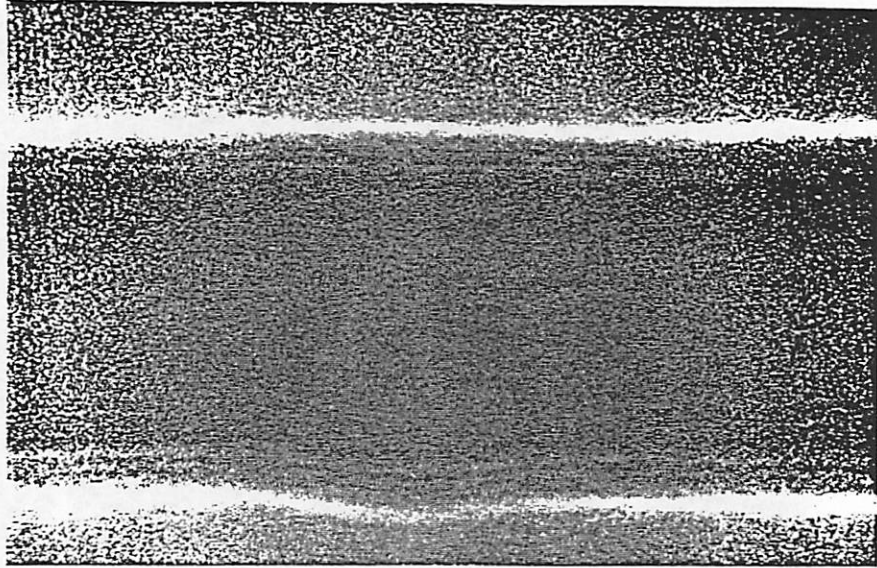
(b) At best focus underexposed
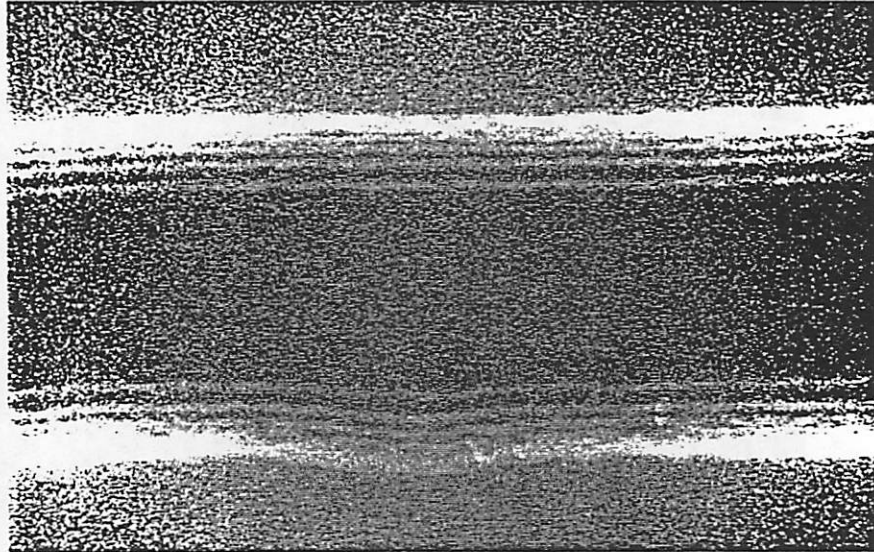
(c) At best dose 3 μm defocus
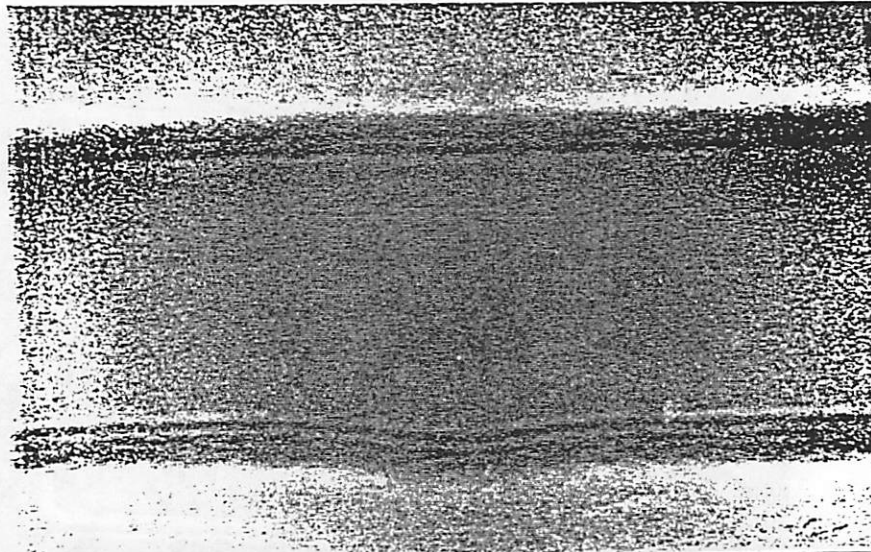
1 Micron
Accel: 19.97Kv   Mag: 28.82Kx
Width: 2.544 Microns   Test ID: LINES   Sample ID: RESIST ON SI

Fig. 5.6.   Enlargement of the 0.3 μm transparent defect at a spacing of 0.2 μm from the line
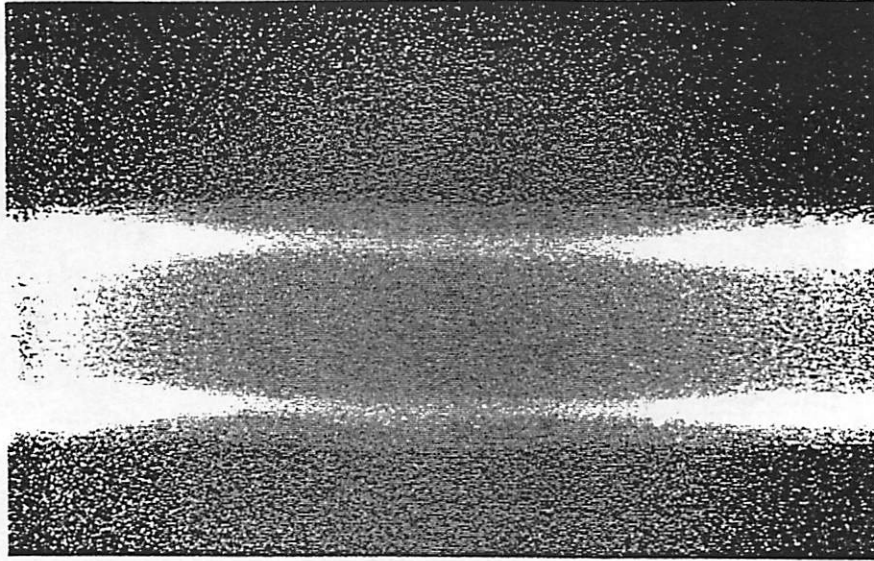
(a) At best focus and dose
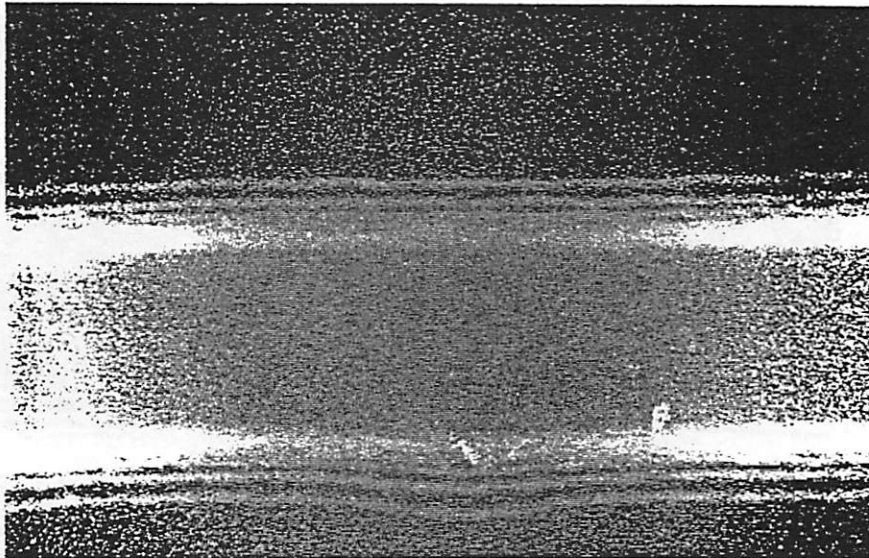
(b) At best focus underexposed

(c) At best dose 3 μm defocus
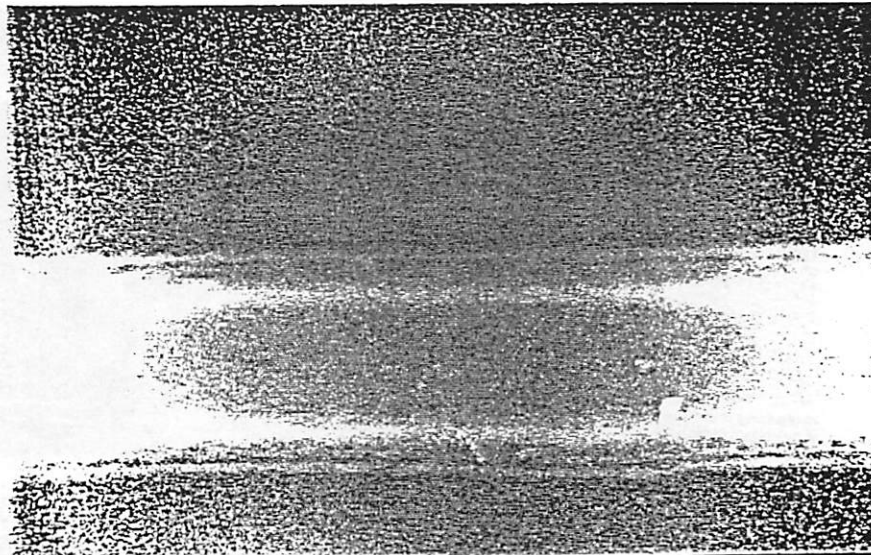
1 Micron

Accel: 19.97Kv   Mag: 28.12Kx
Width: 2.544 Microns   Test ID: LINES   Sample ID: RESIST ON SI

Fig. 5.7.   Enlargement of the 0.3 μm opaque defect at a spacing of 0.2 μm from the line
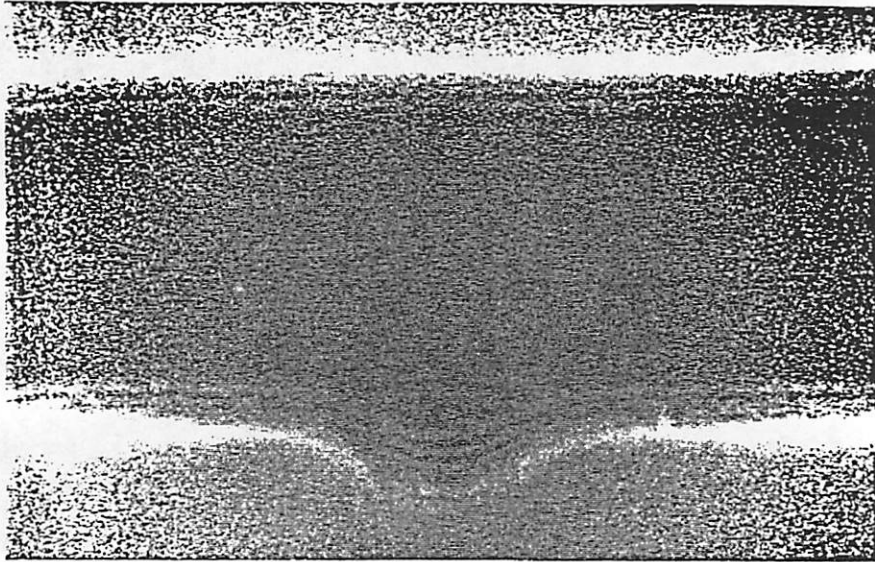
(a) At best focus and dose

(b) At best focus underexposed
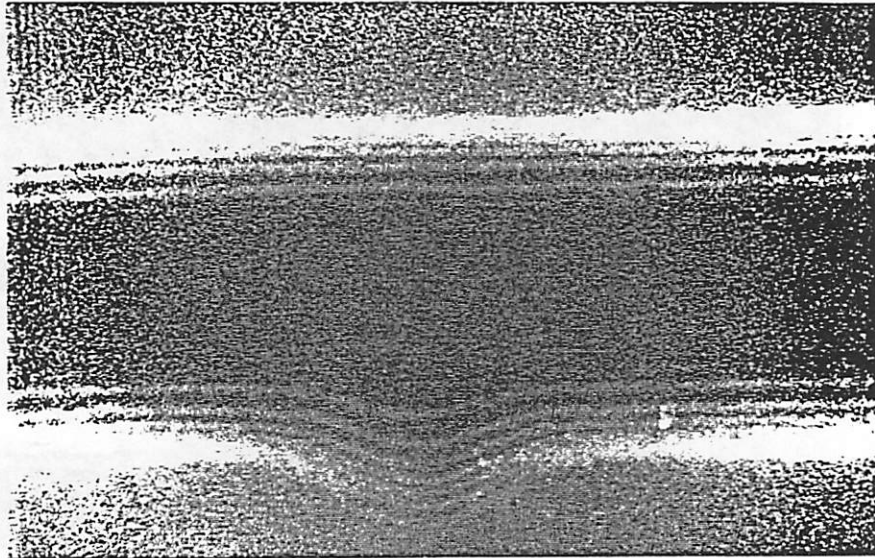
(c) At best dose 3 μm defocus
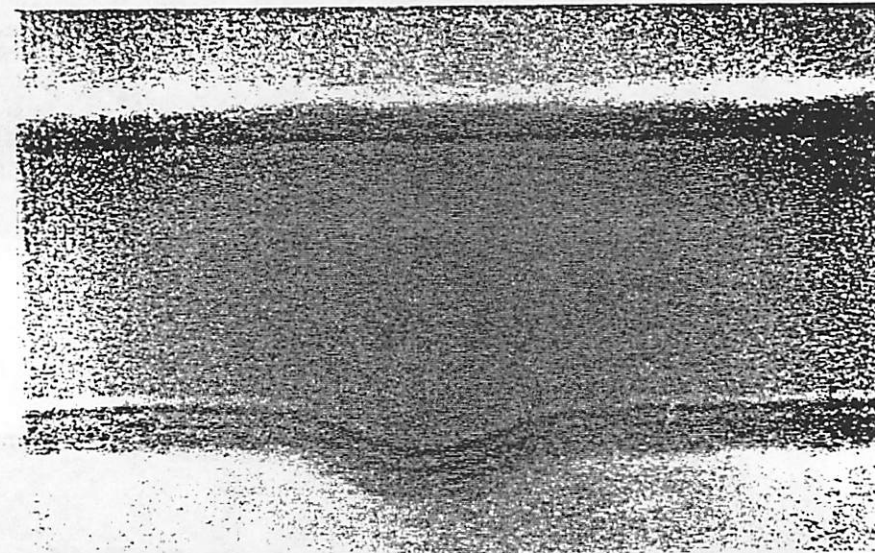
1 Micron
Accel: 19.97Kv Mag: 19.90Kx
Width: 2.544 Microns Test ID: LINES Sample ID: RESIST ON SI

Fig. 5.8. Enlargement of the 0.6 μm transparent defect at a spacing of 0.2 μm from the line

(a) At best focus and dose
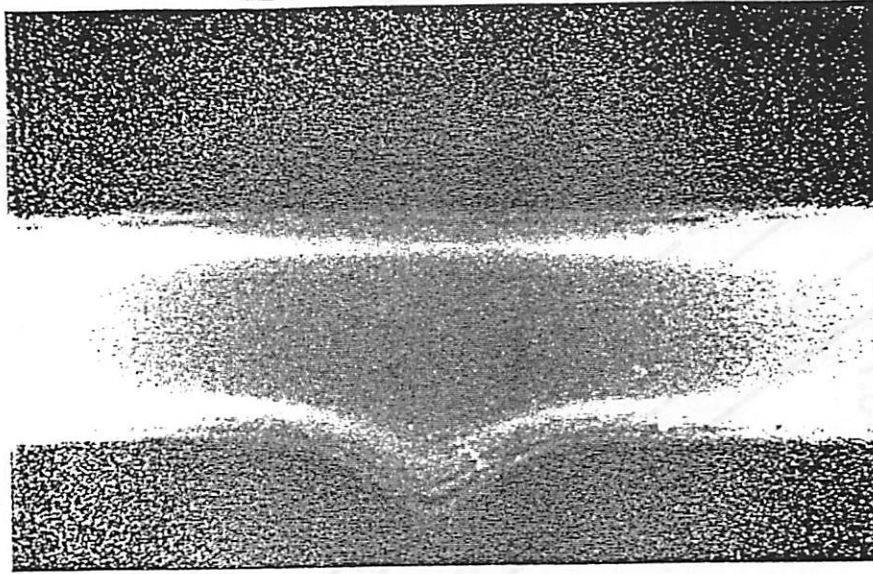
(b) At best focus underexposed
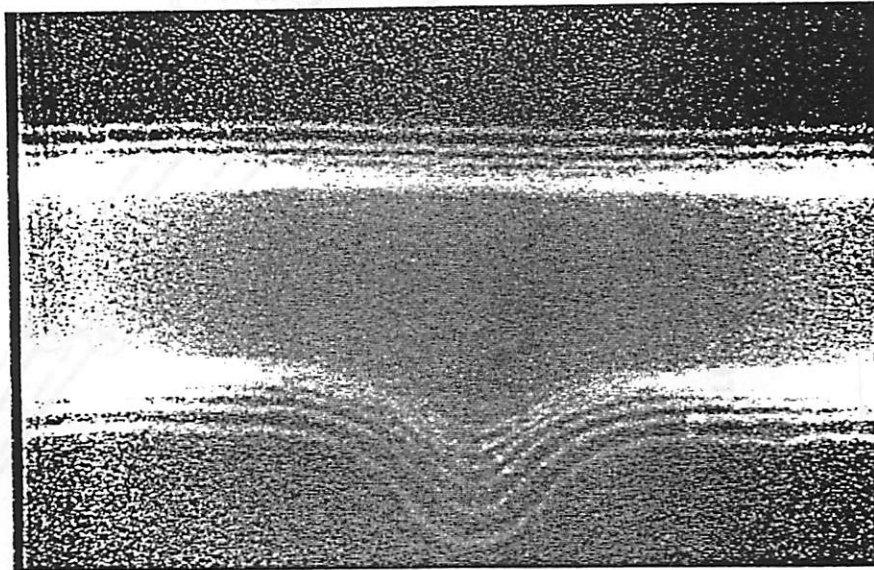
(c) At best dose 3 µm defocus
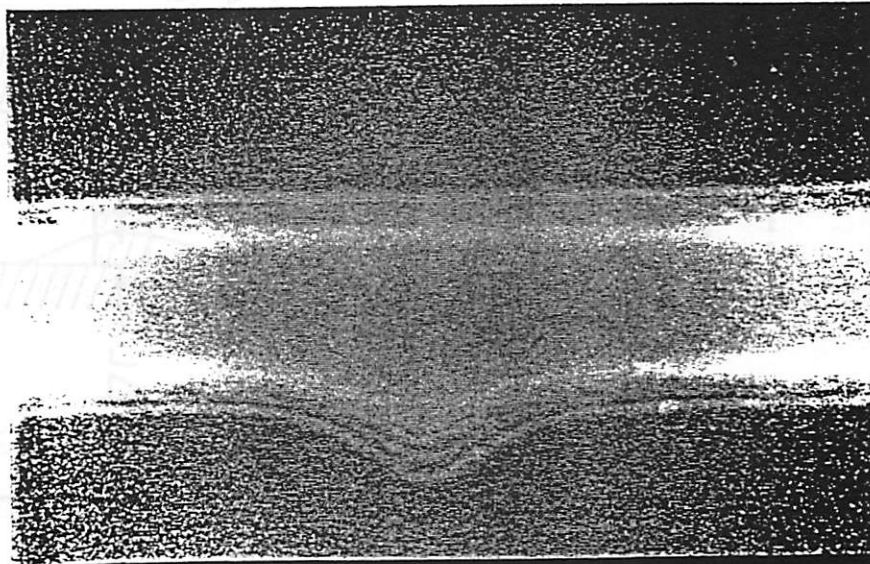
1 Micron
Accel: 19.97Kv   Mag: 19.95Kx
Width: 2.544 Microns   Test ID: LINES   Sample ID: RESIST ON SI

Fig. 5.9.   Enlargement of the 0.6 µm opaque defect at a spacing of 0.2 µm from the line

Fig. 5.10. Line width variation as a function of defect size
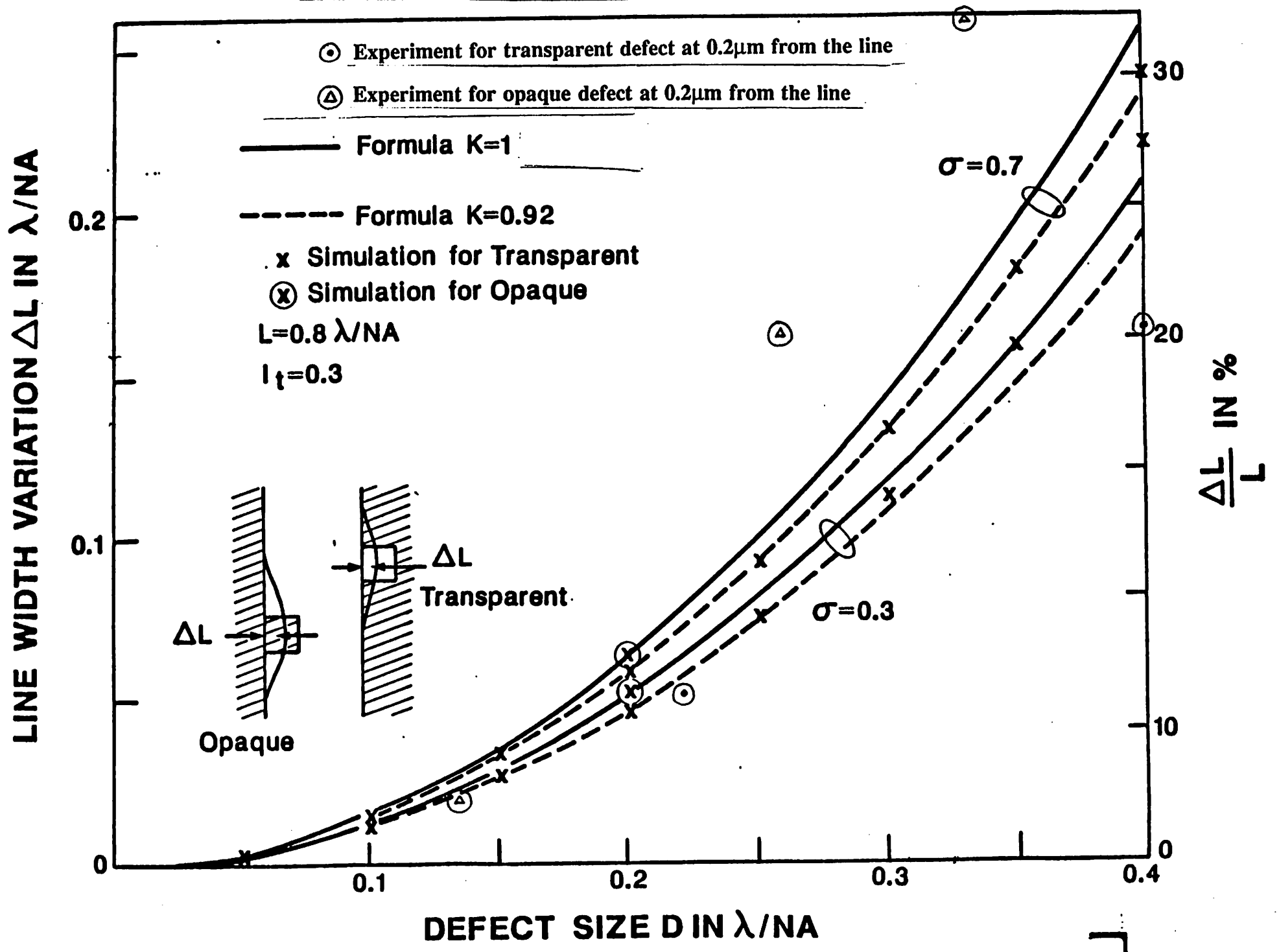
Image Intensity Contour Plot
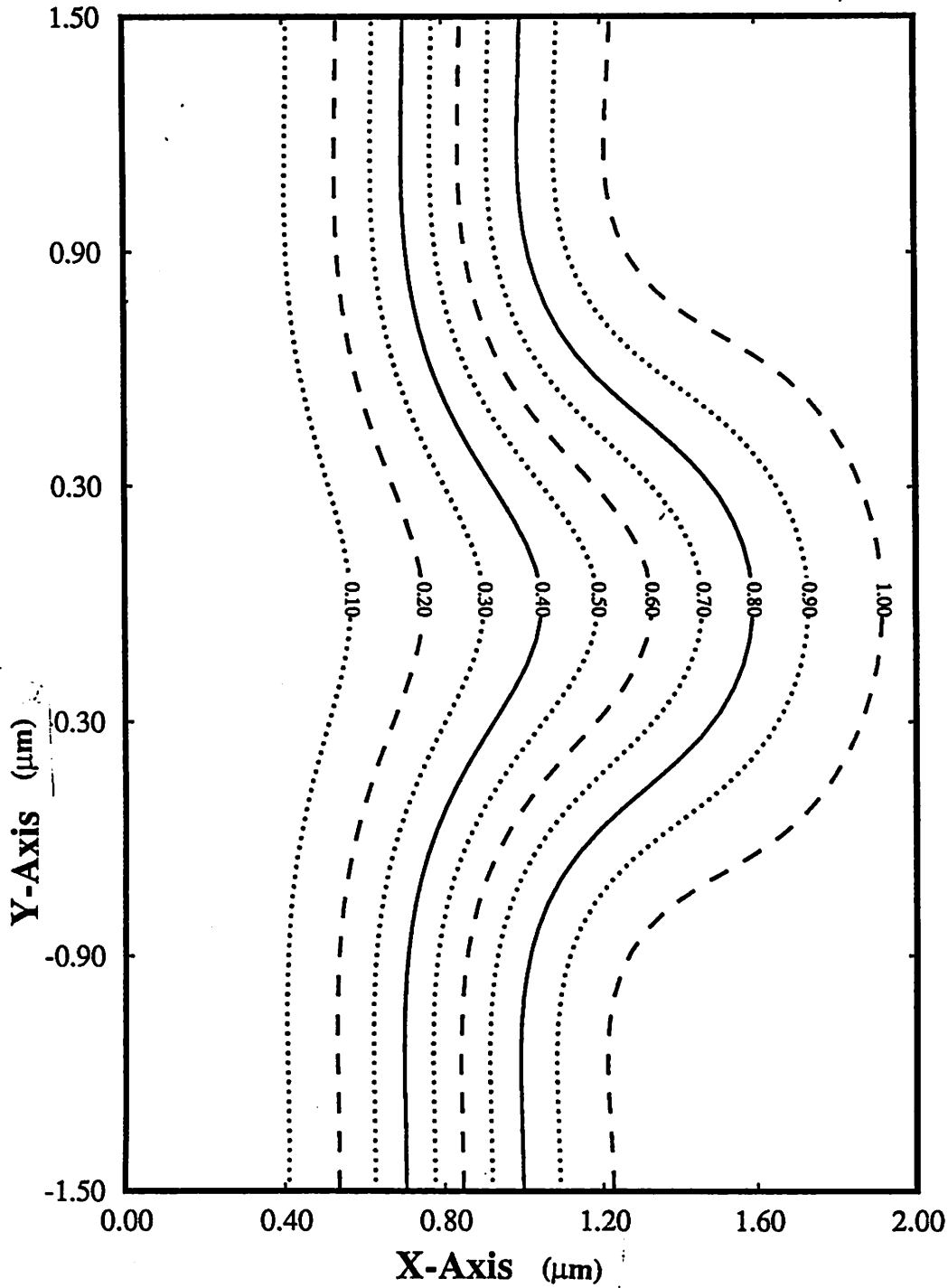
Fig. 5.11. Simulation of a 0.6µm opaque defect at 0.2µm from a line (corrected for bias)

Image Intensity Contour Plot
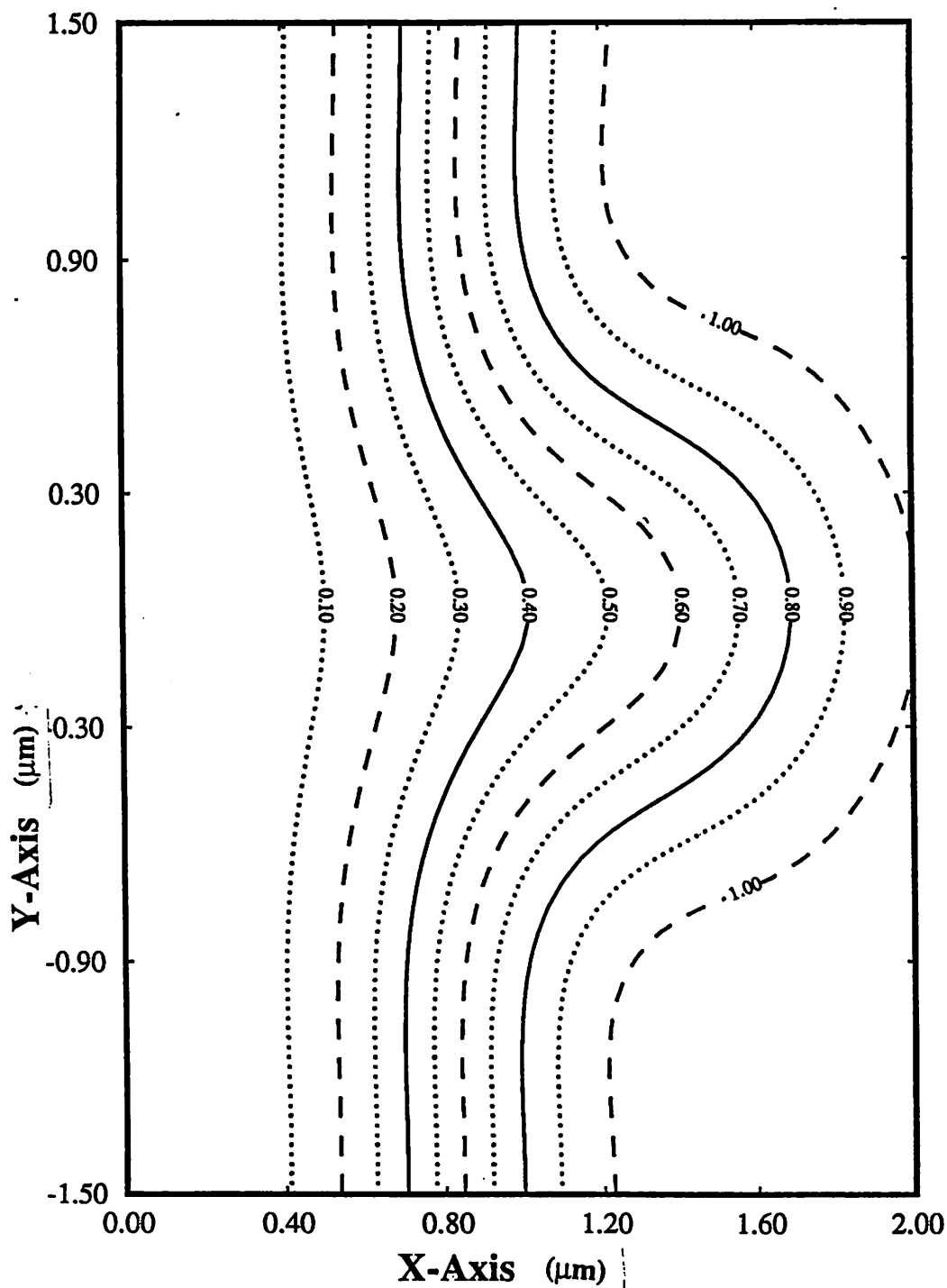
Fig. 5.12. Simulation of a 0.6μm opaque defect at 0.3μm from a line (corrected for bias)

Image Intensity Contour Plot
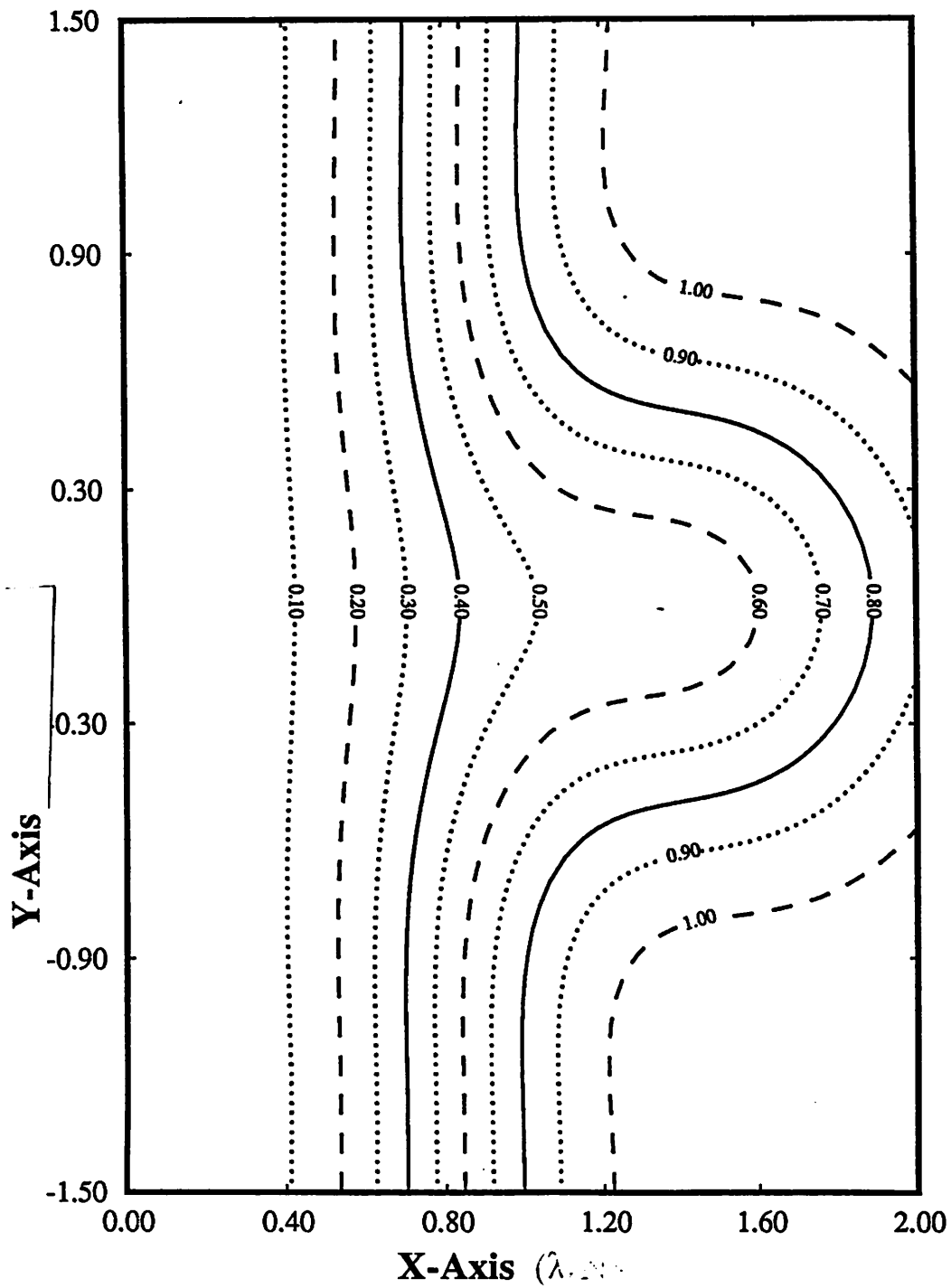
Fig. 5.13. Simulation of a 0.6μm opaque defect at 0.5μm from a line (corrected for bias)

Image Intensity Contour Plot
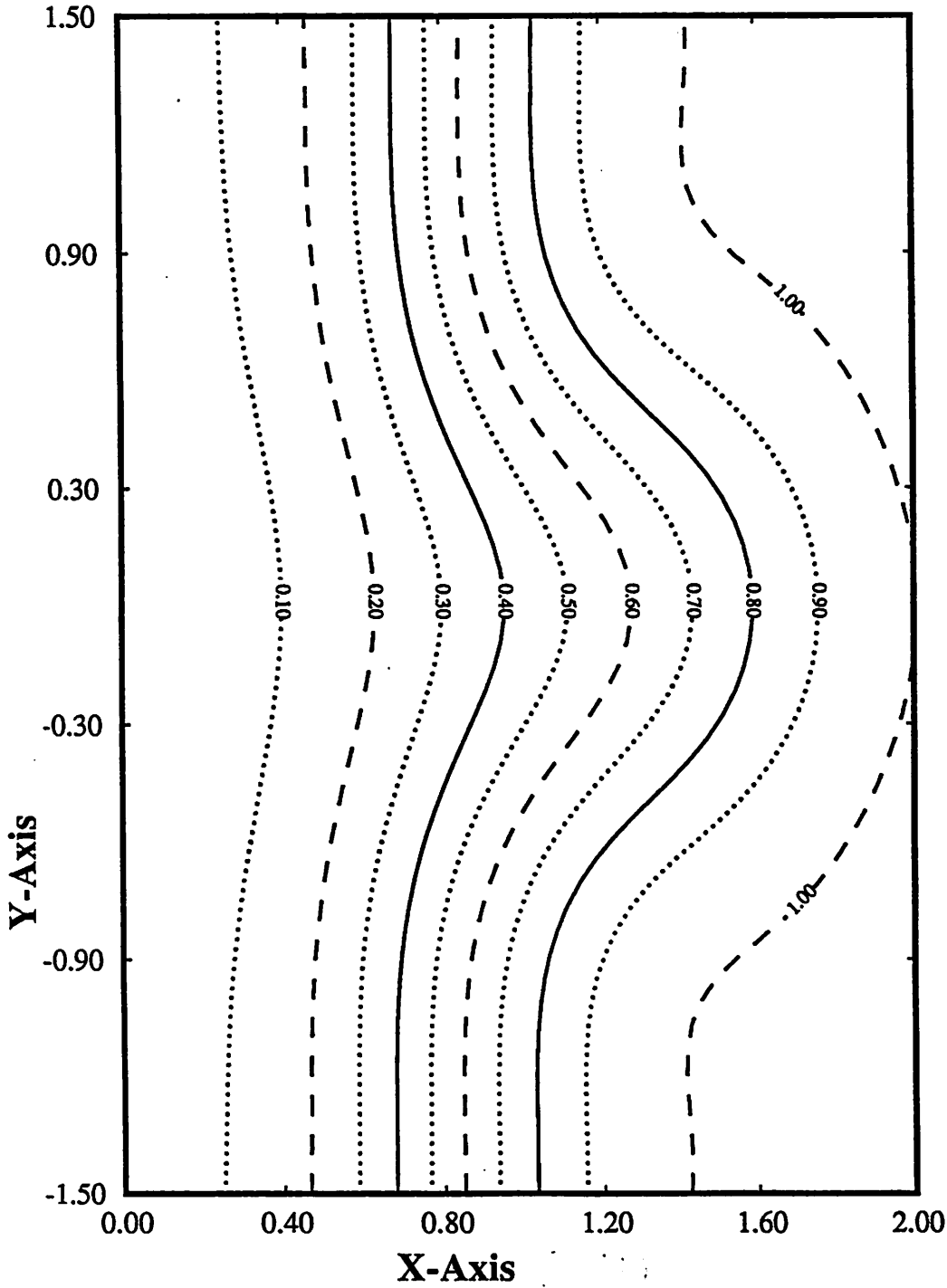
Fig. 5.14. Simulation of a 0.6μm opaque defect at 0.2μm from a line (3μm defocus,corrected for bias)

Image Intensity Contour Plot

Y-Axis (μm) / **X-Axis (μm)**

0.90, 0.80, 0.70, 0.60, 0.50, 0.40, 0.30, 0.20, 0.10

3 μm defocus

Y-Axis (μm) / **X-Axis (μm)**

0.80, 0.70, 0.60, 0.50, 0.40, 0.30, 0.20, 0.10
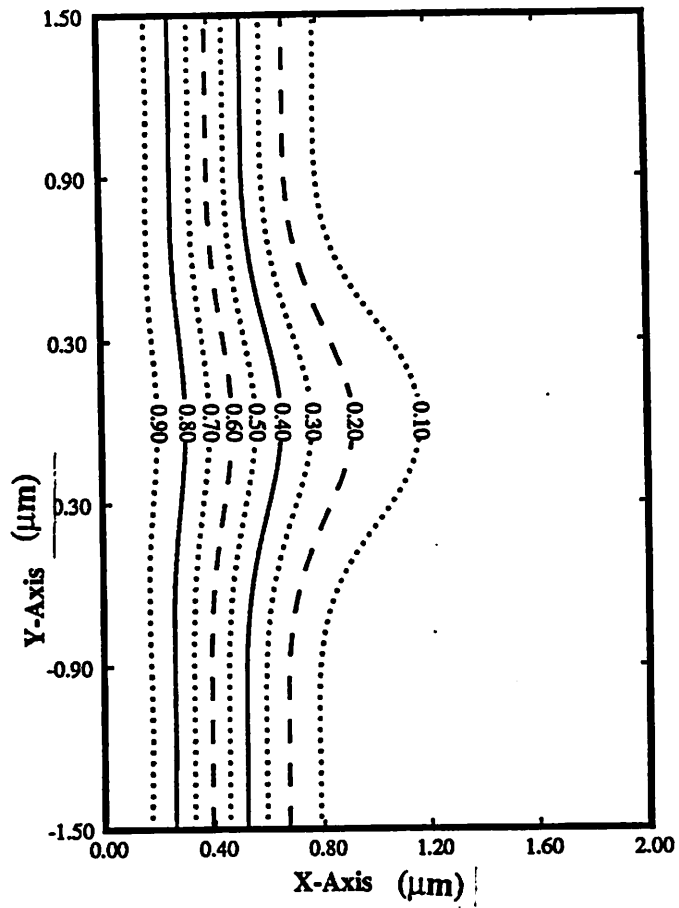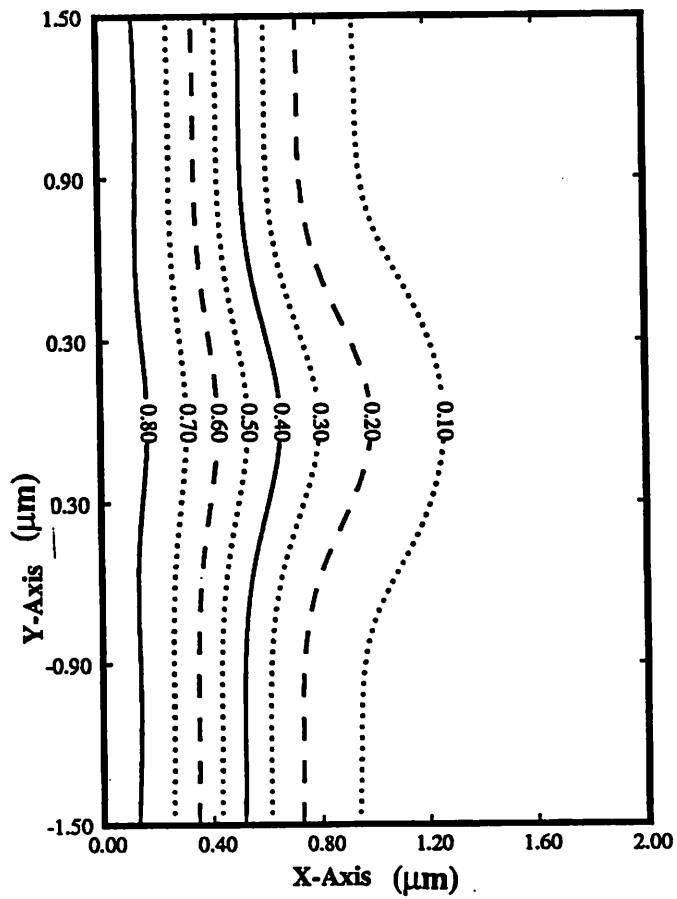
Fig. 5.15. Simulation of a 0.6μm transparent defect at 0.2μm from a line (corrected for bias)

(a) Transparent

10 Microns
Accel: 19.92Kv   Mag: 2.62Kx
Width: 17.872 Microns   Test ID: HUYNH   Sample ID: PR DEFECTS

(b) Opaque

10 Microns
Accel: 19.92Kv   Mag: 2.52Kx
Width: 17.872 Microns   Test ID: HUYNH   Sample ID: PR DEFECTS
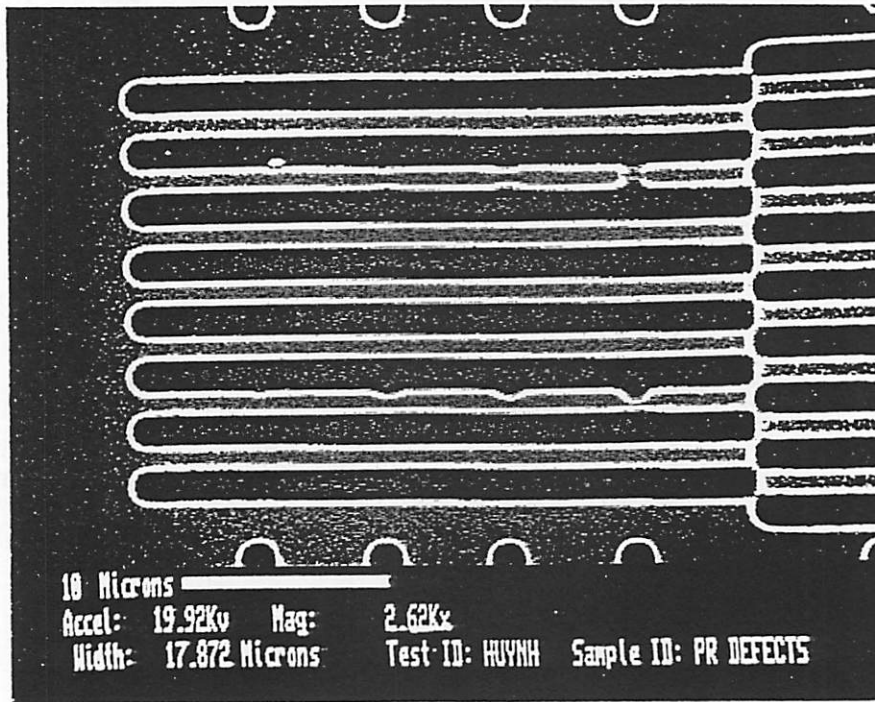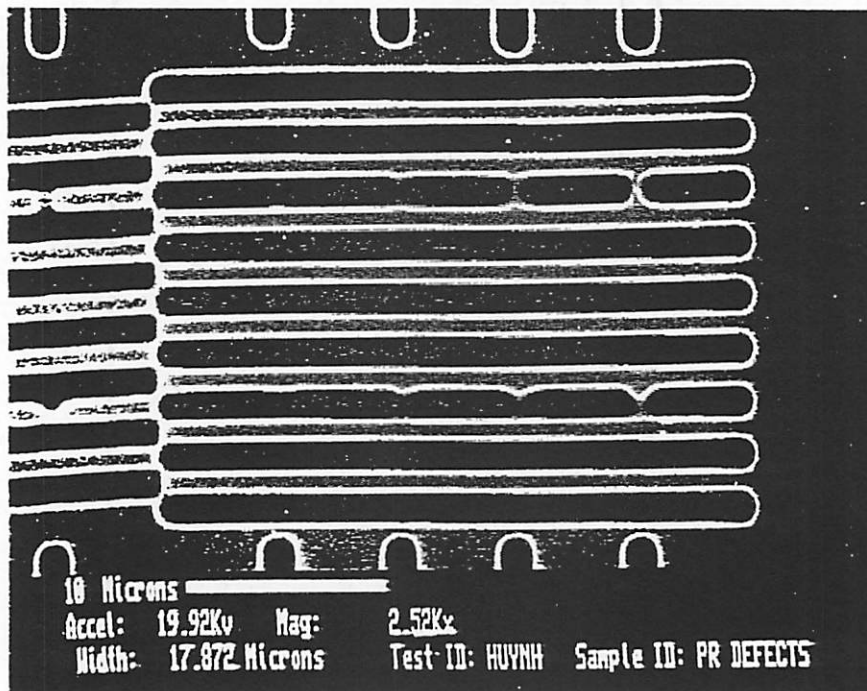
Fig. 5.16. SEM photographs of the line arrays with centered and edged defects

(a) At best focus and dose

(b) At best focus underexposed

1. Micron
Accel: 20.96Kv Mag: 13.73Kx
Width: 27.758 Microns   Test-ID: DEFECT Sample ID: KODAK 820
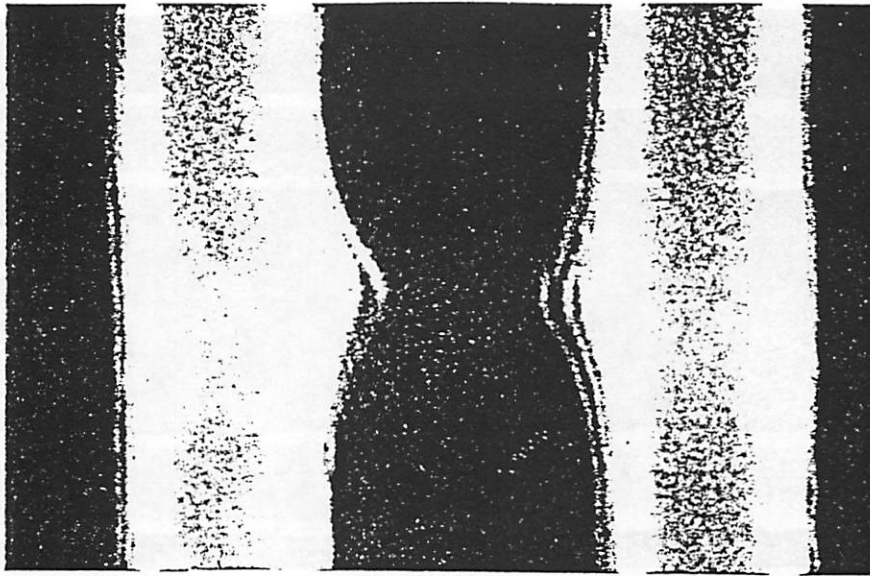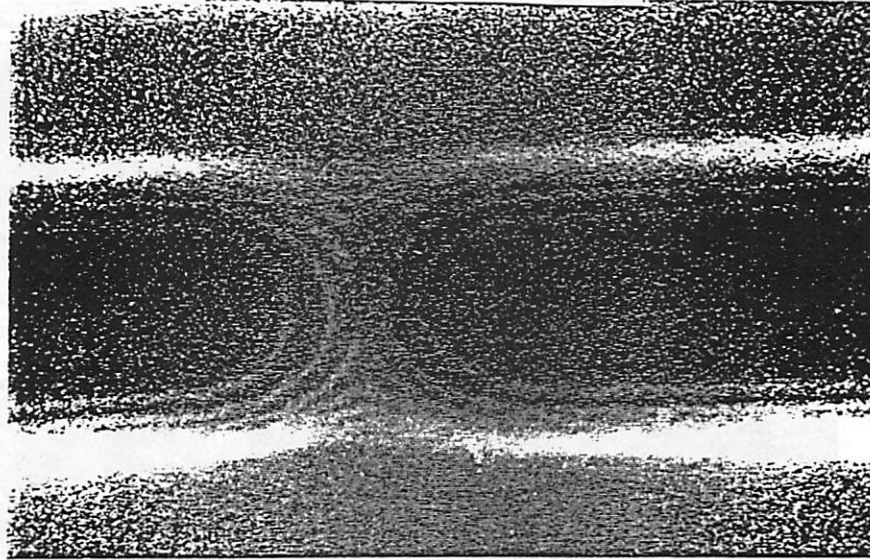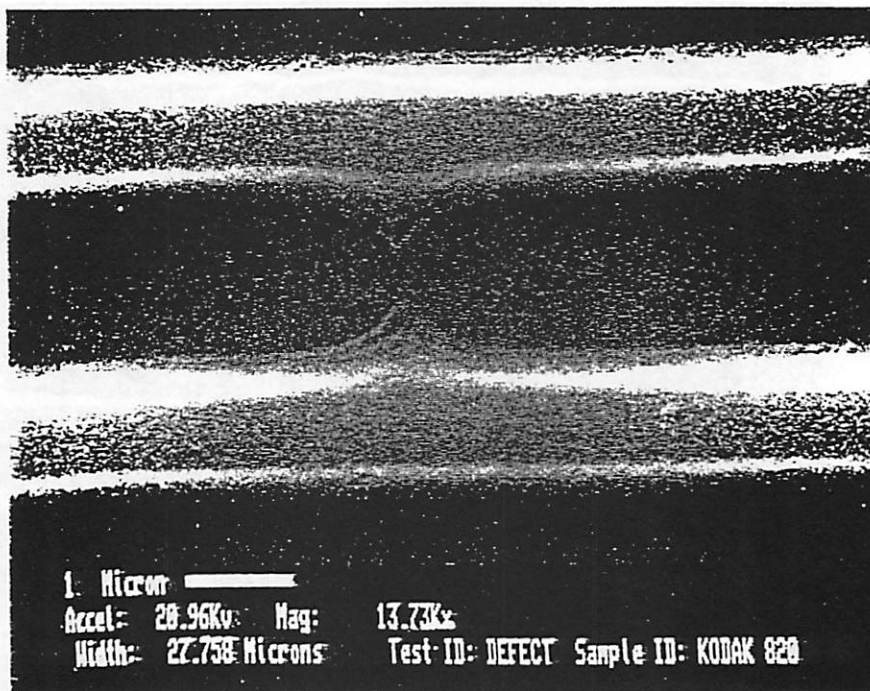
(c) At best dose 3 μm defocus

Fig. 5.17. Enlargement of the 0.5 μm opaque centered defect printed on Si substrate

(a) At best focus and dose

(b) At best focus underexposed

1 Micron
Accel: 19.91Kv   Mag: 15.68Kx
Width: 3.077 Microns   Test ID: JJ4   Sample ID: AFTER NH ETCH
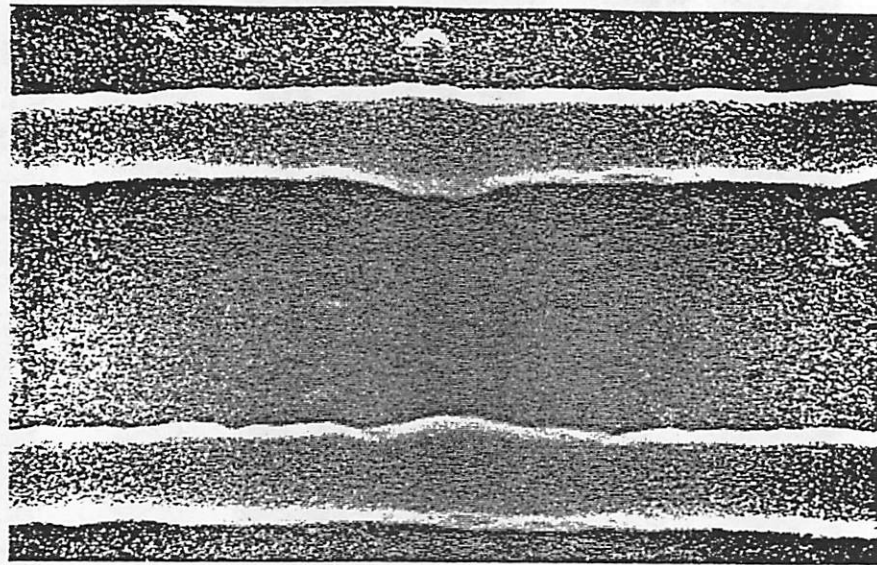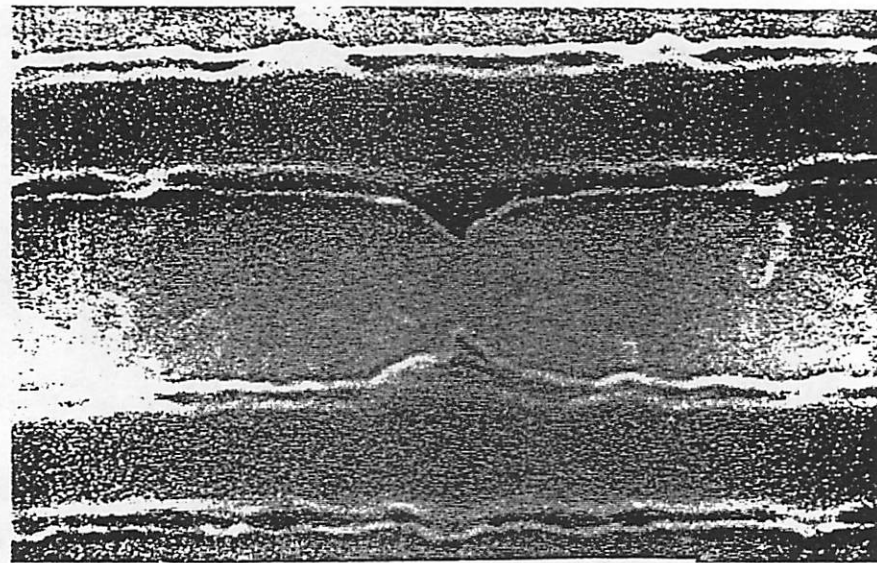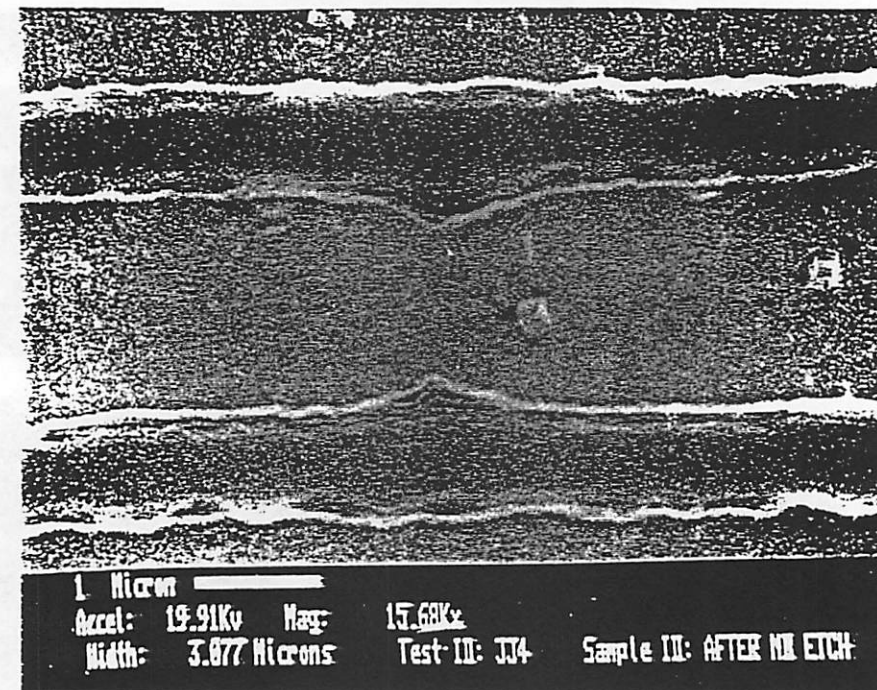
(c) At best dose 3 μm defocus

Fig. 5.18. Enlargement of the 0.5 μm opaque centered defect printed on Al substrate
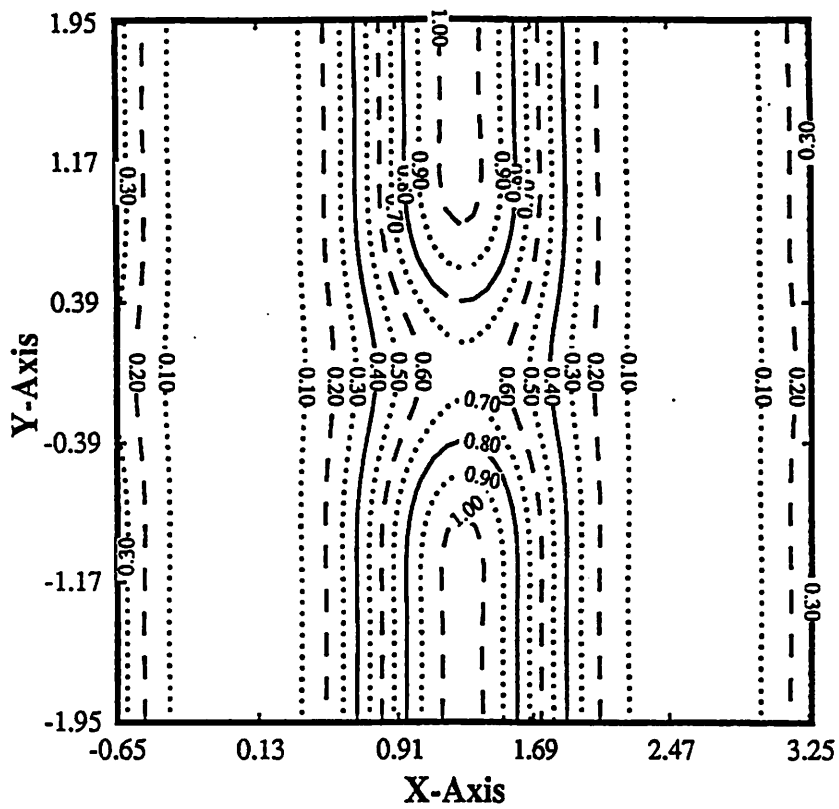
3 μm defocus
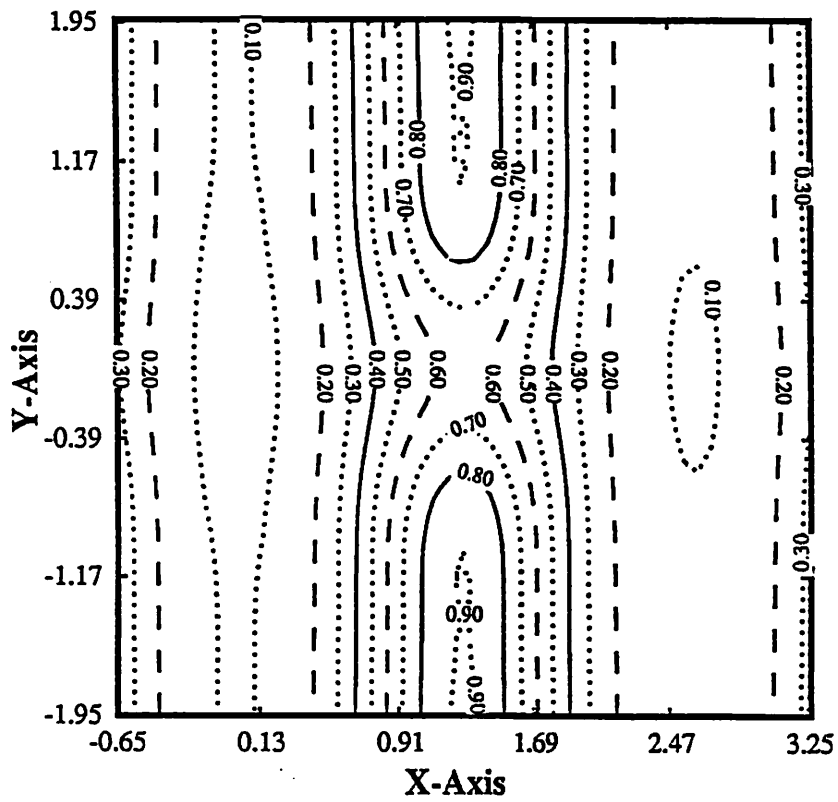
Fig. 5.19. Simulations of the 0.5 μm opaque centered defect

(a) At best focus and dose

(b) At best focus underexposed

1 Micron
Accel: 28.96Kv   Mag: 28.64Kx
Width: 27.758 Microns   Test ID: DEFECT Sample ID: KODAK 828
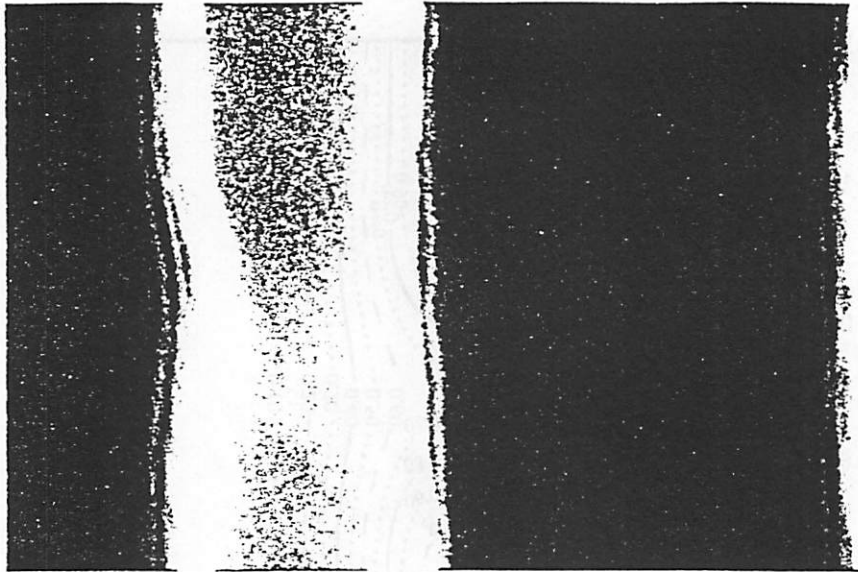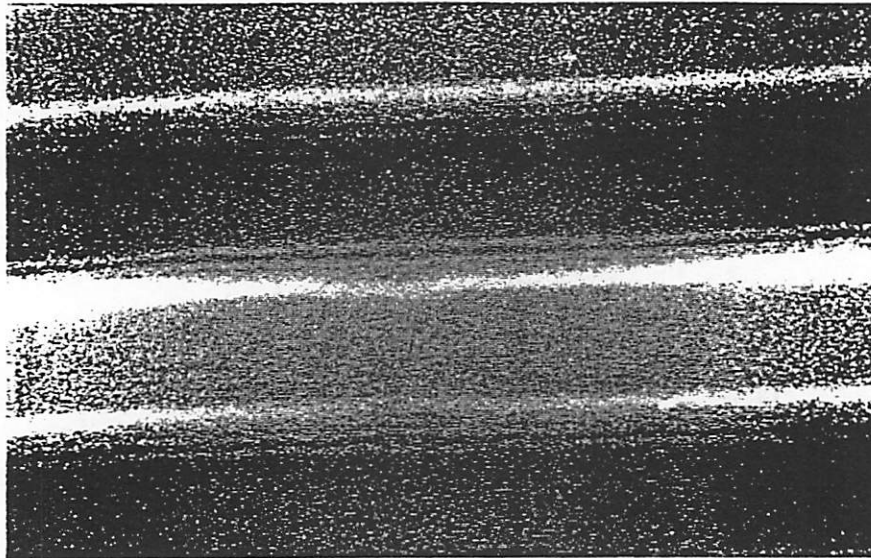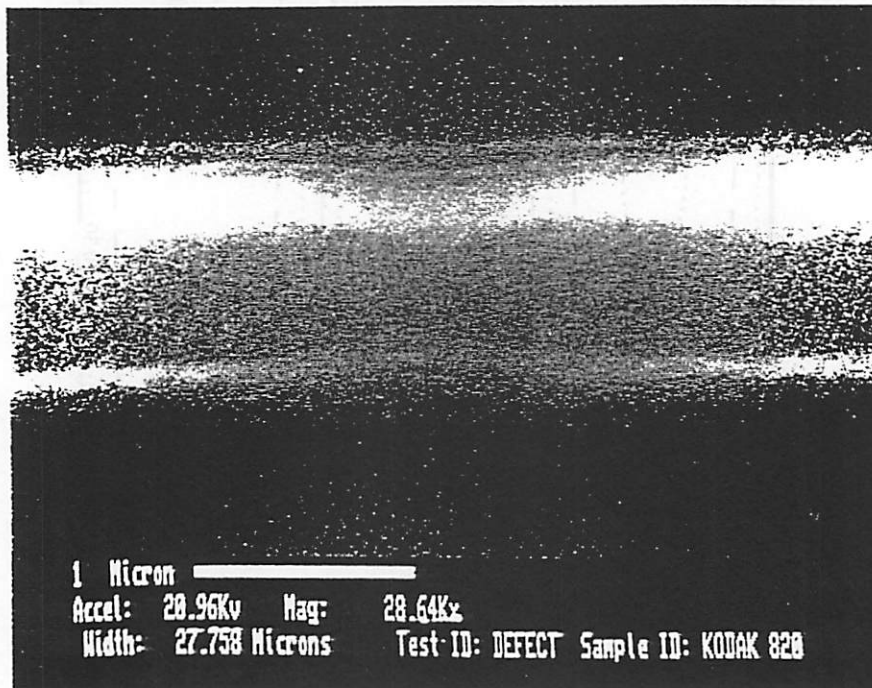
(c) At best dose 3 μm defocus

Fig. 5.20. Enlargement of the 0.5 μm transparent centered defect printed on Si substrate

(a) At best focus and dose

(b) At best focus underexposed

10 Microns
Accel: 20.90Kv   Mag: 5.65Kx
Width: 27.758 Microns   Test ID: DEFECT Sample ID: KODAK 820
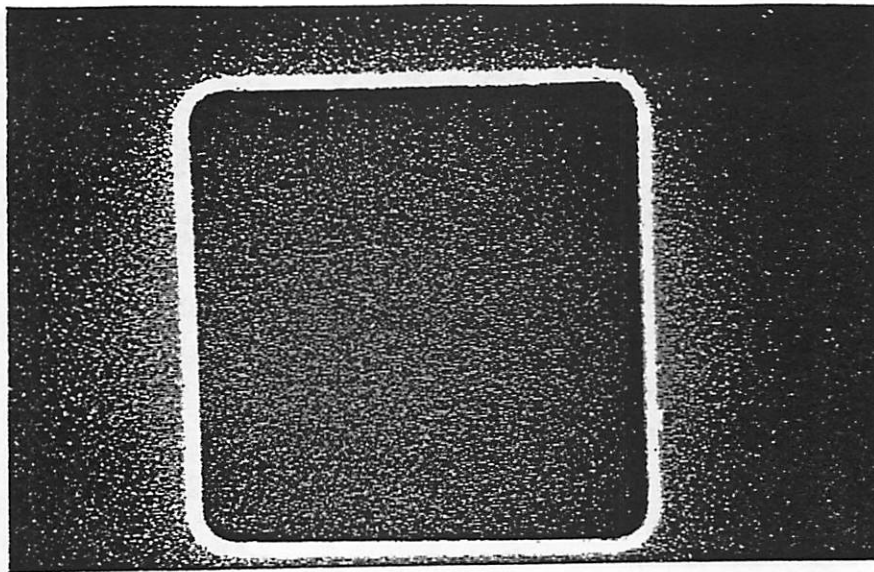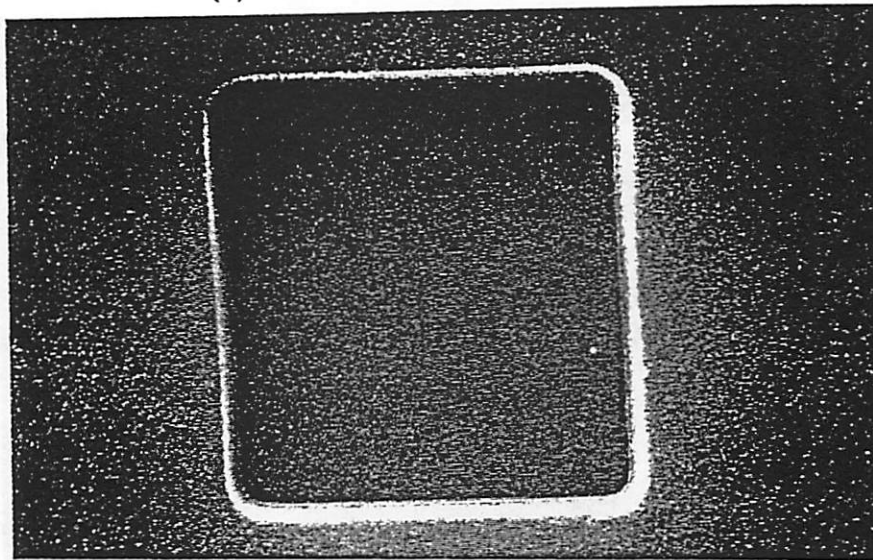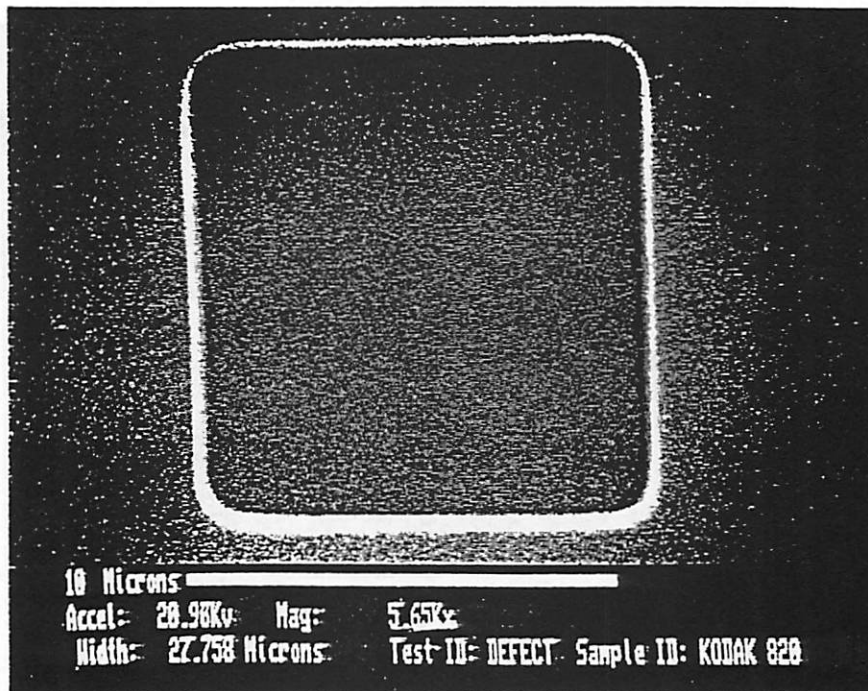
(c) At best dose 3 µm defocus

Fig. 5.21. 10 x 10 µm transparent square with defects located diagonally from the corners

(a) At best focus and dose

(b) At best focus underexposed

10 Microns
Accel: 28.96Kv Mag: 5.37Kv
Width: 27.758 Microns Test ID: DEFECT Sample ID: KODAK 828
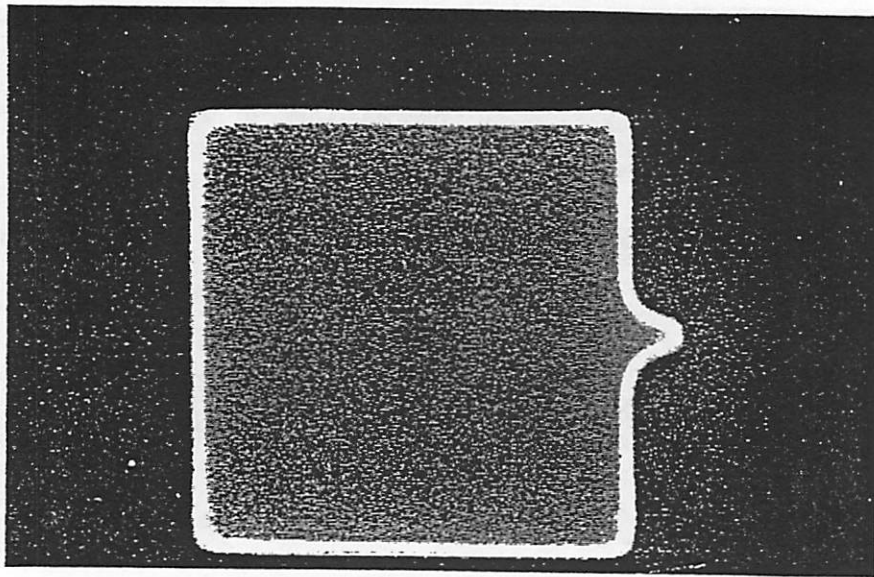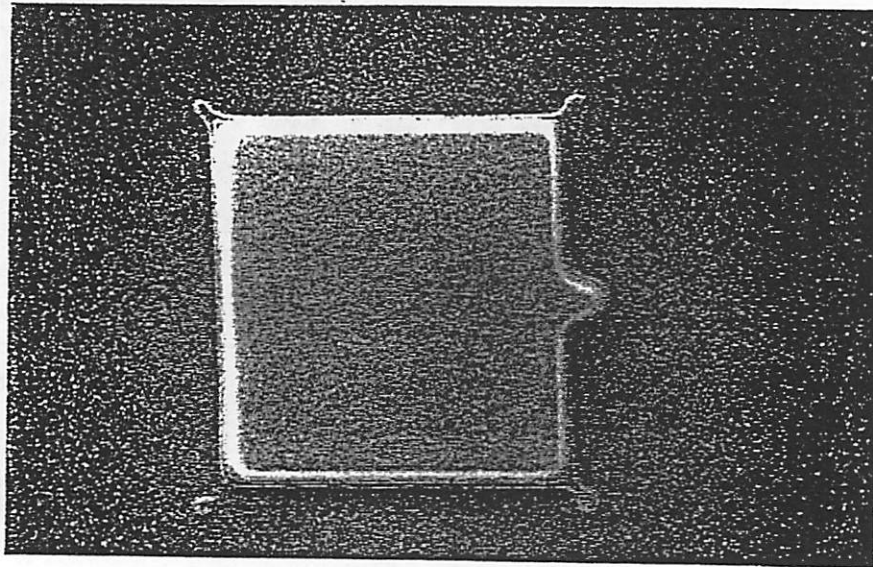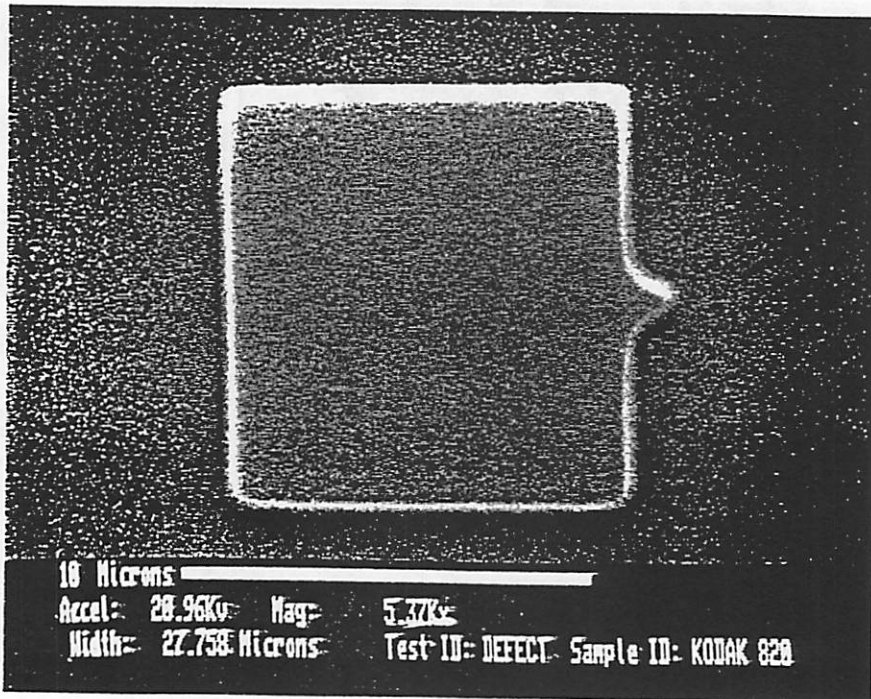
(c) At best dose 3 μm defocus

Fig. 5.22. 10 x 10 μm opaque square with defects located diagonally from the corners

Image Intensity Contour Plot
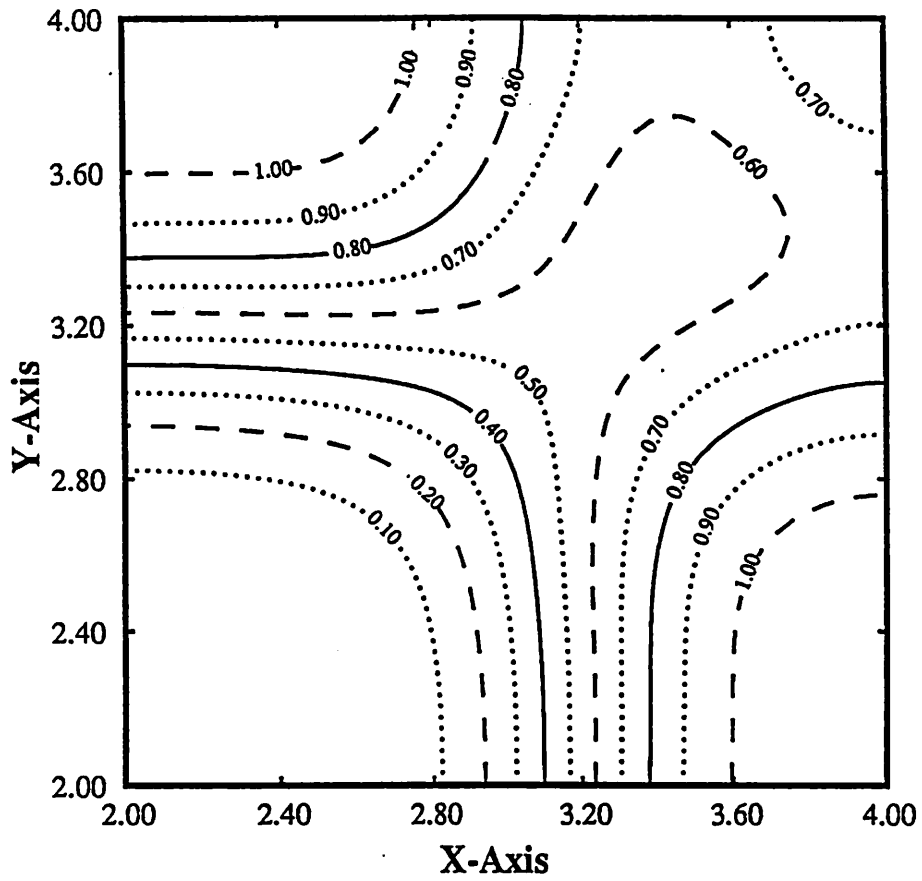
3 μm defocus
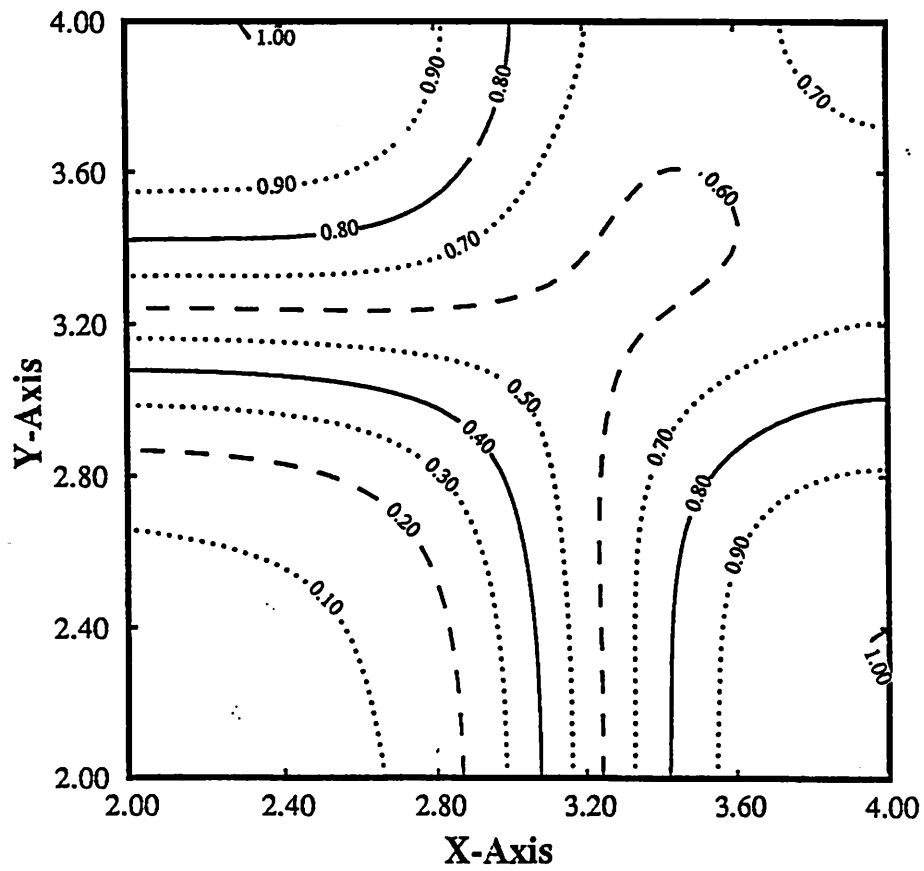
Fig. 5.23. SPLAT simulations of an opaque defect at 0.2 μm from the corner
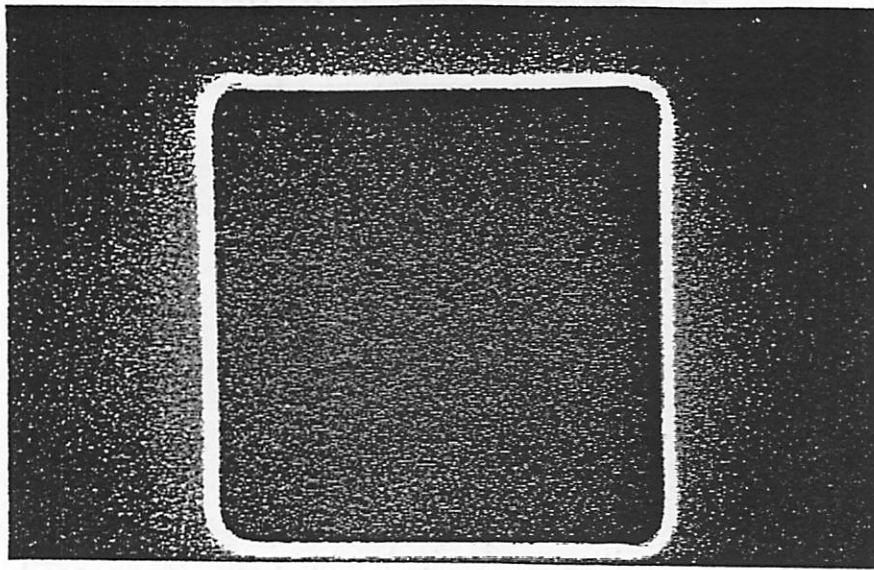
(a) At best focus and dose
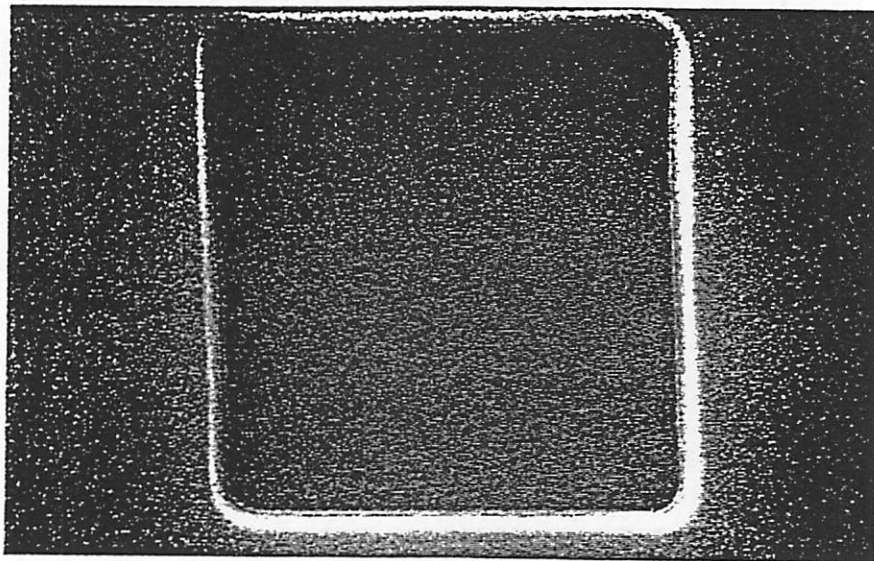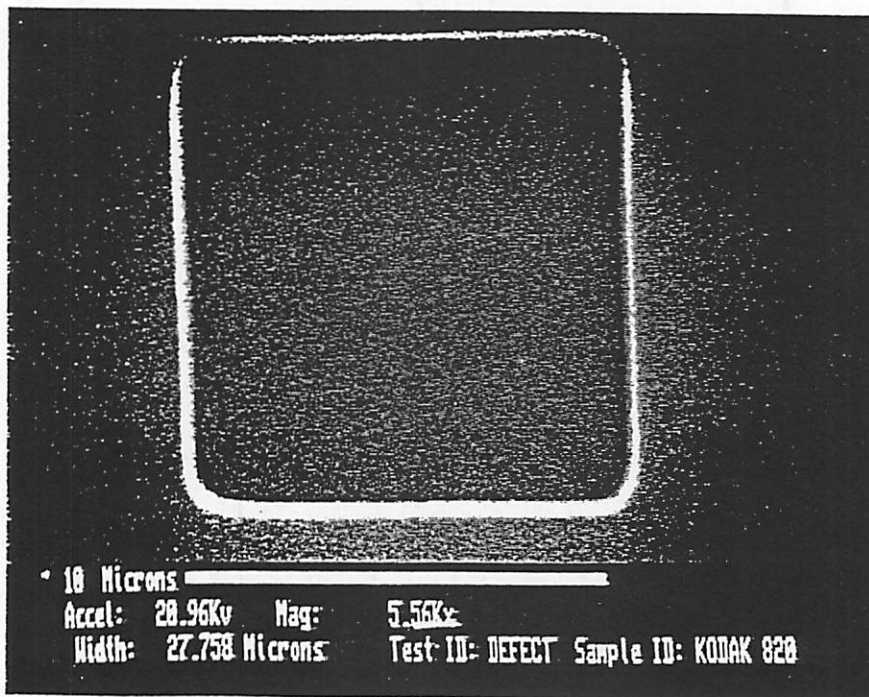
(b) At best focus underexposed

10 Microns
Accel: 20.96Kv   Mag: 5.56Kx
Width: 27.758 Microns   Test ID: DEFECT Sample ID: KODAK 820

(c) At best dose 3 μm defocus

Fig. 5.24. 10 x 10 μm transparent square with defects collinear with the edges

(a) At best focus and dose

(b) At best focus underexposed

10 Microns
Accel: 20.90Kv Mag: 5.17Kv
Width: 27.758 Microns   Test ID: DEFECT Sample ID: KODAK 820
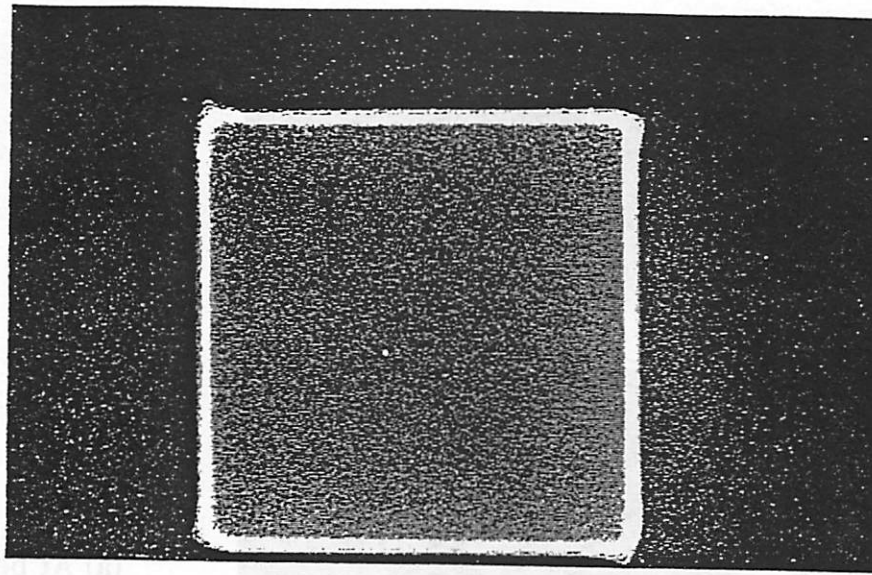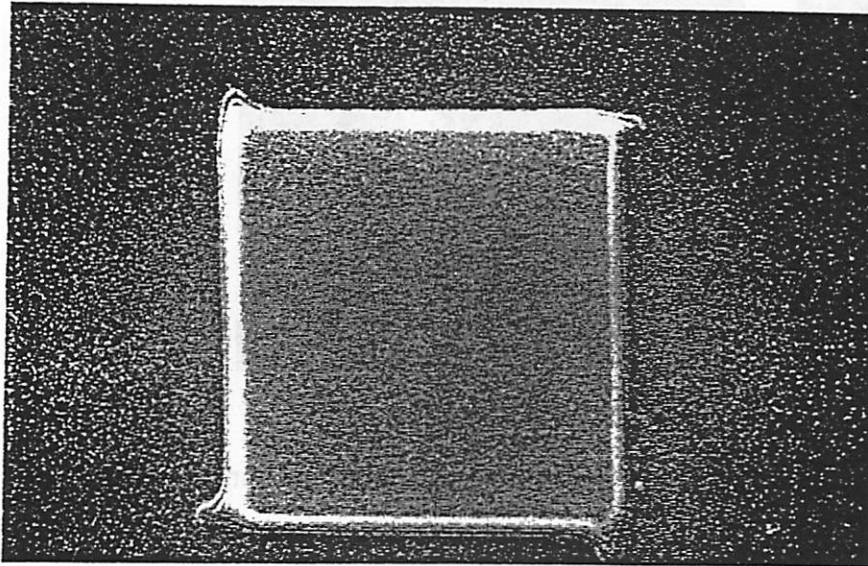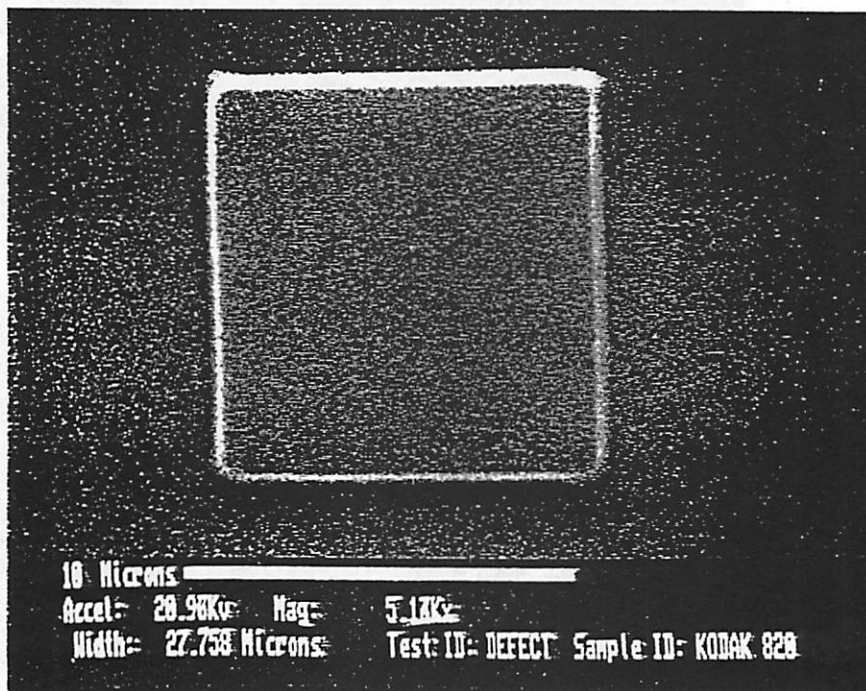
(c) At best dose 3 μm defocus

Fig. 5.25. 10 x 10 μm opaque square with defects collinear with the edges
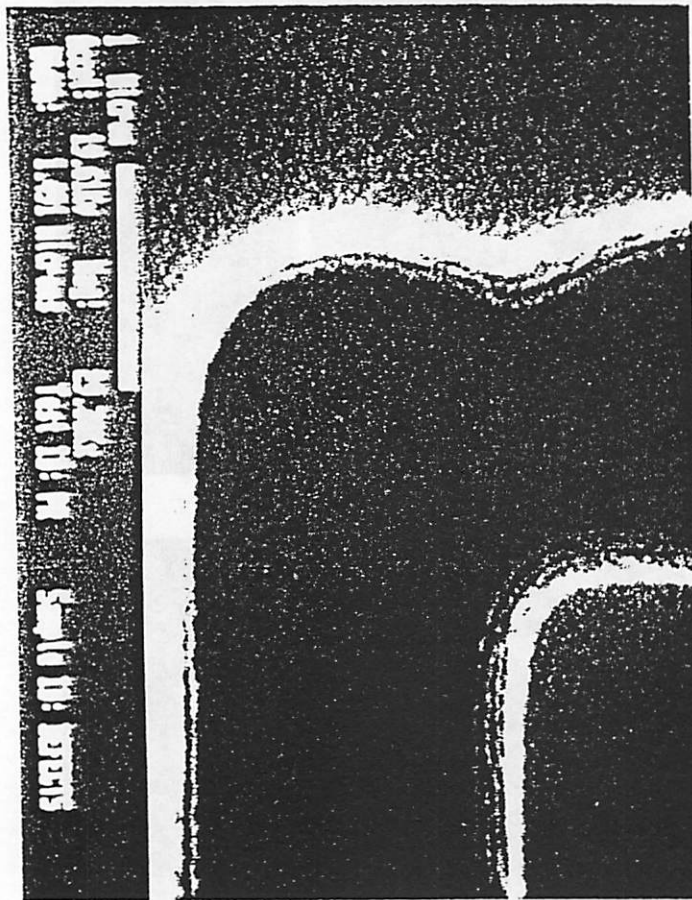
(a) At best focus and dose

Fig. 5.26. SEM photographs of a transparent elbow with a 0.5 x 0.5 μm defect collinear with the vertical inner edge and horizontal outer edge of the elbow
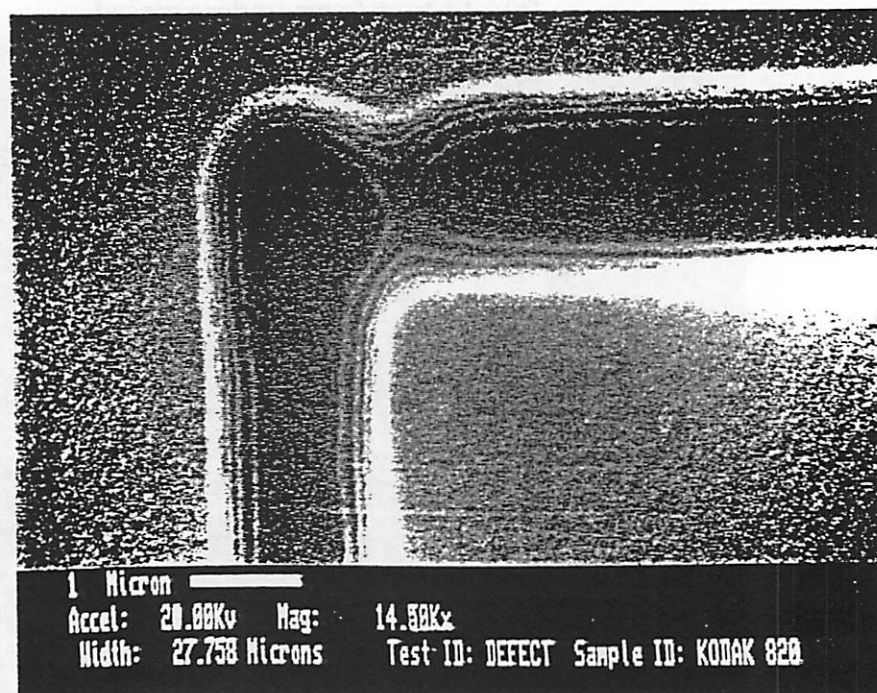
(b) At best focus underexposed
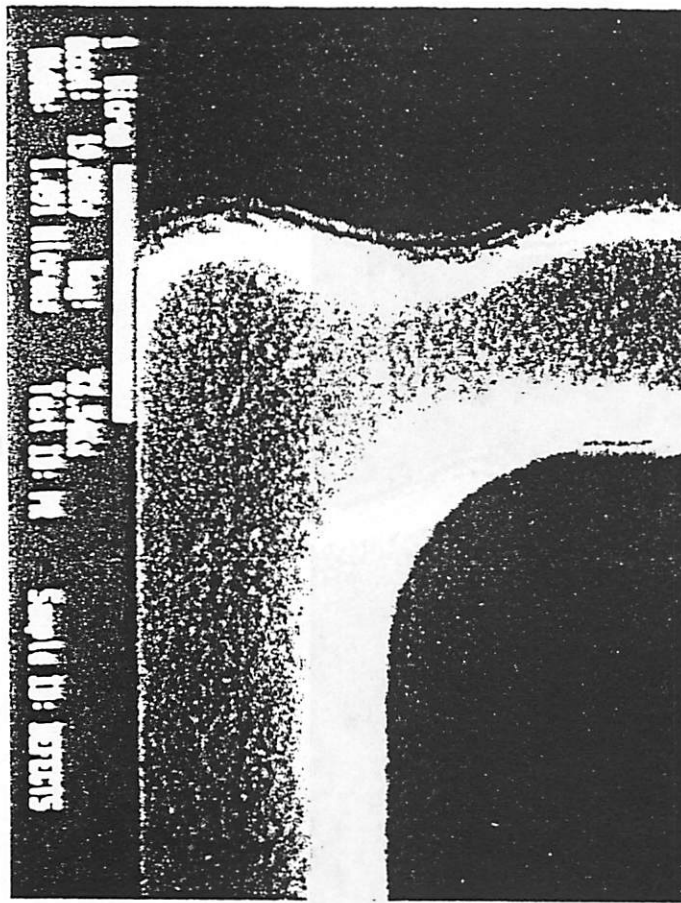
(a) At best focus and dose

Fig. 5.27. SEM photographs of an opaque elbow with a 0.5 x 0.5 μm defect col-
linear with the vertical inner edge and horizontal outer edge of the elbow
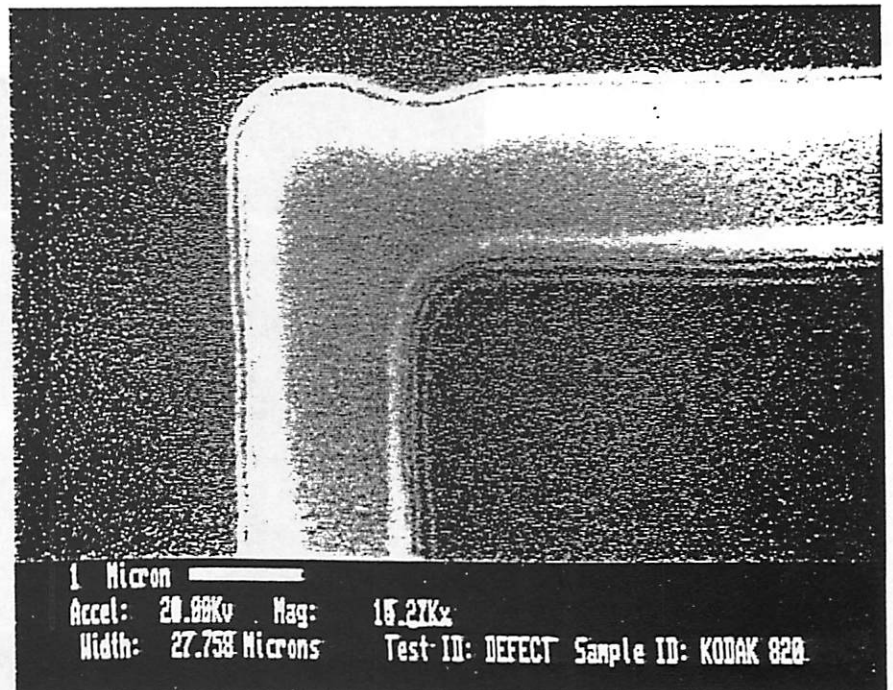
(b) At best focus underexposed
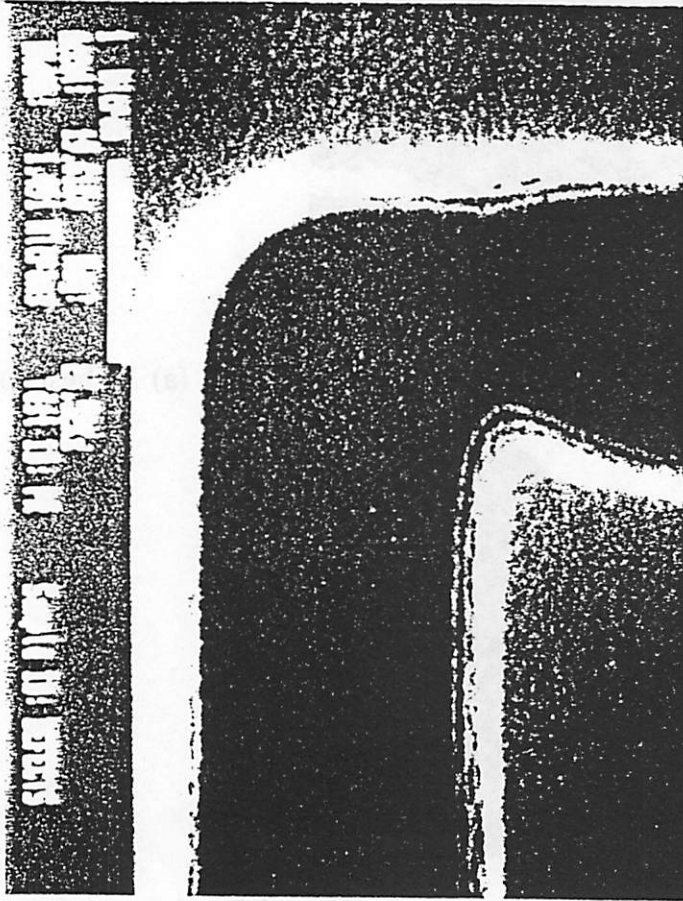
(a) At best focus and dose

Fig. 5.28. SEM photographs of a transparent elbow with a 0.5 x 0.5 μm defect collinear with the vertical and horizontal inner edges of the elbow

1 Micron
Accel: 20.00Kv   Mag: 14.64Kx
Width: 27.758 Microns   Test ID: DEFECT Sample ID: KODAK 820
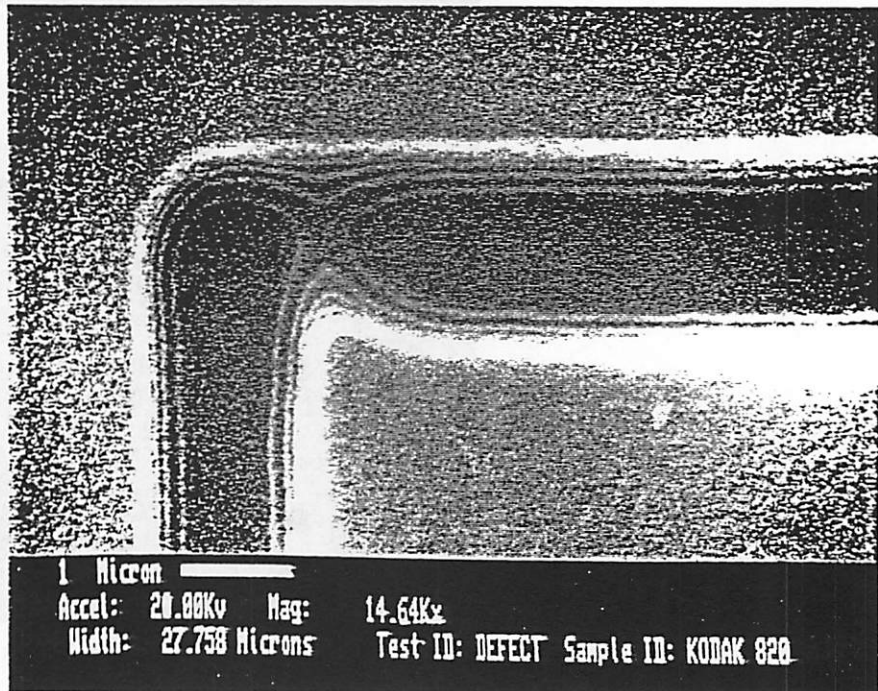
(b) At best focus underexposed
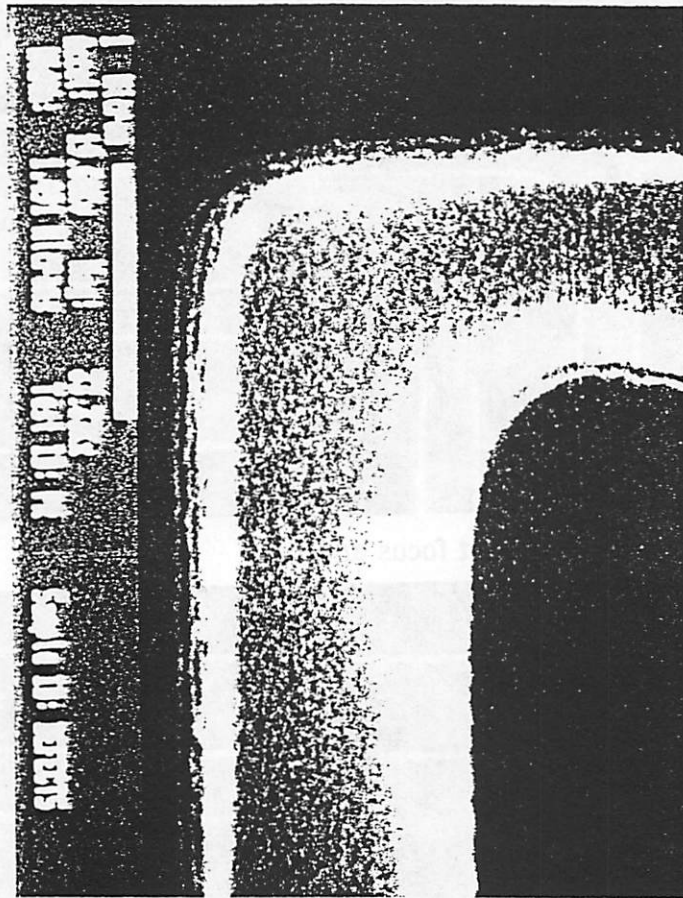
(a) At best focus and dose

Fig. 5.29. SEM photographs of an opaque elbow with a 0.5 x 0.5 μm defect collinear with the vertical and horizontal inner edges of the elbow


```
1 Micron
Accel:  20.00Kv   Mag:    14.72Kx
Width:  27.758 Microns    Test ID: DEFECT  Sample ID: KODAK 820
```

(b) At best focus underexposed

(a) At best focus and dose

(b) At best focus underexposed

10 Microns
Accel: 19.92Kv Mag: 7.85Kx
Width: 1.631 Microns   Test ID: HUYNH Sample ID: PR DEFECTS
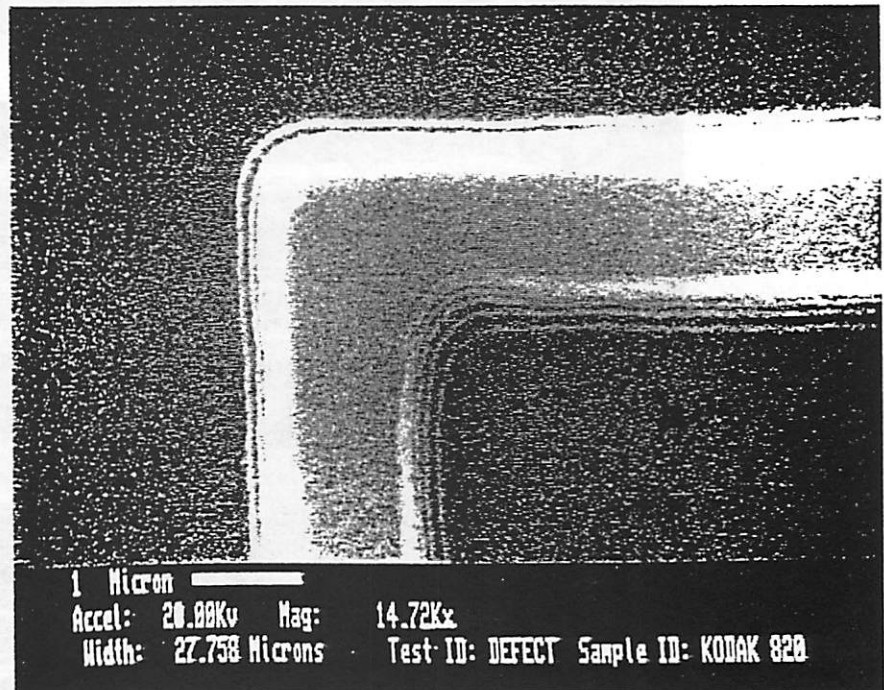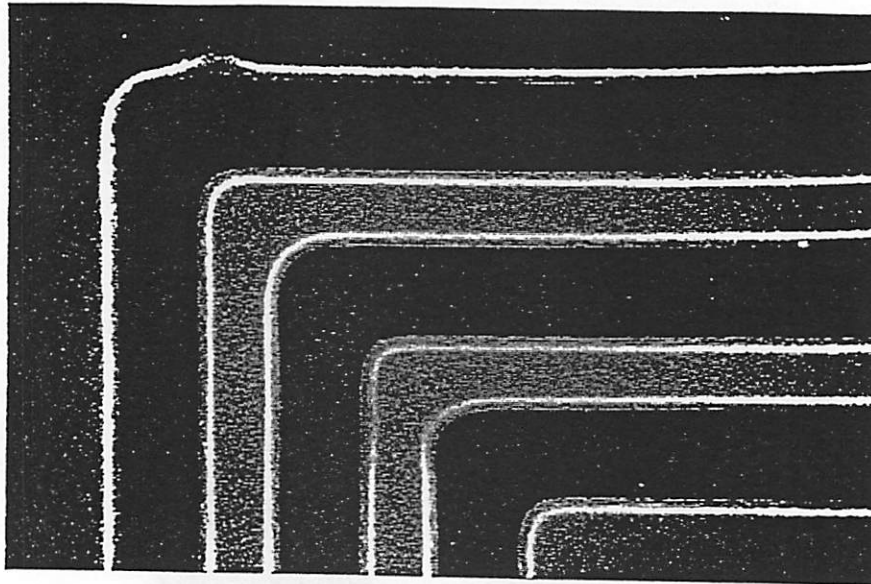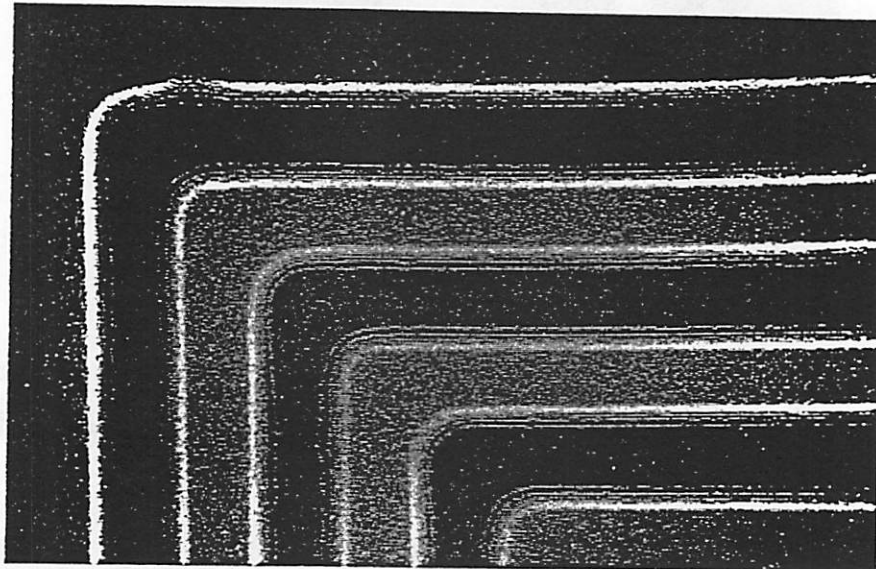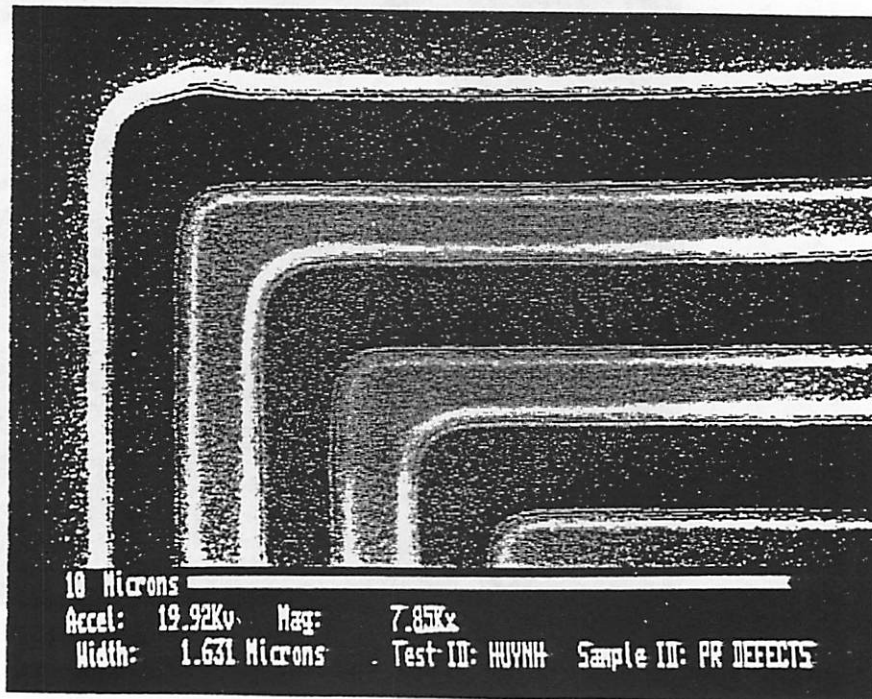
(c) At best dose 3 μm defocus

Fig. 5.30. Transparent nested elbows with two defects one located collinearly with the vertical inner edge of the outermost elbow, and the other located between the two inner elbows

(a) At best focus and dose

(b) At best focus underexposed

10 Microns
Accel: 19.92Kv   Mag: 7.87Kx
Width: 1.631 Microns   Test II: HUYNH   Sample II: PR DEFECTS
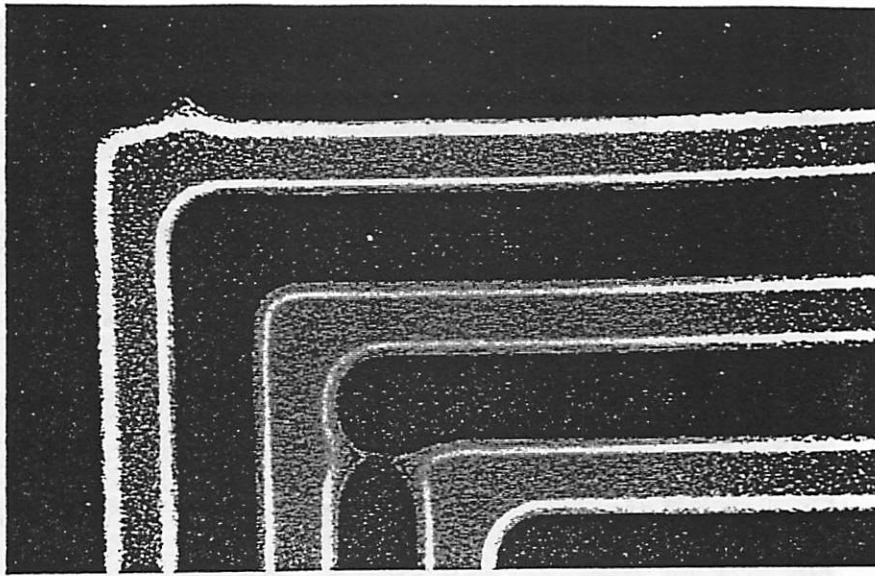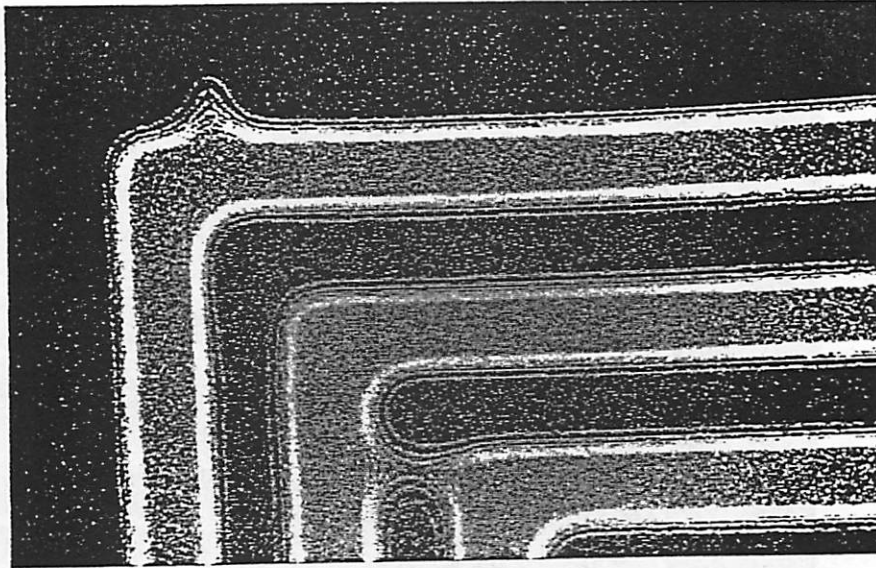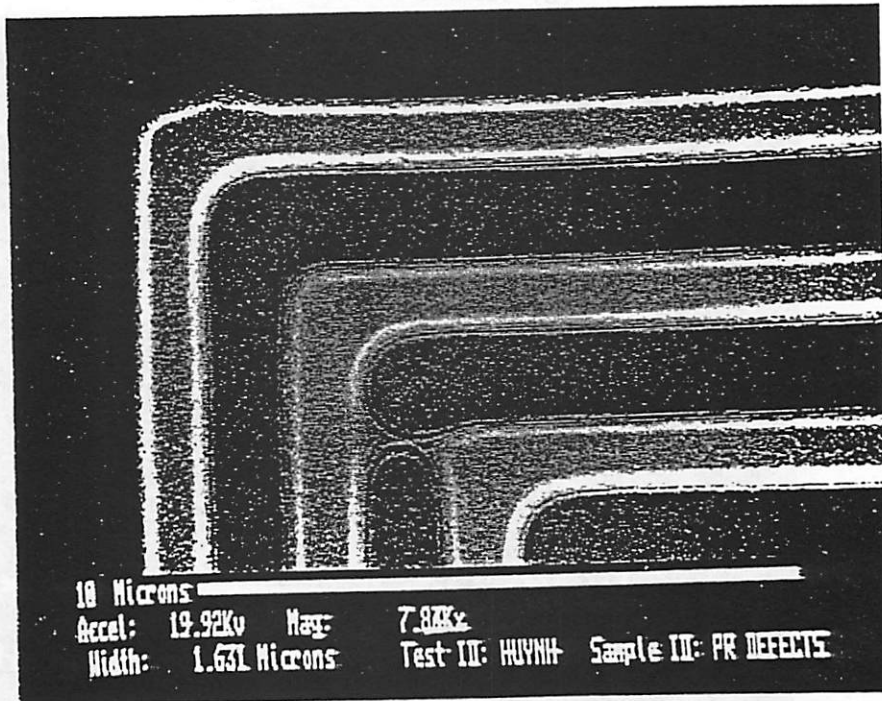
(c) At best dose 3 μm defocus

Fig. 5.31. Opaque nested elbows with two defects one located collinearly with the vertical inner edge of the outermost elbow, and the other located between the two inner elbows
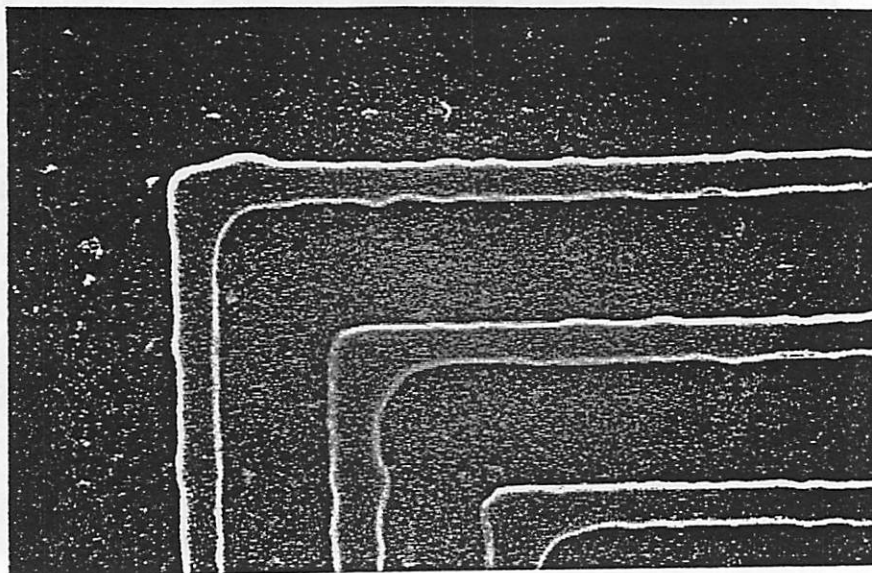
(a) At best focus and dose
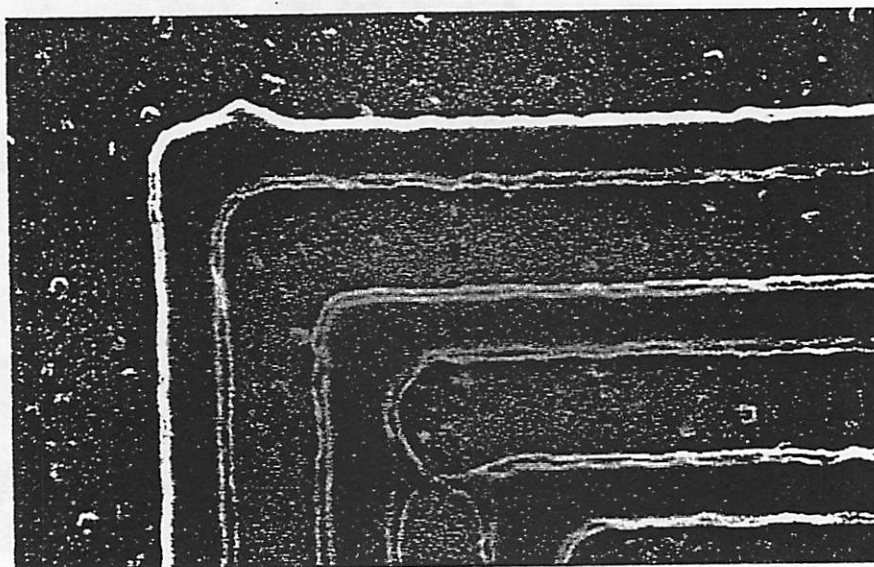
(b) At best focus underexposed
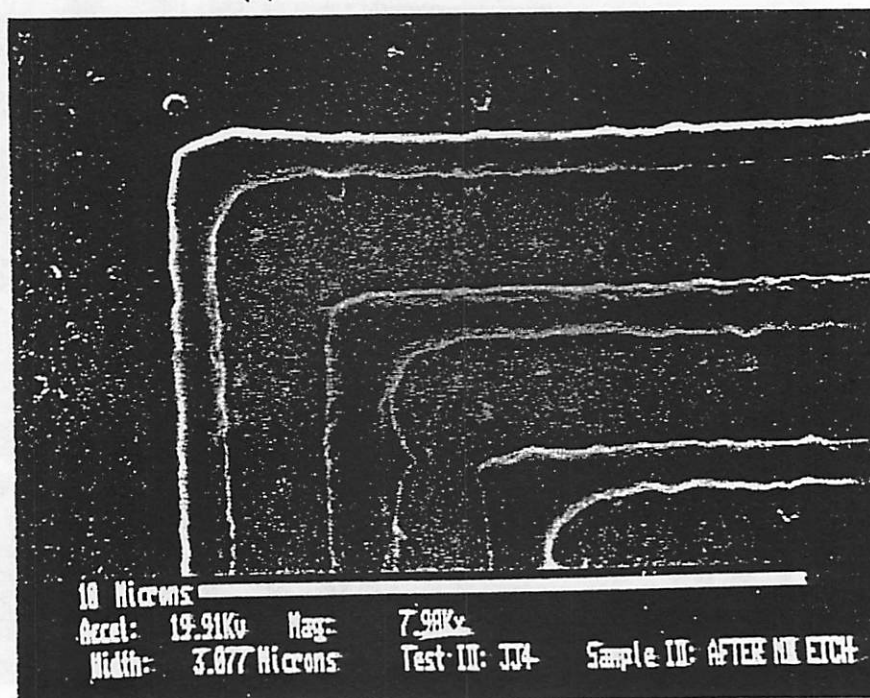
(c) At best dose 3 μm defocus

Fig. 5.32. Opaque nested elbows on Al substrate with two defects one located col-linearly with the vertical inner edge of the outermost elbow, and the other located between the two inner elbows